# ABSTRACT

Title of dissertation: FEASIBILITY OF IN VIVO SAXS IMAGING FOR DETECTION OF ALZHEIEMER'S DISEASE

Mina Choi, Doctor of Philosophy, 2017

Dissertation directed by: Aldo Badano
U.S. Food and Drug Administration
Center for Devices and Radiological Health
Office of Science and Engineering Laboratories
Division of Imaging, Diagnostics, and Software Reliability

Small-angle x-ray scattering (SAXS) imaging has been proposed as a technique to characterize and selectively image structures based on electron density structure which allows for discriminating materials based on their scatter cross sections. This dissertation explores the feasibility of SAXS imaging for the detection of Alzheimer's disease (AD) amyloid plaques. The inherent scatter cross sections of amyloid plaque serve as biomarkers *in vivo* without the need of injected molecular tags. SAXS imaging can also assist in a better understanding of how these biomarkers play a role in Alzheimers disease which in turn can lead to the development of more effective disease-modifying therapies. I implement simulations of x-ray transport using Monte Carlo methods for SAXS imaging enabling accurate calculation of radiation dose and image quality in SAXS-computed tomography (CT). I describe SAXS imaging phantoms with tissue-mimicking material and embedded scatter targets as a way of demonstrating the characteristics of SAXS imaging. I

also performed a comprehensive study of scattering cross sections of brain tissue from measurements of ex-vivo sections of a wild-type mouse brain and reported generalized cross sections of gray matter, white matter, and corpus callosum obtained and registered by planar SAXS imaging. Finally, I demonstrate the ability of SAXS imaging to locate an amyloid fibril pellet within a brain section. This work contributes to novel application of SAXS imaging for Alzheimer's disease detection and studies its feasibility as an imaging tool for AD biomarkers.

# FEASIBILITY OF IN VIVO SAXS IMAGING FOR DETECTION OF ALZHEIEMER'S DISEASE

by

Mina Choi

Dissertation submitted to the Faculty of the Graduate School of the
University of Maryland, College Park in partial fulfillment
of the requirements for the degree of
Doctor of Philosophy
2017

Advisory Committee:
Professor Yu Chen, Chair/Academic Advisor
Dr. Aldo Badano, Co-chair/Research Advisor
Professor Robert Briber, Dean's Representative
Professor Silvina Matysiak
Professor Ian White

# Dedication

I dedicate this to my grandfather, who suffered with Alzheimer's disease for as long as I could remember before passing in 2007 and to my grandmother who cared for him. I also dedicate this to my loving and supportive family and husband who supported me through this PhD program and pushed me towards success.

# Acknowledgments

I would first and foremost like to express my deepest gratitude to **Dr. Aldo Badano**, for his advice, steady leadership, and mentorship. Thank you for patiently guiding me through several research projects and helping me develop professionally. I thank **Dr. Yu Chen** for providing academic advising and being approachable mentor and teacher. Thank you to the family at the **Division of Imaging Diagnostics and Software Reliability** (OSEL/CDRH/FDA) for your support, collegiality, and friendship.

Thank you to the following people for their guidance, training, and contribution to this research:

**Dr. Andreu Badal** for guidance with MC-GPU and assistance with 3D-printing.

**Dr. Bahaa Ghammraoui** for guidance and assistance with MC-GPU, training with X-ray equipment.

**Eshan Dahal** for providing a BSA amyloid model.

**Dr. Wei-Chung Cheng** for guidance and assistance with microscopy and photography equipment.

**Randolph Bidinger and Fred Jordan** for machine shop service in CNC-milling phantom.

**Dr. Hey-Kyoung Lee** for providing transgenic and wild-type mouse brain tissue.

**Dr. Christen Welle** for providing wild-type mouse brain tissue.

**Christopher Gorini** for providing mouse skull tissue.

**Beom Koo** for training on vibratome.

**Anna Lee** for histological staining training.

**Dr. Maria Iacono** for providing MIDA virtual head phantom.

Finally, I thank **Dr. Robert Fischell** for the fellowship that funded my PhD in the spirit of entrepreneurship and biomedical engineering and the **University of Maryland Bioengineering Department** for the opportunity to pursue my PhD degree, specialized traning in the future faculty program, and providing me with resources to be successful.

# Table of Contents

# List of Figures

# List of Abbreviations

| | |
|---|---|
| A$\beta$ | $\beta$ Amyloid |
| AD | Alzheimer's Disease |
| ADNI | Alzheimer's Disease Neuroimaging Initiative |
| AgBe | Silver Behenate |
| APP | Amyloid Precursor Protein |
| BSA | Bovine Serum Albumin |
| BRET | Bioluminescence Resonance Energy Transfer |
| CCD | Charged-Coupled Device |
| CNC | Computer Numerical Control |
| CSF | Cerebral Spinal Fluid |
| CT | Computed Tomography |
| DC | Dark Current |
| DSM-5 | Diagnostic and Statistical Manual of Mental Disorders |
| DLS | Dynamic Light Scattering |
| DMSO | Dimethyl Sulfoxide |
| FDA | Food and Drug Administration |
| FoXS | Fast SAXS Profile Computation Program |
| FRET | Fluorescence Resonance Energy Transfer |
| GM | Gray matter |
| GNP | Gold Nanoparticle |
| GPU | Graphical Processing Unit |
| IAA | Independent Atomic Approximation |
| ICRP | International Commission on Radiation Protection |
| ICRU | International Commission on Radiation Units & Measurements |
| MCI | Mild Cognitive Impairment |
| MC-GPU | Monte Carlo - Graphical Processing Unit |
| MIDA | Multimodal Imaging-Based Detailed Anatomical Model |
| MIF | Molecular Interference Factor |
| MRI | Magnetic Resonance Imaging |
| P-tau | Phosphorylated Tau |
| PDB | Protein Data Bank |
| PENELOPE | A Code System for Monte-Carlo Simulation of Electron and Photon Transport |
| PET | Positron Emission Tomography |
| PIB | Pitssburgh Compound B |
| PMMA | Poly(methyl methacrylate) |
| PSAXS | Planar Small-angle X-ray Scattering |
| ROI | Region-of-Interest |
| SAS | Small-angle Scattering |
| SAXS | Small-angle X-ray Scattering |
| SAXS-CT | Small-angle X-ray Scattering Computed Tomography |
| SDD | Sample-to-Detector Distance |
| SNR | Signal-to-Noise Ratio |
| SPECT | Single-Photon Emission Computed Tomography |
| T-tau | Total Tau |
| Tg | Transgenic |
| UMD | University of Maryland |
| UV-Vis | Ultraviolet-Visible Spectroscopy |
| USAXS | Ultra Small-Angle X-ray Scattering |
| WAXS | Wide-angle X-ray Scattering |
| WM | White Matter |
| WT | Wild-type |

# Chapter 1: Introduction

The purpose of this work is to study the feasibility of small-angle x-ray scattering (SAXS) to detect Alzheimer's disease biomarkers *in vivo*. We study SAXS because it is tailored to characterizing molecular structure and aggregates and could be applied as a medical imaging tool for detection of Alzheimer's disease. This chapter provides a description of Alzheimer's disease, the general theory of SAXS, and the scope of the dissertation.

## 1.1 Overview of Alzheimer's disease

Alzheimer's disease (AD) is an insidious neurodegenerative disorder characterized by impaired memory, reduced cognitive skills, and diminished ability to perform everyday tasks. It is the most common cause of dementia, accounting for 60-80% of cases. Like many other neurodegenerative disorders, there is still no cure, nor ways of slowing or reversing the disease progression. [40] As of 2017, the National Institute on Aging estimates that as many as 5.5 million Americans suffer from AD. [3] Recent discoveries reveal that biomolecular changes associated with AD occur 20 or more years before dementia symptoms appear. Early detection of these changes may be pivotal to developing therapies based on molecular behavior to preventing,

slowing, and ultimately stopping AD. [45, 71, 84, 89]

Two hallmarks of AD onset is the accumulation of $\beta$ amyloid (A$\beta$) plaques and neurofibrillary tau tangles in the brain. A$\beta$ plaques originate from an amyloid precursor protein (APP) that is embedded in the cell membrane. In a benign pathway, an enzyme, $\alpha$ secretase, cleaves APP producing and releasing sAPP$\alpha$ intracellularly for neuronal growth and survival. Another enzyme, $\gamma$ secretase cleaves the remaining piece in the membrane into two peptides. The smaller peptide is released extracellularly and is harmless. In the malignant pathway, $\beta$ secretase enzyme cleaves APP at an errant location producing sAPP$\beta$. The $\gamma$ secretase then cuts the remaining pieces. The produced peptide, A$\beta$ aggregates extracellularly forming A$\beta$ plaques. These A$\beta$ oligomers grow large enough to form fibril like structures and to obstruct surrounding neuronal function.

In contrast to A$\beta$ plaques which build up extracellularly at the synapses of neurons, the neurofibrillary tau angles are protein aggregates inside the cell. Tau is a peptide that, in normal conditions, stabilizes the microtubule in neurons. When hyperphosphorlation occurs, tau disengages from microtubules and aggregate into phosphorylated tau (P-tau) threads that aggregate with other threads to form helical structures. These helical structures eventually aggregate to form tangles. Without functioning tau and microtubules, neurons implode disrupting neuronal pathways. This process is known as tauopathy and leads to many forms of dementia, however, the majority of cases leads to AD.

### 1.1.1 Therapeutic approaches

There are several impeding factors to developing therapies for Alzheimer's disease which include the long time (up to 20 years) needed to observe disease progression in Alzheimer's, challenging feat of delivering drugs through the blood-brain barrier, and lack of understanding of AD pathogenesis for targeted disease-modifying treatments. [11] Currently six drugs are approved by the U.S. Food and Drug Administration (FDA) that temporarily improve symptoms of AD by increasing neurotransmitters in the brain. However, the effectiveness varies among patients. There are several drugs undergoing clinical trials to modify the disease process for example by use of immunotherapy, amyloid aggregators, and tau aggregation inhibitors. Also, treatments to slow or stop the progression of AD and preserve brain function will be most effective when administered during the preclinical and mild cognitive impairment (MCI) stages of the disease. In 2013, FDA released a draft guidance for industry to develop drugs for the treatment of early stage AD [2] which calls for the exploration of new biomarkers for evaluation of these drugs. There is a pressing need to discover specific and more sensitive biomarkers to evaluate these drugs effectively at earlier stages.

### 1.1.2 Current diagnostic procedures

*Psychopathology:* A variety of approaches and tools are used to help make diagnosis of AD. The 1984 diagnostic procedure had initially only included psychopathological evaluations such as a medical and family history from the individ-

ual, psychiatric history, input about changes in thinking skills or behavior from someone close to the individual, cognitive tests, and physical and neurologic examinations. [61] Recently, the diagnostic criteria was updated to include imaging techniques [84] and physicians refer to medical resources such as the DSM-5. [1] We review a few of the added techniques here.

*Anatomical Imaging:* Computed tomography (CT) and magnetic resonance imaging (MRI) are recommended for use in detecting intercranial lesions or other deases that may cause dementia symptoms such as cerebrovascular disease and tumours as an exclusion technique. More novel uses of anatomical MRI has also been used to visualize atrophy differences in the medial temporal lobe in patients with AD and age-matched individuals with a sensitivity and specificity >85%. [90] However the differences between AD and non-AD dementia are not clear using this technique. Other quantitative techniques use volumetric imaging. Three dimensional (3D) mapping of the hippocampus and cortical thickness measurements are promising markers for AD and are currently under investigation at the Alzheimer's Diseases Neuroimaging Initiative (ADNI). [68, 79]

*Cerebrospinal Fluid Analysis:* A$\beta$ peptides and phosphorylated tau (P-tau) have been studied in cerebrospinal fluid (CSF) and independent studies have shown that AD can be differentiated from other dementias by detection of lower concentrations of A$\beta_{1-42}$, higher concentrations of total tau (T-tau), and higher concentrations of P-tau at theonine 231 and 181. [11] This technique had a sensitivity of 83% and specificity of 72%. [57] Another longitudinal study showed that early AD patients with MCI could be identified with a sensitivity of 95% and specificity of

83% studying the combination of T-tau, P-tau, and A$\beta_{1-42}$ in CSF. [37]

*Functional Neuroimaging:* Positron Emission Tomography (PET) with fluorodeoxyglucose (FDG) has been approved by FDA for use in USA for diagnostic purposes in detecting early stage AD. FDG-PET has shown good accuracy in differentiating AD patients from age-matched control individuals. The described AD diagnostic criterion is a reduction of glucose metabolism in the bilateral temporal parietal regions in the posterior cingulate cortex. Meta-analysis has shown this technique to have a sensitivity and specificity of 86% for AD diagnosis however there are many variations between studies. This technique did not perform as well for differentiating AD with other dementia. PET with $^{11}$C-labelled Pittsburgh compound B (PIB) and $^{18}$F-labelled $A\beta$ ligand can be used to directly visualize $A\beta$ in vivo. [80] However, PET has low spatial resolution and low specificity.

$^{99m}$Tc-HMPAO or 133Xe with single-photon emission CT (SPECT) has shown a lower clinical accuracy of 74% for AD patients and control individuals. [24] However it is a useful technique to differentiate AD from other dementia. The use of dopamine transporter with $^{123}$I-fluoropropylcarboxy-metoxynortropane in differentiating Lewy bodies dementia and Parkinson's disease from AD was sufficient enough to be included in the diagnostic criteria for Lewy bodies dementia. [59, 60]

There have been significant advancements in diagnostic tools available for AD. We aim to study the feasibility of an additional complementary tool to assist with the study of this disorder.

Small-angle x-ray scattering (SAXS) imaging has the potential to advance molecular imaging for applications where both depth and high-resolution are re-

quired without the use of contrast probes. SAXS can characterize and selectively image structures based on electron density maps which allows for distinguishing materials based on their scatter properties [6, 47].

Well-characterized SAXS profiles of AD plaques could potentially serve as early detection *in vivo* biomarkers. The SAXS signals for the AD proteins $A\beta$ and tau and their various aggregate states have not yet been described *in vitro* nor in tissue. The applicability of the SAXS imaging technique for AD depends on a differentiating generalized scatter profile for AD aggregates in the brain. This thesis aims to study the feasibility of utilizing this molecular imaging technique for detection of AD plaques *in vivo*.

## 1.2 Primer on SAXS

X rays were first discovered by Roentgen in 1905 [72] and has since been utilized for a variety of applications medical diagnostics (2D radiographic [21] and 3D tomographic [41] medical imaging) and for nondestructive inspection. X rays are electromagnetic waves with much shorter wavelengths, $\lambda$, than visible light (between 0.1 to 10 nm). X rays are also interpreted in terms of photons of energy, $E$ (eV), which relates to $\lambda$ in the following way,

$$E = \frac{hc}{\lambda}, \tag{1.1}$$

where $h$ is Planck's constant, $6.62\times10^{-34}$ (joules s) and $c$ is the velocity of light, $2.998\times\ 10^{8}$ (m/s). Because of their high energy and short wavelengths, they are

able to penetrate through thicker and denser objects than visible light and provide information at the atomic length scale. Similarly to visible light, x rays are either transmitted through objects unperturbed, or interact with the objects by absorption or scattering events. These events can be modelled by probability distribution functions which depend on the electron density of the material and the wavelength of the x rays.

Conventional medical imaging applications largely differentiates materials based on their absorption properties providing micrometer scale morphological spatial information and scattering has traditionally been treated as noise to these systems. Research efforts have therefore been to remove x-ray scattering events by collimation and post-processing. However, a limitation of these absorption-based approaches in medical diagnostics is that many pathologies share similar attenuation characteristics with normal surrounding tissues, especially during early disease stages where change occurs at molecular and cellular levels. Conversely, in x-ray diffraction and crystallography, material nanoscale size, shape, structure, and periodicity has been studied by measuring x-ray scattering and absorption is minimized to maximize scatter signal.

### 1.2.1 Absorption

Absorption occurs when an x ray ejects an electron from the electron cloud of an atom in the material it travels through. This event is known as the photoelectric effect. The energy that the x ray possessed is transferred completely to the electron

which is expelled and the atom rearranges the remaining electrons to fill the electron hole. If an electron from an inner shell is ejected, an electron from an outer shell will move in to fill the hole at inner shells and the atom will emit fluorescence radiation to balance the energy of the event. The emitted fluorescence is an x ray with a different energy than that of which was absorbed. The probability that absorption occurs depend on the energy of the x ray and material density. The fraction of x rays that are absorbed can be described as,

$$\frac{I}{I_0} = e^{-\mu(\lambda)\rho x}, \tag{1.2}$$

where $I_0$ is the initial number of x rays before traversing through a material, $I$, is the number of x rays recorded after traversing through the material at the same angle of $I_0$, $\mu$ is the mass absorption coefficient of the material dependant on $\lambda$, $\rho$ is the density of the material, and $x$ is the thickness of the material. This absorption coefficient increases with increasing $\lambda$, except at characteristic fluorescent x ray wavelengths. $\mu$ is the material-dependent property that is often exploited in conventional x-ray radiography for differentiation of tissue types. In x-ray diffraction studies, material thickness is adjusted to minimize absorption effects. The optimal thickness, $x_{opt}$, that provides the most scatter is approximated by the following,

$$x_{opt} = \frac{1}{\mu(\lambda)}. \tag{1.3}$$

### 1.2.2 Scattering

There are two kinds of x-ray scattering that can occur: Rayleigh scattering and Compton scattering. Rayleigh scattering, also called coherent scattering, scatters x rays such that the x ray changes direction, but not energy whereas Compton scattering, or incoherent scattering, typically scatters at wider angles and energy of the x ray is reduced after the scattering event. The Rayleigh scattering angular range has been further categorized to ultra small-angle x-ray scattering (USAXS), small-angle x-ray scattering (SAXS), and wide-angle x-ray scattering (WAXS) by the length scales of the structures they probe. These scattering domains are depicted in Fig. 1.1

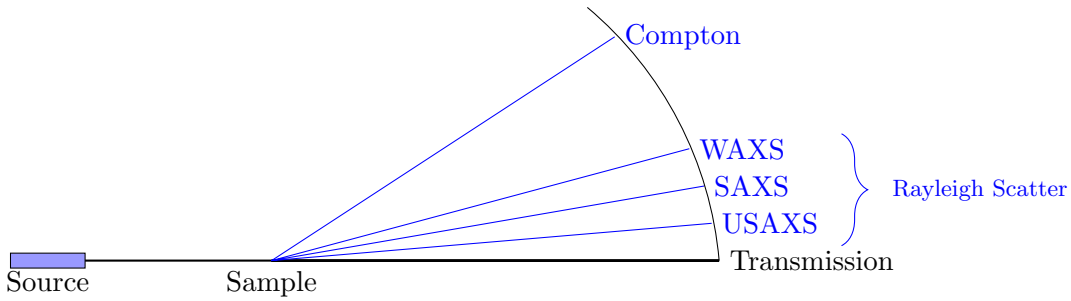


Figure 1.1: Schematic of scattering domains.

Fig. 1.2 shows a typical SAXS system which includes a monochromatic x-ray source, a collimation system to focus the x-ray beam, a beamstop to attenuate a portion of the primary transmitted x rays, and a detector to measure the scattered x rays from interaction with a sample. The collimation could be a series of pinholes, or blocks and they are used to form pencil beams or line beams. Line beams are used because they increase the number of x rays that pass through the sample,

thereby shortening measurement times, however line-collimated SAXS data requires an additional desmearing post-processing step adding uncertainty to the data. On the other hand, point-collimated pencil beams do not generally need a desmearing step. The beamstop protects the detectors from burn-in by the primary x rays and prevent the detector also from saturating to enable measurements of the much weaker scatter signal.

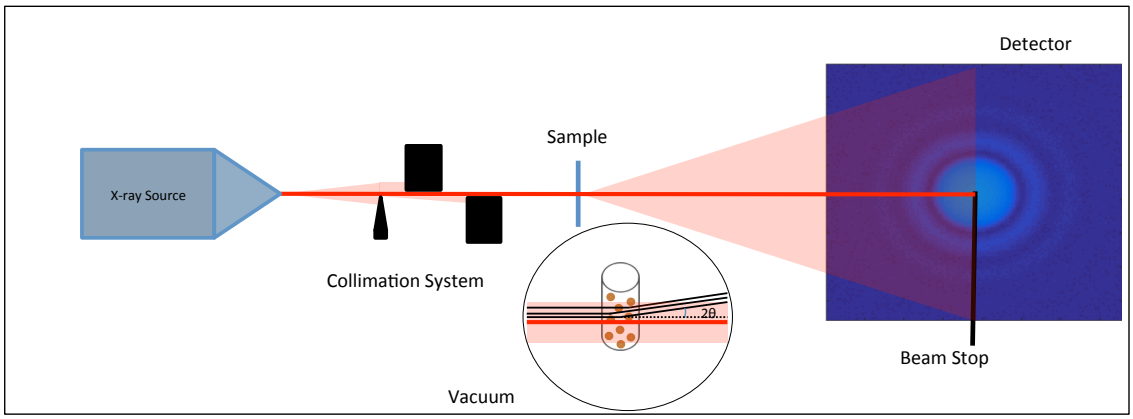


Figure 1.2: Schematic of a typical transmission SAXS system enclosed in vacuum.

For a system with square pixel detectors, the scattering angle, $2\theta$, can be calculated by,

$$2\theta = atan(\frac{p_n p_x}{d}), \tag{1.4}$$

where $p_0$ is the pixel at the center of the primary beam, and $p_n$ is the number of pixels away from the center pixel. $p_x$ is the pixel pitch and the $d$ is the sample-to-detector distance.

The scattering vector, also known as momentum transfer, is described in the

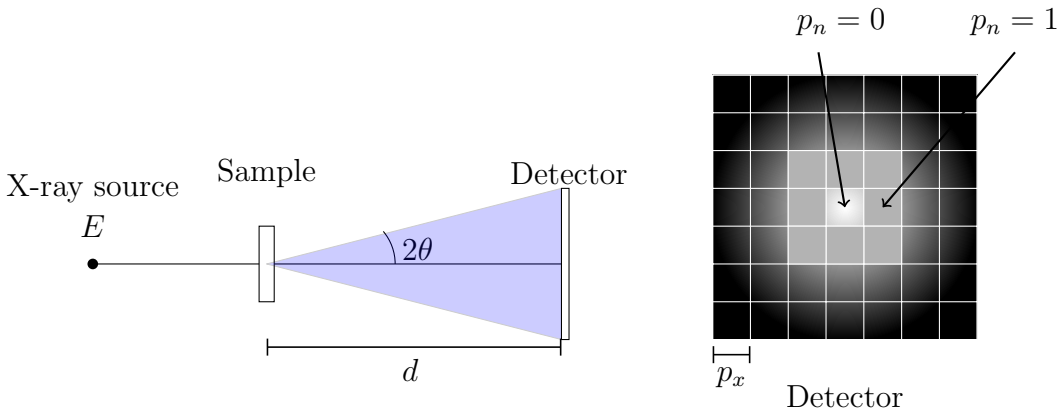


Figure 1.3: Schematic of SAXS system with square pixel detectors.

following equation,

$$q = \frac{4\pi sin(\theta)}{\lambda}, \tag{1.5}$$

where $\theta$ is half of the scattering angle as depicted in Fig. 1.3. The scattering vector is used over $2\theta$ because it accounts for the wavelength of the x-ray source and maintains consistency of scatter profiles between various instrument geometries and energies used.

For randomly oriented scatterers, the 2D scatter is isotropic and can be reduced to a 1D scatter profile by radially averaging. For anisotropic, oriented scatterers, the 2D scatter image will not be radially symmetric, therefore should not be reduced to a 1D scatter profile. Fig. 1.4 shows an example of anisotropic and isotropic signals that we have measured of mouse brain tissue and glassy carbon respectively.

Intensity of x-rays is defined by the flux of energy crossing a unit surface

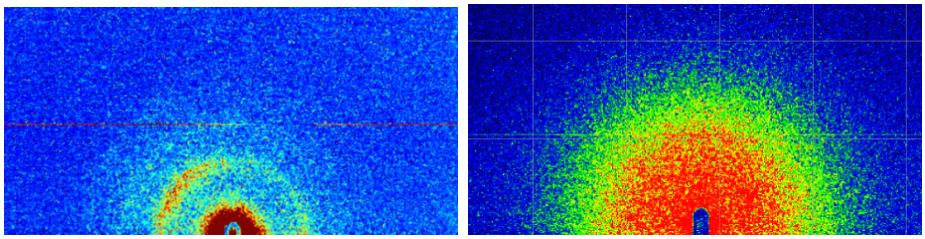

Figure 1.4: An example of anisotropic scatter from mouse brain tissue and isotropic scatter from glassy carbon respectively.

volume per second. The intensity of scatter is described as the following,

$$I_s(q) = I_0 n \rho^2 V^2 F^2(q) S(q), \tag{1.6}$$

where $n$ is number of particles, $\rho$ is the particle electron density, $V$ is the particle volume, and $F(q)$ is the form factor which informs particle shape and size, and $S(q)$ is the structure factor which accounts for interference effects of multiple particles in close proximity.

To subtract scatter contributions from the instrument and sample holder, often times a scatter profile is obtained for the background, $bg$, which is scaled to the sample scatter profile by the primary beam, then subtracted,

$$I(q) = I_s(q) - I_{bg}(q) T_f, \tag{1.7}$$

where $T_f$ is the transmission scaling factor. These steps are shown in Fig. 1.5. In this case, we observe the change in electron density of the scatter profile, $\Delta\rho$, which provides contrast to the background scattering.

The primer on SAXS was developed from the following sources. [26, 33, 36]

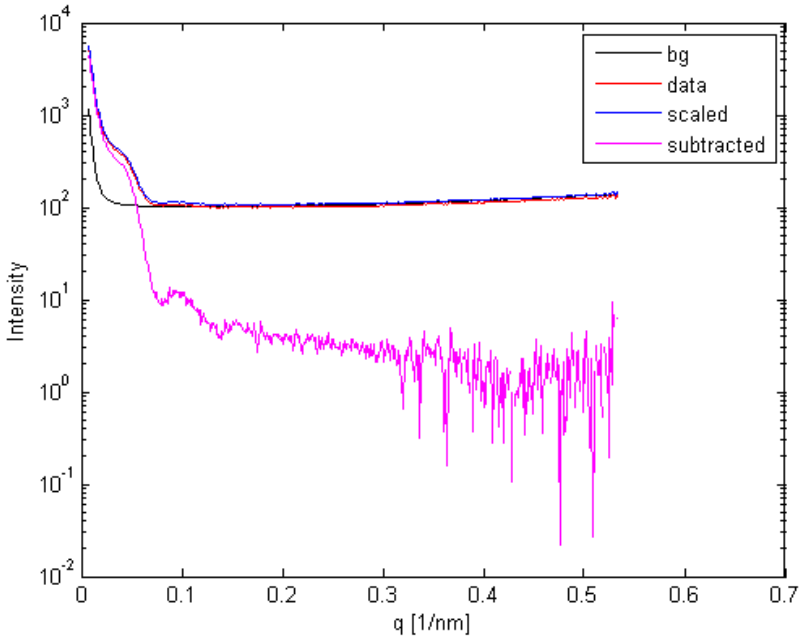


Figure 1.5: Scaling and background subtraction data treatment.

Additional corrections due to geometric distortions and detectors are performed to the scatter intensity. [65]

## 1.3 Thesis scope

In this chapter, we introduce Alzheimer's disease, the impact it has on our society, the motivation for our study to present a novel approach to imaging this disorder by molecular changes occurring in the brain, and the general theory of SAXS.

In chapter 2, we present SAXS measurements of isolated peptides of A$\beta$ and tau *in vitro* in various buffer solutions. We discuss decisions made to focus on A$\beta$ and on *ex vivo* tissue rather than *in vitro* as these peptide aggregate structure in buffer solutions may not accurately describe what happens *in vivo*.

In chapter 3, we introduce simulations of x-ray transport that allows us to study instrument design and optimal sample thickness that will enable us to discern a signal of interest from nanoparticles in a transmission SAXS system and also for SAXS in computed tomography (CT) geometry. This work is published in Journal of Applied Crystallography.

Chapter 4, we simulate a simplified SAXS-CT system for detection of dilute gold spherical nanoparticles in water.

Chapter 5 presents planar SAXS imaging measurements of a developed phantom with known cross sections and demonstrates feasibility of planar SAXS to differentiate materials and increase signal based on material scattering cross sections. This work was published in Applied Physics Letters.

Chapter 6 presents our measurements of planar SAXS on slices of normal *ex vivo* mouse brains. We segment different tissue regions in the planar SAXS image and characterize cross sections of the white matter, gray matter, and corpus callosum in the mouse brain.

In chapter 7, we demonstrate the ability of planar SAXS to measure amyloid fibrils in a mouse brain. Transgenic Alzheimer's disease mouse model and wild-type mice brains are measured and compared.

Finally, in chapter 8, we conclude our work and present outlooks for SAXS-CT and it's feasibility for detection of molecular changes in the brain for application of Alzheimer's disease.

# Chapter 2: Preliminary *in vitro* SAXS measurements of A$\beta$ and Tau

There is a need for novel imaging techniques for the earlier detection of Alzheimer's disease (AD). Two hallmarks of AD are amyloid beta ($A\beta$) plaques and tau tangles that are formed in the brain. Well-characterized x-ray cross sections of $A\beta$ and tau proteins in a variety of structural states could potentially be used as AD biomarkers for small-angle x-ray scattering (SAXS) imaging without the need for injected probes or contrast agents. In this chapter, we report SAXS measurements of $A\beta_{42}$ and $\text{tau}_{352}$ in a 50% dimethyl sulfoxide (DMSO) solution in which these proteins are believed to remain monomeric because of the stabilizing interaction of DMSO solution. However, our SAXS analysis showed the aggregation of both proteins. In particular, we found that the aggregation of $A\beta_{42}$ slowly progresses with time in comparison to $\text{tau}_{352}$ that aggregates at a faster rate. Furthermore, the measured signals were compared to the theoretical SAXS profiles of $A\beta_{42}$ monomer, $A\beta_{42}$ fibril, and $\text{tau}_{352}$ that were computed from their respective protein data bank structures. We have begun the work to systematically control the structural states of these proteins *in vitro* using various solvent conditions.

While various peptide lengths of $A\beta$ exist, we initially study the $A\beta_{42}$ isomer because it is the most fibrillogenic and therefore most associated with amyloid load.

There are also six isoforms of tau that depend on phosphorylation epitopes. Not much is understood about how each of these protein isoforms affect AD. They take on various structural forms and could potentially be differentiated in SAXS imaging which may give insight into their role in AD. We have focused our study on the smallest isoform, $tau_{352}$. Aggregation of these proteins has been reported to depend on sample temperature, solvent pH, ionic concentration, and time. [4, 89, 92] Therefore, the environment and solvent conditions have been controlled in order to obtain SAXS signals for the AD proteins at specific aggregate states.

## 2.1 Methods

Lyophilized powder form of human $tau_{352}$ peptide (Abcam, Cambridge, UK) and human $A\beta_{42}$ peptide (Anaspec, Fremont, CA) were stored at -20°C before sample preparation. We dissolved the proteins in 50% DMSO (pH 8) because they were reported to remain monomeric in this solvent. [82] $A\beta_{42}$ was dissolved with a concentration of 5.6 mg/ml and $tau_{352}$ was dissolved with a concentration of 1.43 mg/ml. Each sample was loaded into a 1 mm diameter quartz capillary and held in a temperature-controlled sample holder at 37 °C.

SAXS measurements were performed using SAXSpace (Anton Paar, Ashland, VA, USA). The instrument, which uses Cu $K_\alpha$ radiation ($\lambda = 0.154$ nm), was configured in Kratky block point collimation mode with an accessible $q$ range of 0.14–2 $nm^{-1}$. The system is equipped with a CCD camera with a pixel pitch of 24 $\mu$m in an array of 2084×2084 pixels. The camera uses a $Gd_2O_2S$:Tb phosphor screen

optimized for 8-keV X rays. The sample holder was positioned at a distance of 305.3 mm from the CCD. The collimation system, sample chamber, and beam path were enclosed in vacuum with a pressure below 3 mbar. The CCD pixels were binned along the length of the beam (2 cm). SAXS measurements were obtained with an exposure time of 5 s and 200 frames for each protein. The samples were measured 5 min after preparation and again after 4 days. Between measurements, the samples were stored at room temperature.

Preliminary data treatment of scatter profiles including solvent background and dark current subtraction were performed in SAXStreat (Anton Paar, Ashland, VA, USA) and SAXSquant (Anton Paar, Ashland, VA, USA). Subsequent data analysis for measurements included beam desmearing, fitting approximations, and obtaining pair distance distribution functions, $P(r)$, using indirect Fourier transform. [31] Guinier analysis [34] was performed using custom code written with MATLAB R2015a (The MathWorks Inc., Natick, MA) to obtain information about the radius of gyration, $R_g$, of the protein. A larger $R_g$ than what is expected based on the protein's monomeric structure is one indicator of aggregation.

In the Guinier approximation of $R_g$, a $q$ range of 0.001-0.399 nm$^{-1}$ was used for $A\beta_{42}$ sample measured after 5 min and the PBD data of $A\beta_{42}$ where $q = 4\pi sin(\theta)/\lambda$. A $q$ range of 0.001-0.200 nm$^{-1}$ was used as a low angles for the $A\beta_{42}$ sample measured after 4 days, and 0.300-0.400 nm$^{-1}$ was used for wider angles because more than one slope region was observed. For all tau$_{352}$ samples, a $q$ range of 0.001-0.140 nm$^{-1}$ was used at low angles, and 0.270-0.310 nm$^{-1}$ was used for wider angles.

The $R_g$ was also calculated for each sample using the electron pair distribution

function, $P(r)$, which provides information on the average protein shape in the solution. The $R_g$ was calculated using the following equation,

$$R_g^2 = \frac{\int_0^{D_{max}} r^2 P(r) dr}{2 \int_0^{D_{max}} P(r) dr} \tag{2.1}$$

where $D_{max}$ is average maximum electron pair distance the value of $r$ when the $P(r)$ returns to zero.

As a comparison to our measurements of $A\beta_{42}$ and $\text{tau}_{352}$ in DMSO, we obtained the protein data bank (PDB) files of $A\beta_{42}$ peptide (1IYT), $A\beta_{42}$ fibrils (2MXU), $\text{tau}_{352}$ (1B5L) and simulated their scatter profiles from the given protein structures using FoXS web server. [74] FoXS computes a SAXS profile using information of a protein from a PDB file and the Debye formula. Scattering from the hydration layer around protein and the excluded volume are considered in the Debye model by incorporating them as adjustable parameters in the form factor to estimate a SAXS profile. All of the scatter profiles from PDB files were computed with default parameters. By default, the maximum $q$ value was 5 $\text{nm}^{-1}$ and we used 500 points to generate each SAXS profile.

## 2.2 Results

We present the SAXS signals acquired and analyzed for $A\beta_{42}$ and $\text{tau}_{352}$ within 50% DMSO. Fig. 2.1(b) shows the SAXS signals for $A\beta_{42}$ in DMSO solvent (pH 8) at 37 °C after 5 min and after 4 days. The FoXS generated SAXS profiles of the $A\beta_{42}$ monomer and fibril are also shown for comparison. When plotted as Guinier curves

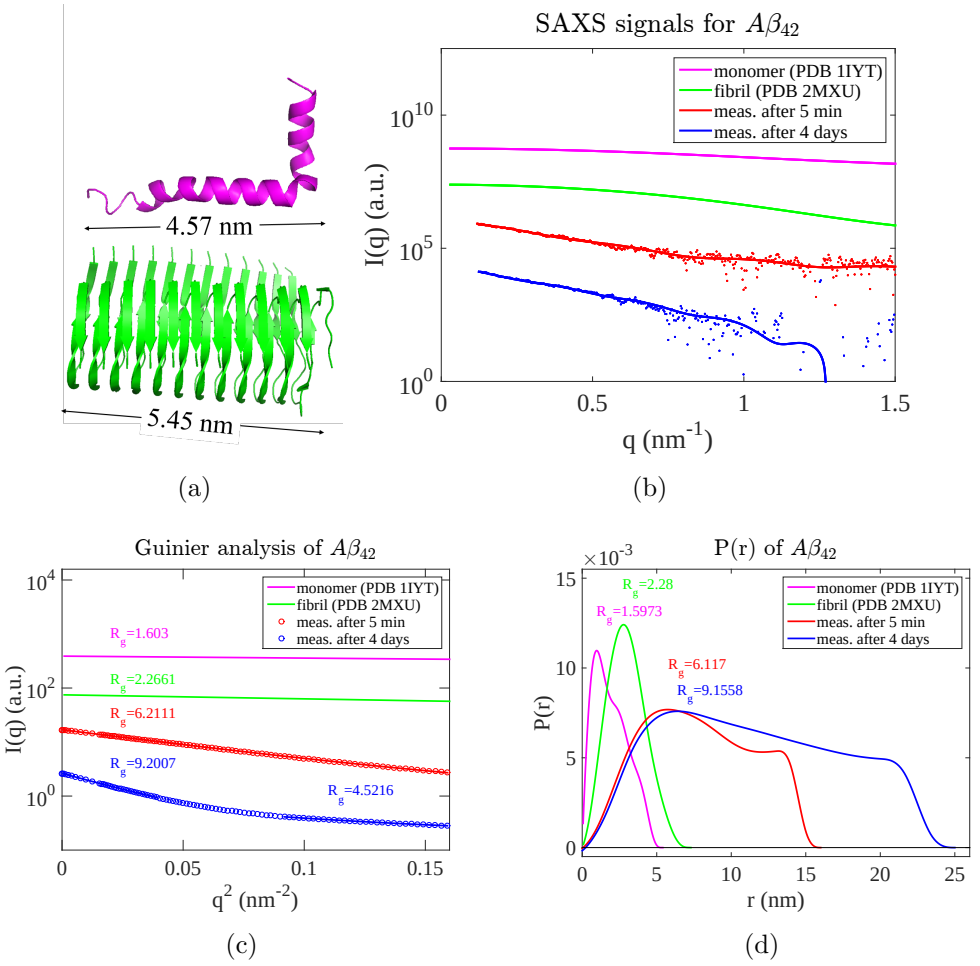


Figure 2.1: (a) Representation of the protein structures of $A\beta_{42}$ monomer (PDB 1IYT) in pink and fibril (PDB 2MXU) in green. (b) SAXS profiles for $A\beta_{42}$ from crystal structures of monomer and fibril obtained from the FoXS using PDB files, and from SAXS measurements of $A\beta_{42}$ protein in DMSO after 5 min and after 4 days. The curves have been offset for clarity by factors of $10^{1.3}$, $10^{-1.9}$, $10^4$, and $10^2$ respectively. (c) Guinier plots with reported $R_g$ of $A\beta_{42}$ monomer and fibril crystal structures from PDB, and from SAXS measurements after 5 min and after 4 days. The curves have been offset for clarity by factors of $10^3$, $10^2$, $5 \times 10^4$, and $5 \times 10^3$ respectively. (d) $P(r)$ of $A\beta_{42}$ for monomer and fibril crystal structures from PDB, and from SAXS measurements after 5 min and after 4 days.

as shown in Fig. 2.1(c), the $R_g$ values of the proteins can be extracted from the slope of linear fit. Fig. 2.1(c) shows that the $R_g$ value of $A\beta_{42}$ increases from 6.2 nm to 9.2 nm after 4 days of measurement, indicating slow progression of aggregation with time. The Guinier curve of $A\beta_{42}$ after 4 days cannot be fitted with a single straight line and shows two different $R_g$ values (9.2 nm and 4.5 nm) in the low q region. This strongly suggests the formation of aggregates of two different size. Moreover, the experimentally measured $R_g$ value of $A\beta_{42}$ after 5 min is approximately four times bigger than of its own monomer crystal structure (PDB 1IYT). Interestingly, the size of the $A\beta_{42}$ fibril crystal structure (PDB 2MXU) is also approximately three times smaller than that of $A\beta_{42}$ measured after 5 min.

Fig. 2.1(d) shows the $P(r)$ of the SAXS profiles for $A\beta_{42}$. We report the $R_g$ values calculated using Eq. 2.1. The $R_g$ values calculated for $A\beta_{42}$ are similar to those calculated in Guinier analysis for the respective samples. In addition, both functions for the experimental samples have a wider spread for $r$ and a shoulder at the right tail end of the curve in comparison to the theoretical $P(r)$ calculated from their crystal structures. $D_{max}$ of $A\beta_{42}$ after 5 min is at least three times bigger than that of its monomeric crystal structure. Similarly, as shown in Fig. 2.1(d), $A\beta_{42}$ after 4 days has a wider spread than when it was measured after 5 min. This result suggests that $A\beta_{42}$ aggregation increases over time and we can use SAXS to characterize this aggregation. Nevertheless, it also suggest that the expected trend for $A\beta_{42}$ aggregation derived from their crystal structures is not consistent with experimental results. We observe the effect of protein-protein interaction and induced aggregation from features in the distribution, specifically by the shoulder

at the right tail of the curve and by the $D_{max}$.

Fig. 2.2(b) shows the SAXS signals for $tau_{352}$ in DMSO solvent at 37 °C measured after 5 min and after 4 days. The FoXS generated SAXS profiles of the $tau_{352}$ monomer is also shown for comparison. In Fig. 2.2(c), $R_g$ values around 14 nm were calculated for measured $tau_{352}$ SAXS profile in the low q region. A second $R_g$ was estimated by Guinier analysis to be 9-14 nm in a wider q region, which is significantly larger than the expected 1.6 nm determined from its monomer crystal structure, indicating significant aggregation of $tau_{352}$ in DMSO.

Fig. 2.2(d) shows the $P(r)$ of the SAXS profiles for $tau_{352}$. As observed with $A\beta_{42}$, the $R_g$ values calculated for $tau_{352}$ are close to those calculated in Guinier analysis for respective samples. The $R_g$ values calculated through both Guinier and $P(r)$ analysis were similar. In addition to this, the $P(r)$ of $tau_{352}$ measured after 5 min and then after 4 days appear nearly identical, indicating little to no change in aggregation over the course of 4 days. The characteristic symmetry and large $r$ at the maximum peak of the $P(r)$ suggest that, for both time points, $tau_{352}$ formed large, spherical oligomers and that $tau_{352}$ may have already reached steady-state aggregation.

## 2.3 Discussion

The results of this study show that various aggregation levels of AD proteins, $A\beta_{42}$ and $tau_{352}$, can be characterized with SAXS. In this paper, we focused on one particular solvent condition (50% DMSO solution) in which these proteins were

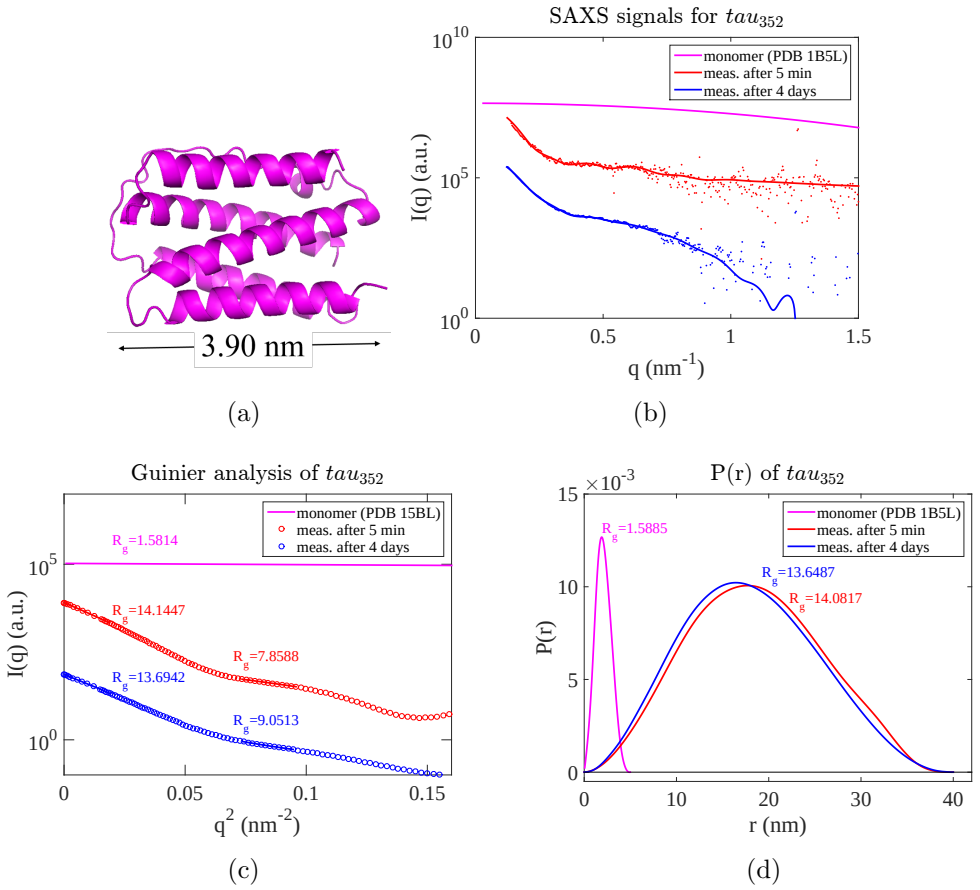


Figure 2.2: (a) Representation of protein structure for tau$_{352}$ monomer (PDB 1B5L). (b) SAXS profiles from crystal structure of monomer obtained from FoXS using PDB file, and from SAXS measurements of tau$_{352}$ protein in DMSO after 5 min and after 4 days. The curves have been offset for clarity by factors of 1, $10^2$, and $10^4$ respectively. (c) Guinier plots with reported R$_g$ for monomer crystal structure, and for SAXS measurements after 5 min and after 4 days. The curves have been offset for clarity by factors of $10^7$, $10^5$, and $10^3$ respectively. (d) $P(r)$ of $tau_{352}$ for monomer and fibril crystal structures from PDB, and from SAXS measurements after 5 min and after 4 days.

hypothesized to remain monomeric because of the stabilizing interaction of DMSO and the high pH of the solution. One likely reason behind this is that DMSO at this concentration preferentially binds to the hydrophobic side chains of the amino acids and prevent the hydrophobic interaction which is one of the driving forces of protein aggregation. On the other hand, pH changes in the solution modulates the electrostatic interaction among proteins depending on their individual net charge. For instance, in the case of pH 8, the net calculated charge of $A\beta_{42}$ is -3.4. Due to their negative charges, there should be an effective repulsion among $A\beta_{42}$ proteins to maintain their native monomeric states. Nevertheless, aggregation for both $A\beta_{42}$ and $\text{tau}_{352}$ samples were observed with SAXS in the 50% DMSO solution contrarily to what we expected.

Our SAXS analysis suggests aggregation of both $A\beta_{42}$ and $\text{tau}_{352}$. In particular, we found that $\text{tau}_{352}$ aggregates at a faster rate to reach the steady state after 5 min, whereas $A\beta_{42}$ aggregation slowly progresses with time. One possible reason behind the aggregation is due to the concentration effect. The concentration of $A\beta_{42}$ and $\text{tau}_{352}$ were 5.6 mg/mL and 1.43 mg/mL respectively. Due to their high concentration, the aggregation is likely to occur despite the unfavourable hydrophobic interaction and electrostatic repulsion imposed by the solvent. The concentration of DMSO in water was not high enough to bind to every peptide present at high concentration to prevent the aggregation. In any case, the concentration dependent study of both protein and DMSO needs to be done to further understand the mechanistic part of protein aggregation shown by SAXS data.

The differences in scatter profile between measured samples and PDB could be

attributed to the fact that calculations of scatter using the PDB are of a single protein in every orientation averaged, whereas, experimental measurements are more complex containing of a distribution of protein aggregates, orientation, and conformations. In addition, a nuclear magnetic resonance technique was used to inform the PDB file for these proteins. Therefore, differences between the measured sizes of the protein and the PDB information could be due to differences in measurement techniques.

Future work includes validating the measurements obtained with repeat measurements, as well as with other laboratory techniques including dynamic light scattering (DLS), UV-vis spectroscopy, and thioflavin T fluorescence assay. Also, we plan to compare measurements of these proteins taken at different time-points for AD proteins dissolved in a variety of solvents. After characterizing the SAXS measurements of these AD proteins at various aggregation in steady-state, the obtained scatter signals will be converted to absolute cross sections using a water standard.These cross sections can then be converted to input material files for MC-GPU simulations to determine feasibility of AD imaging *in vivo* with various sample and instrument geometries. [9, 19]

## 2.4 Conclusion

We report SAXS measurements of $A\beta_{42}$ and $\text{tau}_{352}$ in 50% DMSO at two time points. 50% DMSO was initially chosen as a buffer because proteins are reported to remain monomeric in this solution, however we observed aggregation and growth

between measurements at 5 min after sample preparation, and 4 days. The signals measured even after 5 min were different than theoretical scatter profiles generated using PDB structures. $\beta$ amyloid and tau were difficult to control *in vitro* and may not behave the same way *in vivo*, therefore, we determined it would be more useful to measure the plaques and tangles *ex vivo* for a closer approximation to our target signals *in vivo*.

# Chapter 3: Incorporating experimental cross sections into MC x-ray transport calculations

In this chapter, we describe and validate a fully detailed Monte Carlo x-ray transport simulation technique that utilizes user-provided cross sections to describe x-ray interaction in virtual samples and explore SAXS instrument design choices. We validate the accuracy of the simulation code with sample material cross sections derived from analytic models and empirical measurements of a homogeneous spherical gold nanoparticle (GNP) monomer, dimer, and heterogeneous mixtures of the two in a water solvent. Analytic and measured scatter profiles from these samples were converted to cross sections using an absolute water standard. Our Monte Carlo estimates of the fraction of dimers from analytically-derived and empirically-derived cross sections are strongly correlated with less than 1.5% and 16% error respectively to the expected concentration of monomer and dimer species. In addition, we simulated a variety of monoenergetic x-ray beams to investigate coherent scattering versus radiation dose for a range of sample sizes. For GNP spheres in a water solvent, the energy range that produces the most coherent scatter at the detector per deposited energy was between 31 and 49 keV for sample thickness of 1 mm to 10 cm. The method we describe for the detailed simulation of SAXS using

measured and modeled cross sections will enable instrumentation optimization for *in vivo* molecular imaging applications.

## 3.1 Introduction

There are an increasing number of imaging applications for small-angle x-ray scattering (SAXS) using scanning [32] and tomographic methods [46, 75]. We have proposed a particular biomedical application that utilizes SAXS molecular imaging of probed protein-protein interactions [6]. SAXS imaging is a promising alternative tool for *in vivo* molecular imaging because the coherent scatter provides nanostructural information about a sample without the need for destructive sample preparation techniques. Other biomolecular interaction characterization methods, such as positron emissions tomography (PET), fluorescence resonance energy transfer (FRET), and bioluminescence resonance energy transfer (BRET), have low spatial resolution, poor specificity, or inherently lack the capability for deep tissue imaging. Well-defined SAXS signatures from high-contrast molecular probes, such as gold nanoparticles (GNPs), could be correlated with the presence of biomolecular interactions and provide a higher specificity option that is able to image protein-protein interactions *in vivo* in deep tissue. It was demonstrated that GNP signals could be determined even within a complex background such as E. coli lysate [6]. However, concerns remain regarding the long measurement times and the excessive amount of energy deposited into live samples. Simulations of the entire SAXS imaging chain allow us to study various instrumentation geometries for a given application without

time, safety, and monochromatic source energy limitations typical of measurements.

We present a code that simulates x-ray transport from source to detector in a SAXS instrument. The code allows user-provided cross-sections derived from measurements or analytic models to describe how the x-ray interacts in voxelized virtual samples. For more complex biological materials that cannot be described analytically such as soft tissue, adipose, and bone, this construct allows users to measure cross sections of materials individually with optimal sample thickness and instrument settings and then simulate a more realistic sample geometries which includes effects from multiple materials superimposed. We validate the simulations with well-defined cross sections consisting of a homogeneous gold nanoparticle (GNP) sphere, dimerized GNP spheres, and the weighted sum of the former two cross sections in ratios of 2:1, 1:1, and 1:2 in a water solution as non-interacting and interacting SAXS signals at varying levels. These cross sections are derived both from analytic modeling and from measurements of GNP spheres with radius of 6.75 nm in water, dimerized GNPs in water with similar concentration, and the two former solutions in the same aforementioned volumetric ratios as the model. We describe the procedure of converting scatter intensity profiles to cross sections that can be used as inputs to the simulations. After simulation of the SAXS instrument measurement of virtual samples, a previously developed method [6] was used to extract from scattering profiles the required information regarding the fraction of interacting particles in a solution and the size of monomers and dimers.

To illustrate the use of our tool, we explore the effect of varying the monochromatic source energy and the sample thickness and evaluate deposited energy and

intensity of coherent x rays when varying parameters of energy and sample thickness.

## 3.2 Methods

### 3.2.1 SAXS simulations

The code we present is based on MC-GPU [9], a publicly available GPU-accelerated x-ray transport simulation tool that is used to generate clinically-realistic images and radiation dose estimations for a number of x-ray imaging modalities (Radiography, Computed Tomography [10], Digital Breast Tomosynthesis [64]). It uses Monte Carlo techniques to simulate large number of x ray trajectories which interact with material atoms in a voxelized geometry based on advanced physics models from PENELOPE 2006 [73]. The x-ray path is determined by random sampling probability distribution functions that decide whether the x ray is scattered, transmitted, or absorbed. Cross sections of the materials the x ray travels through is used to determine these probability distribution functions. The inherent benefit of this tool is that it allows for separation of primary, Compton, Rayleigh, and multiple-scatter x rays contributions, a dose estimation on the sample, use of a complex voxelized sample geometry, the inclusion of realistic source and detector models, and study of various collimation geometry effects.

The form factors for homogeneous materials are by default calculated in MC codes with an independent atomic approximation (IAA) which combines the form factor of the individual atoms in the material according to their relative atomic

weight fraction:

$$F_{IAA}^2(q) = \sum n_Z F_Z^2(q), \tag{3.1}$$

where $n_Z$ is the weight fraction of element $Z$, $F_Z(q)$ is the atomic form factor for element $Z$, and $q$ is the momentum transfer defined as:

$$q = 4\pi \frac{sin(\theta)}{\lambda}, \tag{3.2}$$

where $\lambda$ is x-ray source wavelength, and $2\theta$ is scattering angle.

To simulate realistic x-ray scattering from particles, molecules, and tissues at small angles, MC-GPU was modified to allow user-provided cross sections of materials that that capture both the form factor and the structure factor effects [28].

The differential coherent cross section is described by:

$$\frac{d\sigma}{d\Omega}(q) = \frac{d\sigma_T}{d\Omega}(q) F_{IAA}^2(q) s(q), \tag{3.3}$$

where $d\sigma_T/d\Omega$ is the classical Thomson cross section for scattering by a free electron at rest, and structure factor, $s(q)$, accounts for the interference effects between the scattered photons.

### 3.2.2 Cross sections

Empirical measurements and analytic scatter models of a controllable surrogate protein-protein interaction system consisting of monomeric GNP spheres,

dimerized GNP spheres, and a mixed ratio of these two particles are used to generate cross sections for validation of the simulations of SAXS using MC-GPU. We simulate a full SAXS instrument using theoretical and measured cross sections of samples.

### 3.2.3 Empirical measurements

The sample system was synthesized monomeric GNP spheres with radius of 6.75 nm and dimerized GNP spheres of same radii dissolved in water. The concentration of the GNP monomer and dimer solutions were both $7.0 \times 10^{11} \pm 0.5 \times 10^{11}$ GNPs per mL as estimated by UV-Vis. The two solutions were mixed with volumetric ratios of 1:0, 2:1, 1:1, 1:2 and 0:1. These five samples and water were empirically measured with our laboratory SAXS instrument (SAXSpace, Anton Paar, Ashland, VA, USA). The instrument utilizes a Cu $K_\alpha$ radiation ($\lambda = 0.154$ nm) and was configured in Kratky block line collimation mode. The CCD camera had a pixel pitch of 24 $\mu$m in an array of 2084x2084 pixels. Samples were loaded into the system via a 1-mm diameter quartz capillary positioned at a distance of 305.3 mm from the CCD. The accessible $q$-range was 0.0732–1.66 $nm^{-1}$. The entire beam path was enclosed in vacuumed space with a pressure below 3 mbar to limit undesirable scatter from air. The CCD pixels were binned along the length of the beam (2 cm). For each measurement, 2400 frames were obtained at 1 s exposures and averaged. The smeared line-collimated data was desmeared using indirect Fourier transform method [31] with 20 splines between 0 and the *a priori* estimate of the longest pair

distance in the particle, $D_{\max}$. $D_{\max}$ was initially estimated and then adjusted until the $p(r)$ shown near $D_{\max}$ did not descend sharply, go negative, or oscillate. We used 29 different stabilization values, $\alpha$, of $10^n$ for $n$ from -4 to 10 in steps of 0.5 which we found to be a sufficient range in finding an appropriate $\alpha$ and set of weights. The appropriate $\alpha$ chosen was determined by following procedures outlined by Glatter et. al [31]. The $\alpha$ for the probe solution was 5, and ranged between 2.5 and 4.5 for the dimer solution and mixes.

### 3.2.4 Analytic models

As a noise-free comparison, scatter profiles of GNP monomer spheres, dimers, and the mixture of the two were also analytically-derived using spherical form factor and a dimer structure factor. To calculate the analytic model scatter of the GNP solutions we used the form factor of a monomeric homogeneous sphere [66],

$$F_{\mathrm{m}}(q,R) = \frac{3[sin(qR) - qRcos(qR)]}{(qR)^3}, \tag{3.4}$$

where $R$ is the sphere radius. We chose a $R$ of 6.75 nm which was the approximate radius of our GNP samples. The scattering intensity of spheres, $I_{\mathrm{m}}$, is described by $I_{\mathrm{m}}(q) = KF_{\mathrm{m}}^2(q,R)$, where $K = n\Delta\rho^2V^2$ ($n$ is the number of particles, $\Delta\rho$ is the difference in electron density between particles and solvent, and $V$ is volume of a particle). For our model, $K$ was a scaling factor to the scattering intensity of our measured scatter of GNP spheres. We applied a structure factor to take into account the interference effect of two interacting spheres. The structure factor multiplied by

$I_{\mathrm{m}}$ is the scattering intensity of a dimer [48],

$$I_{\mathrm{d}}(q,s) = I_{\mathrm{m}}\left(2 + 2\frac{\sin(qs)}{qs}\right), \tag{3.5}$$

where $s$ is the center-to-center spacing of the spheres in a dimer. For our model, we chose $s$ =20 $nm$ which is within a range of distances at which proteins interact. The SAXS profile for a our sample material, $I_{\mathrm{M}}(q)$, is the weighted sum of the contributions from monomers, $I_{\mathrm{m}}(q)$, and dimers, $I_{\mathrm{d}}(q)$:

$$I_{\mathrm{M}}(q) \approx \omega_{\mathrm{m}} I_{\mathrm{m}}(q) + \sum_{s} \omega_{\mathrm{d}}(s) I_{\mathrm{d}}(q,s), \tag{3.6}$$

where $\omega$ is the weight for relative monomer concentration and dimer concentrations with a distribution of center-to-center spacings, $s$.

### 3.2.5 Absolute scaling by secondary water standard

Scatter intensity profiles of model and measured cases were converted to material cross sections by calibrating to a water standard [62] using the following equation,

$$\frac{d\sigma}{d\Omega}_{M}(q) = \frac{I_W(0)}{I_M(0)}\frac{I_M(q)}{I_W(q)} \times \frac{d\sigma}{d\Omega}_{W}(q), \tag{3.7}$$

where $\frac{d\sigma}{d\Omega_M}(q)$ is the differential cross section of the material of interest, $I_M(q)$ and $I_W(q)$ are the scatter profiles of the material and water respectively. $\frac{d\sigma}{d\Omega}_W(q)$ is the known differential cross section of water which is relatively constant at 0.01632 $\mathrm{cm}^{-1}$ within the $q$-range 0–12 $\mathrm{nm}^{-1}$. $I_M(0)$ and $I_W(0)$ are the primary beam intensities

of the material and water respectively.

The scatter intensity of both analytic model and experimentally measured samples are converted to cross sections to be assigned to sample material voxels in the simulations. The MC estimates of both the modeled and measured cross sections are compared to evaluate the performance of the MC acquisition model.

### 3.2.6 Validation

The geometry of the SAXS instrument is shown in Fig. 6.1 The distance of the front edge of the sample to the detector was fixed at 29 cm. The x-ray source was an infinitely small monochromatic pencil beam. The x-ray energy used was 8 keV. The detector was 2x2 $cm^2$ with 1200x1200 pixels and had 100% detection efficiency. Fig. 3.2b shows a block diagram of the inputs to MC-GPU. The sample geometry was a 1x1x$z$ cm box where $z$ is the thickness along the beam path. For the study of interaction fraction of our analytic models and empirical data, we used $z = 1$ mm which is the thickness of our instrument capillary. $10^{12}$ primary x rays were simulated for each SAXS acquisition and took approximately 6 minutes to complete in our computer containing 6 NVIDIA GeForce GTX Titan GPUs. The image at the detector was radially averaged. The process was repeated 10 times for calculating the statistical uncertainty.

We extended the validation of simulated SAXS profiles to an interaction fraction figure-of-merit [6] which in our application quantifies the fraction of dimers in a given sample. The interaction fraction is calculated using a fitting algorithm

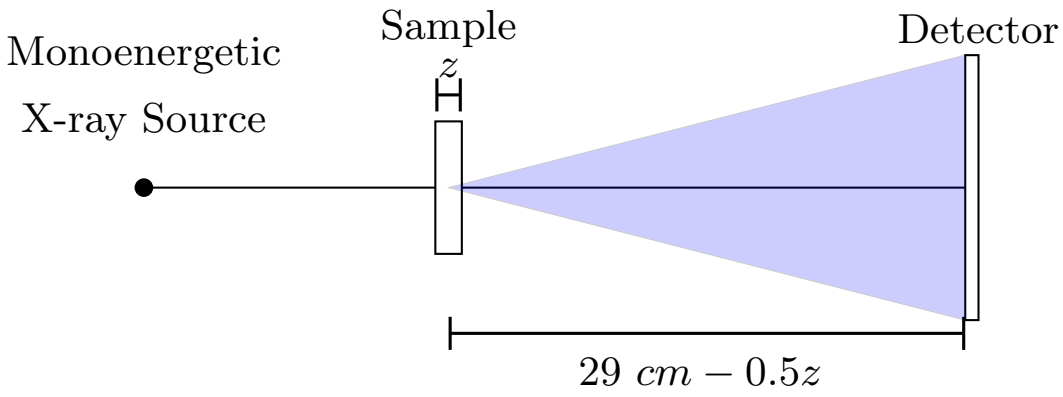


Figure 3.1: Schematic of instrument geometry used in simulations.

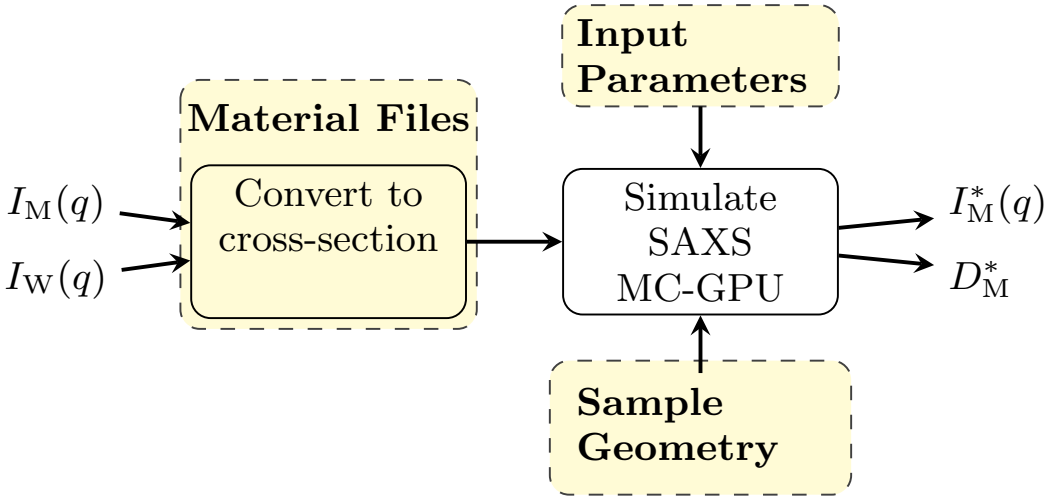


Figure 3.2: Block diagram of inputs and outputs of MC-GPU for SAXS. $I_M(q)$ and $I_W(q)$ are the empirical scatter profiles for a material of interest and water. $I^*_M(q)$ is the simulated scatter profile. $D^*_M$ is the calculated total dose on the sample.

(MATLAB 'lsqnonneg' function) incorporating positivity constraint to minimize a least squares objective,

$$\min_{\omega} ||C\omega - I_{\mathrm{M}}^{*}||_2^2, \tag{3.8}$$

with $I_{\mathrm{M}}^{*}$ as the simulated scatter profile of a given material. The basis functions, $C$, corresponding to analytic expressions for a monomer and several dimers with varying $s$ (see section 3.2.4), are assembled into a matrix,

$$C = \begin{bmatrix} I_{\mathrm{m}}(q) & I_{\mathrm{d}}(q, s_{\min}) & \dots & I_{\mathrm{d}}(q, s_{\max}) \end{bmatrix} \tag{3.9}$$

The interaction fraction is calculated by the weights assigned to each basis function:

$$\mathcal{I} = \frac{\sum_s \omega_{\mathrm{d}}(s)}{\sum_s \omega_{\mathrm{d}}(s) + \omega_{\mathrm{m}}}. \tag{3.10}$$

The interaction fraction of weighted sum scatter curves from the analytic model of monomer and dimers matched exactly the expected dimer weights using this algorithm. The dimer fractions were 0, 0.33, 0.5, 0.66, and 1 which were the estimated volumetric fractions for dimerized GNPs in our measured samples. To improve the realism of the simulations, we added the absolute cross section of water as a constant (See section 3.2.5) to the analytic scatter cross sections to mimic the GNP monomer and dimers that were measured in a water solution. The resulting simulated scatter profiles were corrected by subtracting a separately simulated water scatter with the same sample geometry.

Equation 3.8 was fit over a $q$-region from 0.0732–1 $\mathrm{nm}^{-1}$ with a $\Delta q$ of 0.0032.

This range of $q$ was selected because it contained the differentiating feature in the scatter profile indicative of dimers.

### 3.2.7 Application to instrument design

After validating MC-GPU for SAXS using analytic models and measured data, we studied the SAXS system design varying the source energy and sample thickness. The same instrument geometry was used as shown in Fig. 3.2a, however energy was varied from 5 to 95 keV in steps of 1 keV and $z$ was varied 0.1, 0.5, 5, and 10 cm. We used the analytic monomer scatter cross section for the sample material because it was well defined and devoid of various sources of noise as opposed to the measured monomer scatter. $1 \times 10^{12}$ primary x rays were simulated.

## 3.3 Results

Fig. 3.3 shows the scatter profiles of the analytic model before and after simulation. The interaction fraction of these simulated curves is shown in Fig. 3.4(a) and Fig. 3.5. The simulation results accurately match the input analytical cross sections with a constructed $s$ of 20 nm. The error between simulated interaction fractions and the weights applied to analytic monomer and dimer scatter was less than 1.5%, likely due to differences in the flat water cross section addition and simulated water subtraction containing Poisson noise. This caused peaks to occur at the boundaries of the dimer $s$ distribution and at 21 nm.

The results from simulated measured scatter curves of our GNP samples are

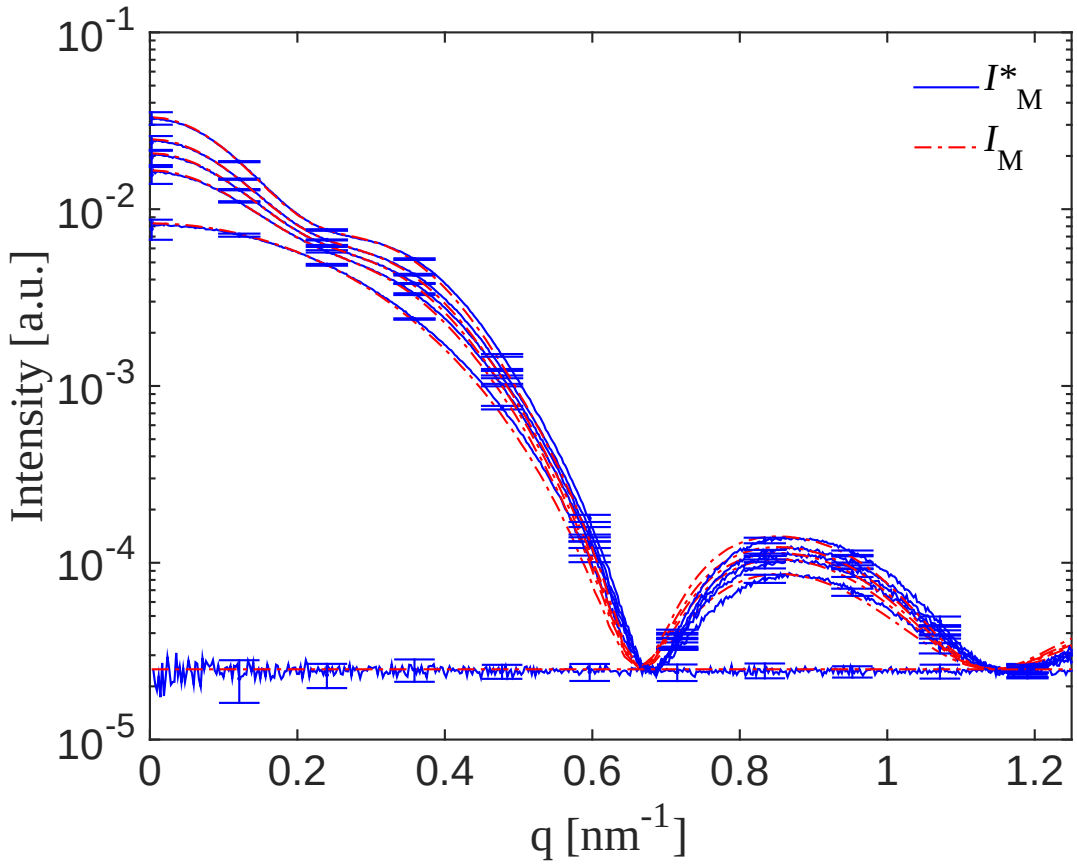


Figure 3.3: Scatter profile of the analytic ($I_M$) model of GNP spheres in water and average scatter profile of 10 simulations ($I^*_M$) of that model with different monomer and dimer ratios. From bottom to top the scatter is of water, GNP monomer, 2m:1d, 1m:1d, 1m:2d, and dimer in a water solvent. Error bars are the standard deviation of 10 repeated simulations for every 50 points for clarity. The simulated scatter profiles match the input scatter profiles from analytic models giving indication there is little bias from simulations.

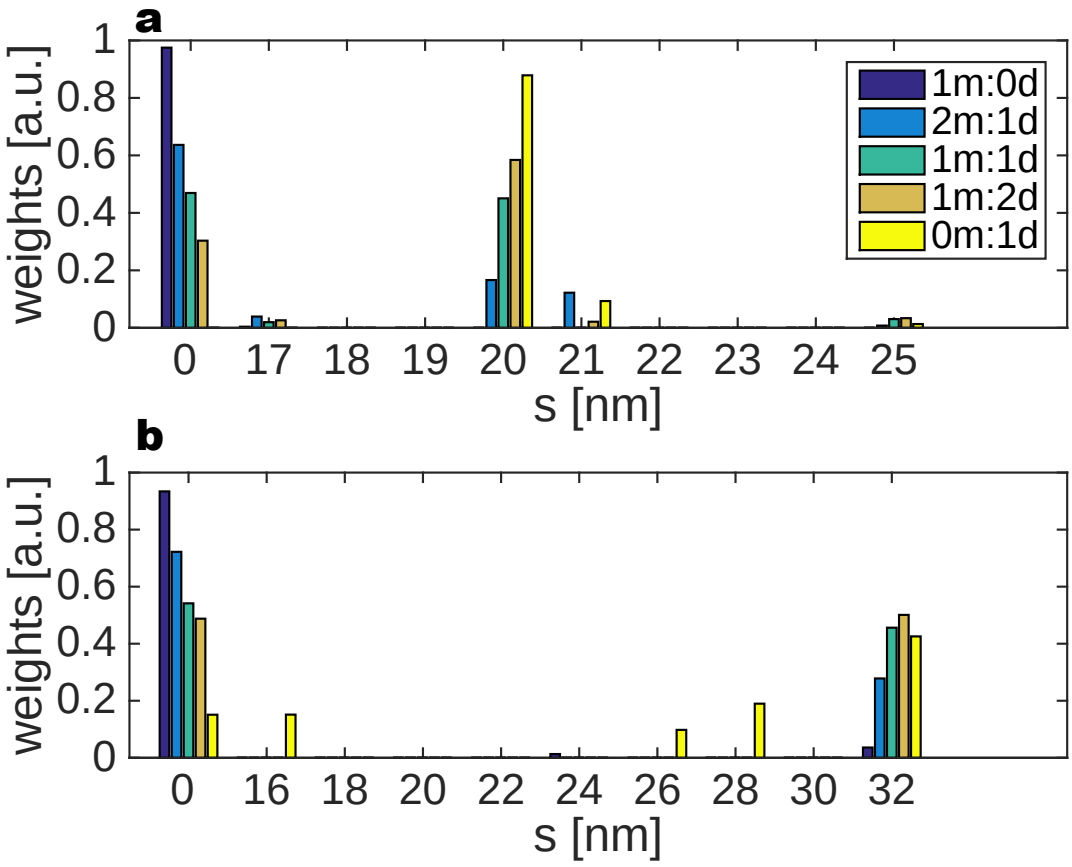


Figure 3.4: Distribution of GNP center-to-center spacing, s, for 5 scatter profiles with different ratios of monomer 'm' and dimer 'd' scatter estimated from simulations using analytically-derived cross sections (a) and empirically-derived cross sections (b). The analytically-derived cross sections were constructed to have an $s$ of 20 nm, whereas the empirically-derived cross sections were found to have an $s$ of around 32 nm.

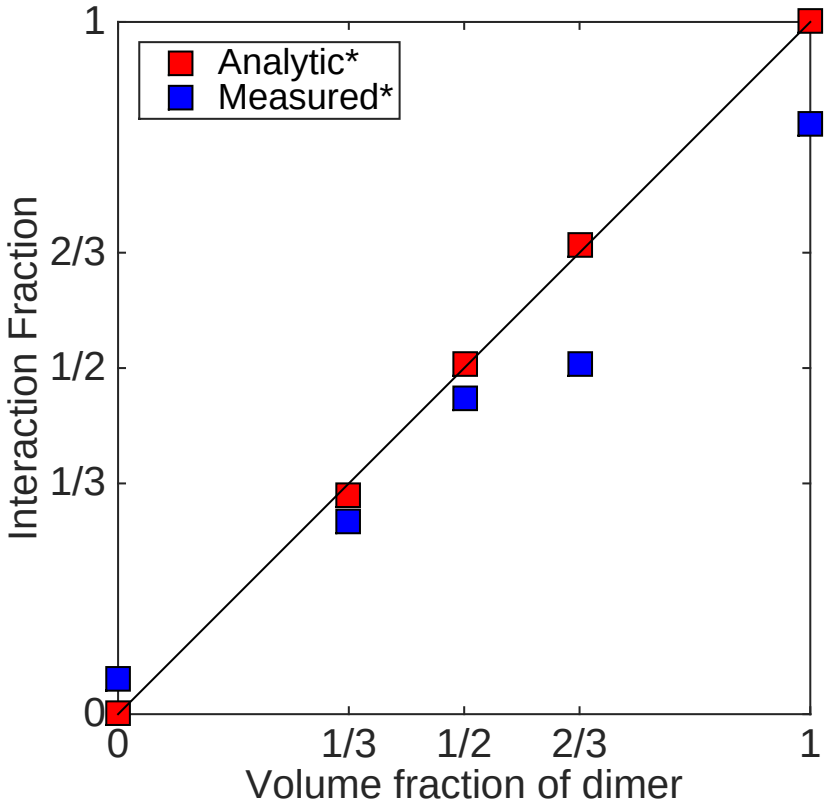


Figure 3.5: Correlation plot of volumetric fraction of dimers and interaction fraction estimated from simulations using analytic and measured cross sections.

shown in Fig. 3.4(b) and Fig. 3.5. The $s$ of the dimers were unknown at time of measurements but from information gleaned from fitting analytic curves suggested that the dimers have an $s$ of 32 nm which coincides what was reported in our previous work for these samples [6]. The interaction fraction error was less than 16%. The difference in this comparison could be attributed to several factors. First, the monomer GNP solution could have a distribution of sizes. Second, there is likely to exist some monomer and different $s$ dimers in our dimer solution. And lastly, there could be an imperfect background subtraction which was also seen in the analytically-derived cross-section simulations.

Fig. 3.6 shows the scatter profiles from simulations with varying energies and $z$. The energy was varied from 5 to 95 keV in steps of 1 keV and $z$ was selected to be 0.1, 0.5, 5, and 10 cm.

Fig. 3.7(a) shows the sum of scattering photons, $I$, within a momentum transfer of 0 and 2 $nm^{-1}$, over the total number of primary photons simulated for each sample, $H$. The maxima in these plots are indicative of the energies that produce the most coherent scatter within the angular range of interest for a fixed number of primaries which is proportional to exposure time. Fig. 3.7(b) shows the energy deposited, $E_D$ on the sample per incident photon, $H$.

Fig. 3.7(c) shows the number of scattered photons over the deposited energy ($U = I/E_D$). The peak energy of these plots is optimum in terms of the maximum amount of scattered photons with the least amount of deposited energy. In other words, the x-ray utilization, $U$, which is the ratio of scattering intensity across all angles of interest and the deposited energy in the object.

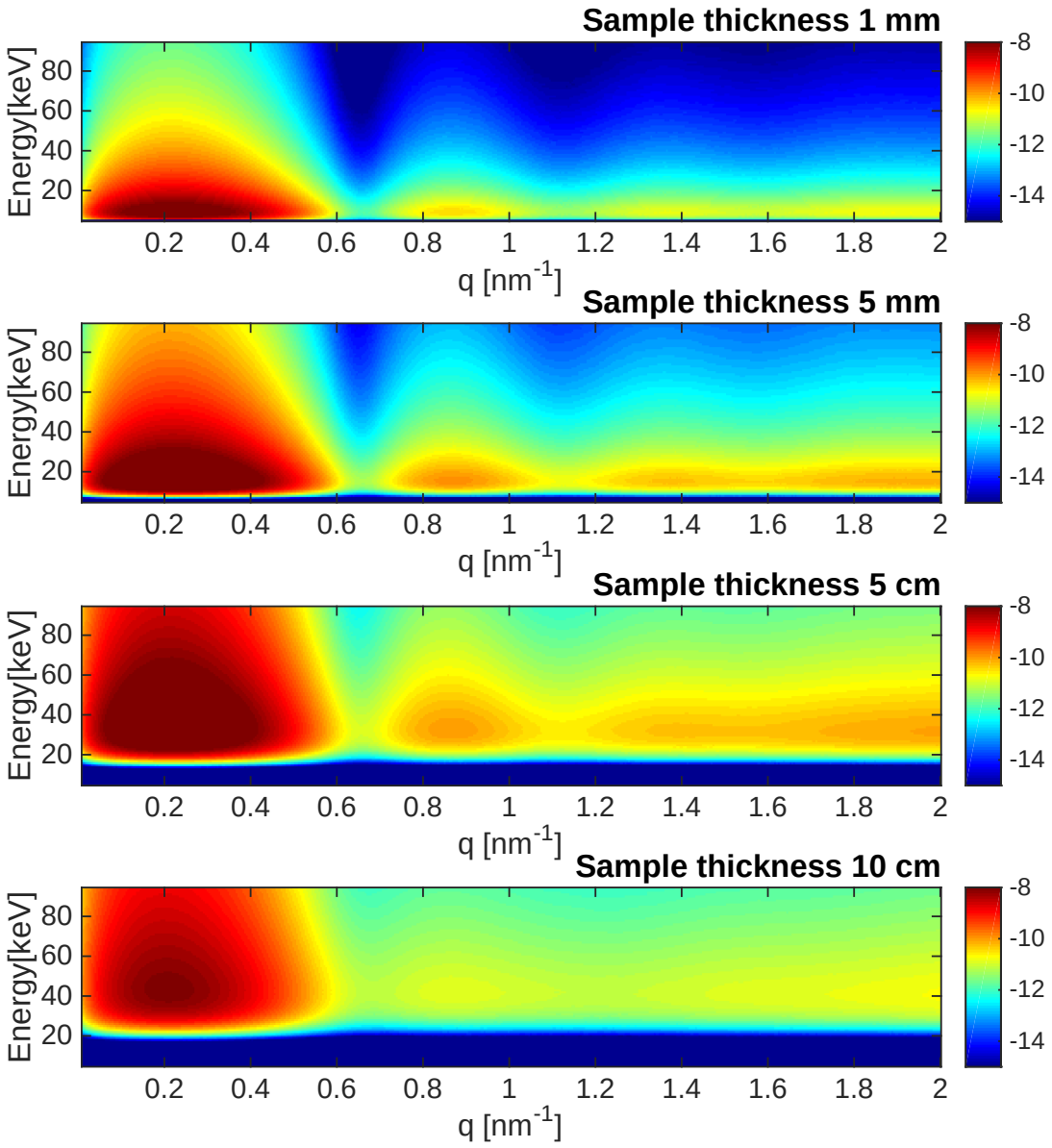


Figure 3.6: Scatter profiles of analytic GNP monomer for energies 5 to 95 keV and sample thicknesses of 0.1, 0.5, 5, and 10 cm. Colorbar is in logscale and represents scatter intensity [a.u.].

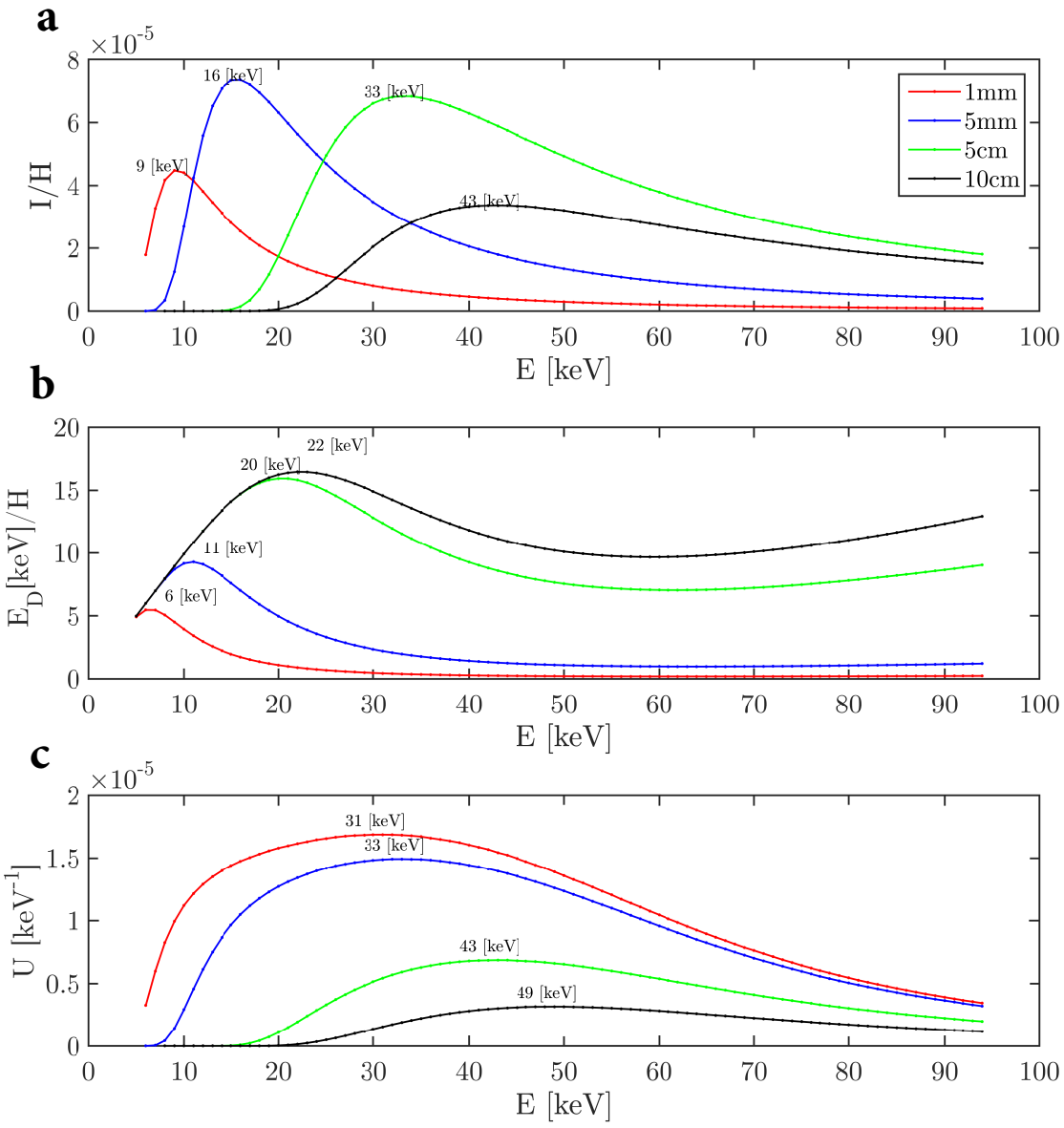


Figure 3.7: (a) This plot shows the number of scattered photons, $I$, between a $q$ of 0 and 2 nm$^{-1}$ over total number of photons simulated, $H$, as a function of the x-ray energy for different sample thicknesses. (b) Plot of the energy deposited on sample, $E_D$, over $H$. (c) Plot of the utilization energy, $U$, which is $I$ divided by $E_D$. The maximum $U$ indicates the energy which produces the largest number of scattered photons per energy deposited on sample. Inserted text indicates the energy at the maxima.

## 3.4 Discussion

We qualitatively confirm there is little to no bias added to scatter profiles from MC-GPU code because the simulated scatter profiles match the input scatter profiles from analytic models as seen in Fig. 3.3. This demonstrates the software can successfully simulate complete SAXS acquisitions in the computer.

Our findings show that simulations extended to the interaction fraction figure-of-merit using analytically-derived cross sections produces very little error (<1.5%) with respect to analytical models. The main source of error is primarily due to subtraction of a simulated noisy solvent. The comparison of the analytically-derived to the empirically-derived cross sections allows us to validate the methodology. Differences in the interaction fractions of the measured cross section and the expected results (Fig. 3.5) are not due to errors in the measurement, but, on the contrary, due to error in our estimated interaction fractions based on volumetric ratios of GNP monomer and dimer solutions.

Simulations which varied energy and sample thickness corroborated our expectations that scatter information detected is greatly reduced for thicker samples with lower x-ray energies. For example, in Fig. 3.6, very little scatter information was detected for x-ray energies below 20 keV for samples with 10 cm sample thickness, however, using higher energy x rays could recover some of the scatter data within a limited angular range.

Some SAXS applications require a short measurement time, in which case, the optimal energy would be one that produces the most coherent scatter at the detector

in an angular range of interest regardless of dose. In Fig. 3.7, for sample thickness of 1 mm, simulations showed that 9 keV x rays produced the most coherent scatter in the angular range of interest which agrees with design choices of many laboratory SAXS systems that use Cu $K_\alpha$ x rays (around 8 keV) with 1 mm thick sample holders.

For *in vivo* applications where dose minimization is desirable, the optimal energy is one that balances having more coherent scatter at the detector in an angular range of interest and reduced energy deposited in the sample. This optimal energy for *in vivo* applications is at the maximum utilization, $U_{max}$, where $U$ is the sum of scattered photons, $I$, over an angular range of interest divided by the energy deposited in the sample, $E_D$, for each energy, $E$. For our GNP sample in water with a thickness of 1 mm, energy at $U_{max}$ was 31 keV. For the same sample with a thickness of 10 cm, energy at $U_{max}$ was 49 keV. Some caveats are the energy at $U_{max}$ depends on the cross section of the sample measured, the angular range of interest, sample geometry, and instrument geometry. We show that simulations can be used for SAXS system design optimization based on a particular sample and application.

There are many benefits to using MC-GPU for simulations of SAXS. The simulated scatter profiles allow us to estimate contributions from Compton, Rayleigh, and multiple-scattered and primary x rays. For additional realism, the ideal detector could be replaced with models of detectors by varying detection efficiency and the x-ray pencil beam could be replaced with a cone beam with a variety of different collimation system designs. Simulations could be repeated for system variance estimations which may not be possible in experimental measurements due to changes

in the sample over time and experimental error. In addition, user-provided cross sections from empirical measurements of complicated biological materials could be assigned to materials in virtual phantoms of small animals and human heads and simulated with our code to investigate potential *in vivo* applications of SAXS [43,49].

## 3.5 Conclusion

We have utilized and validated MC-GPU to simulate x-ray transport in a full SAXS system using empirical cross sections to describe x-ray interactions in virtual samples. This method allows the investigation of factors that affect design choices given thicker and more complex samples (i.e., the monochromatic x-ray energy, and if safety is a concern, the amount of energy deposited in the sample). We have shown that MC-GPU simulation of x-ray transport in SAXS could be used to optimize instrumentation to produce the most scatter in an angular range given a fixed primary number of x rays and estimate radiation energy deposited on a sample. MC-GPU is open source and publicly distributed online for free. This work was critical to enabling realistic simulations of SAXS imaging for medical applications in the coming chapters.

# Chapter 4: MC Simulations of simplified SAXS-CT imaging system

We used a publicly available MC-GPU code to simulate x-ray trajectories in a SAXS-CT geometry for a target material embedded in a water background material with varying sample sizes (1, 3, 5, and 10 mm). Our target materials were water solution of gold nanoparticle (GNP) spheres with a radius of 6 nm and a water solution with dissolved serum albumin (BSA) proteins due to their well-characterized scatter profiles at small angles and highly scattering properties. The background material was water. Our objective is to study how the reconstructed scatter profile degrades at larger target imaging depths and increasing sample sizes. We have found that scatter profiles of the GNP in water can still be reconstructed at depths up to 5 mm embedded at the center of a 10 mm sample. Scatter profiles of BSA in water were also reconstructed at depths up to 5 mm in a 10 mm sample but with noticeable signal degradation as compared to the GNP sample. This work presents a method to study the sample size limits for future SAXS-CT imaging systems.

## 4.1 Introduction

Coherent scattering allows for detailed tissue characterization and added contrast compared to transmission x-ray and computed tomography (CT) imaging [46]. However, challenges remain for the technique to be used clinically. Among them, measurement times must be reduced, microfocus x-ray sources must be further developed for smaller beam sizes and higher flux, and total radiation dose must be estimated and possibly reduced. In this context, a methodology to measure the limitations regarding sample depth of a SAXS imaging system has yet to be developed. When these challenges are met, small-angle x-ray scattering CT (SAXS-CT) for in vivo imaging will represent a powerful diagnostic tool for a number diagnostic applications. In this work, we present a preliminary description for a method to study the sample size limit of SAXS-CT which depends on instrumentation design, cross-section strength of the molecular targets and background materials.

## 4.2 Methods

We used a publicly available, GPU-accelerated, Monte Carlo tool (MC-GPU [9]) to simulate a large number of x-ray trajectories. MC-GPU has been used and validated to generate clinically-realistic images and accurate radiation dose estimates for a number of x-ray imaging modalities (radiography, computed tomography [10], digital breast tomosynthesis [93]). The code was recently modified for a SAXS-CT geometry with increased cross-section sampling at small scattering angles and to

allow user-generated cross sections of particular materials to account for molecular interference effects [19, 28].

Small-angle cross sections were obtained via experimental measurements or online small-angle scatter databases and converted to an input material file for MC-GPU. For our target material, we have used cross-sections of monomeric gold nanoparticle (GNP) spheres with a radius of 6 nm as the target dissolved in water, and bovine serum albumin (BSA), dissolved in water as shown in Fig. 4.1. The GNP samples were first measured and theoretical scatter curves of ideal spheres were fit and scaled to the intensity of our measurements [6].

We obtained BSA measurements from the SAS biological database [88]. BSA (ID: SASDA3) was measured using synchrotron radiation source in Hamburg, Germany. The cross section of water is a known constant of 0.587 $nm^2$ at small-angles between 0-12 $nm^{-1}$. It is represented in the standard manner scaling SAXS measurements to absolute values to obtain cross sections.

The geometry and location of the target material (GNP or BSA in water) is depicted in Fig. 4.2(a) as the inner yellow cylinder. The cross section of water was used for the background material depicted in Fig. 4.2(a) as the surrounding blue cylinder. We varied the depth of the target material by increasing the diameter of the background material while keeping the target material diameter at 3 mm. We used four sample geometries total: (1 and 2) control target material with no surrounding background material, (3) target material within a 5 mm diameter background, and (4) target material within a 10 mm diameter background. The sample geometries used voxels of 0.005 mm x, 0.005 mm y, and 1 cm z (reference axis shown

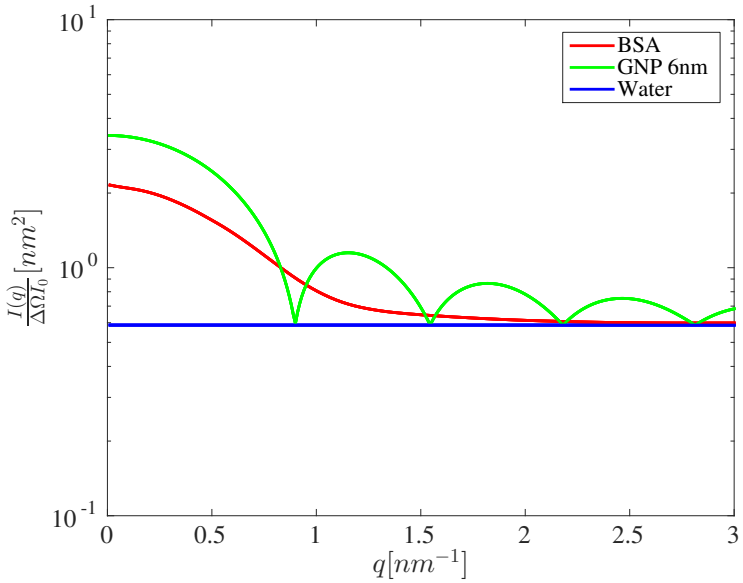


Figure 4.1: Theoretical cross-section models for GNP in water, BSA in water, and water used in simulations.

in Fig. 4.2(b)).

The geometry of the simulated SAXS-CT instrument is shown in Fig. 4.2(b). The x-ray source used was an infinitely small 8 keV monochromatic pencil beam with a beam size of 0.01 cm at the center of each sample. The distance of the front edge of the sample to the detector was fixed at 29 cm. $d$ is the distance between the center of the sample to the detector which varied little with the size of the three samples.

The detector is shown in Fig. 4.2(c). The maximum radius of the detector was 1.4 cm. There were 40 radial pixels with 100% detection efficiency. These instrument parameters achieve a scatter x-ray intensity profile with 40 points evenly in a $q$-range of 0.05 and 2 nm$^{-1}$ ($q$ is the momentum transfer defined as, $q = 4\pi sin(\theta)/\lambda$) which is the angular range where the largest cross-section difference is found between our gold nanoparticle (GNP) target and water background material.

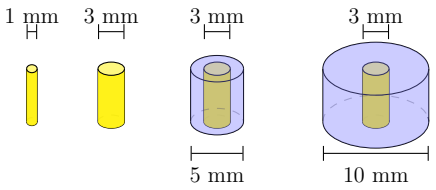


(a) The four sample geometries.

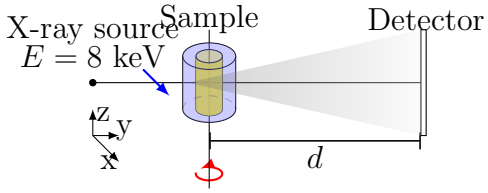


(b) SAXS-CT simulation geometry

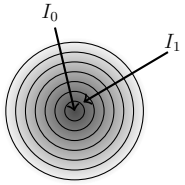


(c) Detector geometry

Figure 4.2: MC-GPU simulation geometries of (a) samples, (b) an idealized SAXS instrument, and (c) a radial detector. In (a), we simulated four sample objects. The inner yellow cylinder is the target material, and the blue outer cylinder is the background material. In (b), the blue arrow indicates a horizontal beam translation across the sample. The red arrow indicates a sample rotation to achieve multiple angular projections for CT reconstruction. In (c), the detector is radially shaped to count scattered x rays, $I$, at various angles equidistant to the center.

We simulated $5 \times 10^7$, $5 \times 10^7$, $2 \times 10^8$, $2 \times 10^9$ primary x rays per beam translation in the x-axis for the 1 mm, 3 mm, 5 mm, and 10 mm thick samples respectively. After translating the beam across the diameter of the sample +1 mm on each end, the sample was rotated 1° and the beam was translated across the x-axis again. This was repeated for 360 projections to achieve a full rotation about the sample. The simulation took 3 min for the smallest sample and 17 h for the largest sample using 5 NVIDIA GeForce GTX Titan GPUs in parallel.

The reconstruction of tomographic images from the 2D scatter profile was first presented in detail elsewhere [29,30]. The profiles provide measures of coherent scatter intensity $I$ arriving at a particular detector element (ring of pixels), integrated along the beam path. The measured pixel intensity (normalized to solid angle $\Delta\Omega$

subtended by the detector element and the transmitted intensity at $q = 0$ nm$^{-1}$, $I_0$) can be described as:

$$\frac{I(q)}{\Delta\Omega I_0} = \int_l n_0(l)\frac{d\Sigma(l,q)}{d\Omega}dl = \int_l S(l,q)dl, \tag{4.1}$$

where $n_0(l)$ is the volumetric electron density at $l$ position along the path through the object, $d\Sigma(l,q)/d\Omega$ is the differential coherent scatter cross section per scattering solid angle, and $q$ is the momentum transfer. The line integral of $S = n_0(l)d\Sigma(l,q)/d\Omega$, is formally equivalent to the line integral of the linear attenuation coefficient in conventional CT. Therefore, an image is reconstructed for each ring (scattering angle), resulting in a series of tomographic images corresponding to the scatter intensity at a series of scatter angles. The intensity at each detector angle was reconstructed to achieve a slice image using a filtered back projection (MATLAB `iradon` function).

## 4.3 Results

Fig. 4.3 shows SAXS-CT measurements of water solution with GNPs as the target material. The 1 mm and 3 mm diameter target material without background material are shown in the first two rows. The third row is the 3 mm diameter sample with a 5 mm diameter background of water. The fourth row is the 3 mm diameter target with a 10 mm diameter background. The smaller sample size required less number of translations. The first column is a slice image of the voxelized samples. Regions of air with low density in the image are depicted as black, the background

water material is gray, and the target GNP material is white. The second column is the attenuation CT image from the primary beam. Columns 3-42 are the scatter CT images at increasing angles. Fig. 4.4 shows SAXS-CT measurements in the same format as Fig. 4.3 but for a water solution with BSA. There is less contrast for BSA in the scattered images than for GNP because BSA has a smaller cross-section intensity than GNP.

Fig. 4.5 shows the reconstructed scatter profiles for all target materials in each sample geometry. The first column pixel maps in Figs. 4.3 and 4.4 were used to average intensities of all pixels belonging to the target material only at each angle. These averaged values were normalized by the area of the detector and the total number of x-ray trajectories simulated. The scatter profile can be seen in Fig. 4.5(left and middle). In addition, Fig. 4.5(right) shows the ratio of the calculated radius of gyration by Guinier analysis [35], $R_s/R_0$, of the reconstructed scatter profiles over the original cross section for both BSA and GNP. With larger samples, $R_s$, diverges from $R_0$ more so than for GNP.

## 4.4 Discussion

Our MC-GPU simulations confirm that SAXS-CT provides increased contrast compared to conventional CT not only for high-Z materials but also for proteins. This increased target contrast was qualitatively worse for BSA over GNP targets especially for larger sample sizes. However, our results suggest that significant contrast can be recovered for sample sizes of up to 10 mm.

Averaging pixels belonging to a particular target assisted with reconstructing an accurate scatter profile for the material. However, an alternative approach would be to repeat the simulation many times and average each pixel value rather than a region for applications where targets are small with respect to pixel size.

GNP scatter profiles were reconstructed accurately even for the largest sample with a $R_s/R_0$ larger than 0.95. For BSA, the scatter profile accuracy decreased at 5 mm and 10 mm sample sizes but were still above a $R_s/R_0$ of 0.89. This indicates that the coherent x-ray scatter could provide additional information to the primary attenuation images that are indicative of the molecular structure of the material.

We plan to extend the study to use different protein targets and more complex background materials while investigating optimal energies for monoenergetic and spectral x-ray sources. In particular, we are interested in studying the advantageous effect of using higher energy x rays with larger sample sizes on improving image quality and radiation dose minimization.

## 4.5 Conclusion

SAXS-CT is an emerging diagnostic medical tool that can potentially be used for in vivo x-ray molecular characterization of tissues. We have used MC-GPU simulations to study SAXS imaging for a gold nanoparticle (GNP) and serum albumen (BSA) protein target in a water background which serves as an initial investigation for performance at depths higher than those consistent with most optical techniques for molecular characterization.

A scatter profile of GNP target was resolved when the target was embedded at the center of a background material with 10 mm diameter and accurate information such as the radius of gyration could still be determined using the Guinier approxima-
860 tion. The system remains to be optimized to shorten measurements times, to allow for measurements of larger objects, and to minimize radiation dose. All of these concerns must be addressed before SAXS-CT can be translated to small-animal imaging and clinical use.

In summary, a publicly available MC-GPU code was used to simulate x-ray
865 trajectories in CT geometry and can be used to further study image quality and radiation dose delivered to the sample. We plan to quantify the scatter signal loss with increasing sample sizes with a variety of different protein targets and complex background materials while performing validation of our simulations with experimental measurements in physical phantoms.

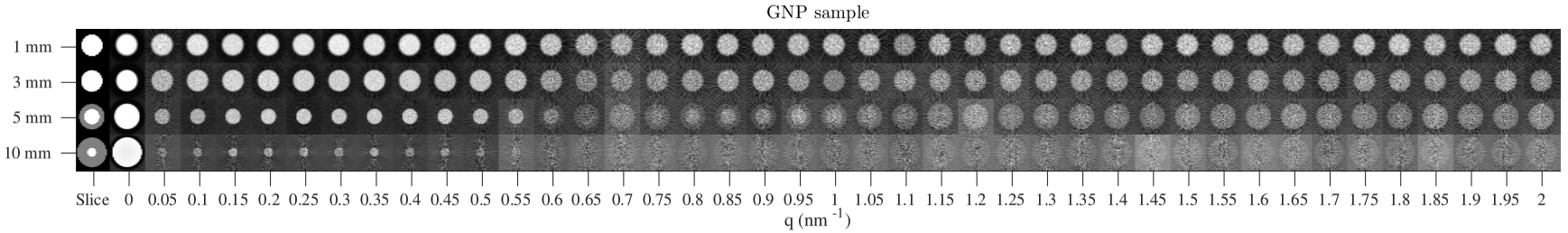


Figure 4.3: Slice images of samples with GNP in water as the target material. Each row shows a different sample geometry and is labelled with the maximum diameter of the outer sample cylinder. The first column shows a slice image of the voxelized sample geometry. White is the target material location, gray is the background water material location, and black is low density air material. The second column shows the conventional CT image using the primary beam at $q = 0$ nm$^{-1}$. Columns 3 to 42 show slice images reconstructed using detector counts at 40 increasing scattering angles between $q$ of 0.05 and 2 nm$^{-1}$.

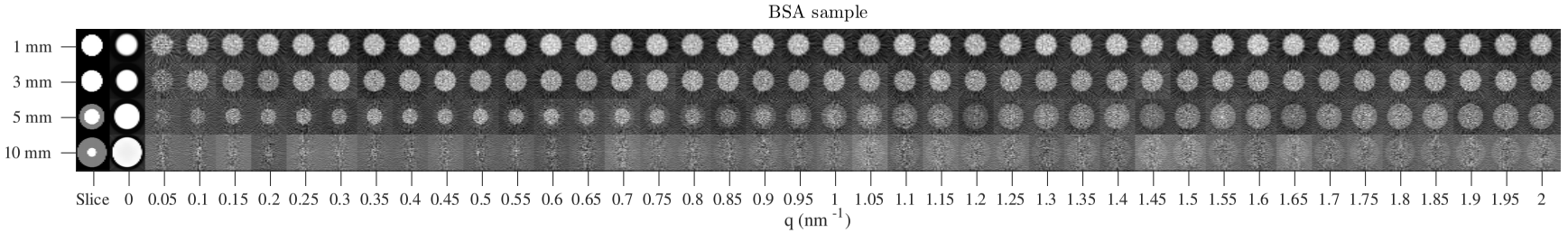


Figure 4.4: Slice images of samples with BSA in water as the target material. See Fig. 4.3 caption for description of format in data presentation.

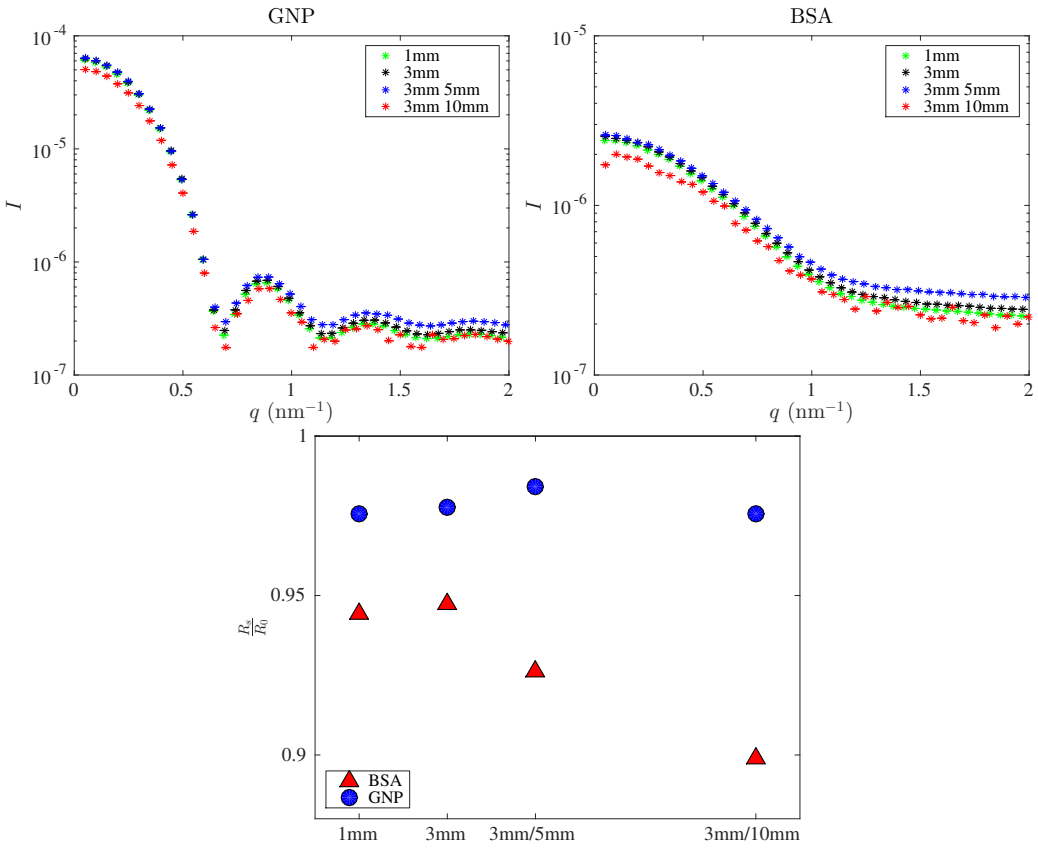


Figure 4.5: (Left) Reconstructed SAXS profiles of GNP by averaging all pixel values within the target of the sample for each angle. Intensities are normalized by the area of the detector and by the total number of x-rays simulated. (Middle) Reconstructed SAXS profiles of BSA by averaging all pixel values within the target of the sample for each angle. (Right) The ratio of the calculated radius of gyration for each of the reconstructed SAXS curves for both BSA and GNP, $R_s$, over the calculated radius of gyration of the original cross section used for simulations, $R_0$.

# Chapter 5: PSAXS phantom imaging studies

Coherent small-angle x-ray scattering (SAXS) provides molecular and nanometer-scale structural information. By capturing SAXS data at multiple locations across a sample, we obtained planar images and observed improved contrast given by the difference in the material scattering cross sections. We use phantoms made with 3D printing techniques, with tissue-mimicking plastic (PMMA), and with a highly-scattering reference material (AgBe), chosen because of their well characterized scattering cross section to demonstrate and characterize planar imaging of a laboratory SAXS system. We measure 1.07 and 2.14 $nm^{-1}$ angular intensity maps for AgBe, 9.5 $nm^{-1}$ for PMMA, and 12.3 $nm^{-1}$ for Veroclear. The planar SAXS images show material discrimination based on their cross section features. The image signal-to-noise ratio (SNR) of each $q$ image was dependent on exposure time and x-ray flux. We observed a lower SNR ($91 \pm 48$) at $q$ angles where no characteristic peaks for either material exist. To improve the visualization of the acquired data by utilizing all $q$-binned data, we describe a weighted-sum presentation method with *a priori* knowledge of relevant cross sections to improve SNR ($10{,}000 \pm 6400$) over the SNR from a single $q$-image at 1.07 $nm^{-1}$ ($1100 \pm 620$). In addition, we describe planar SAXS imaging of a mouse brain slice showing differentiation of tissue types

as compared to a conventional absorption-based x-ray imaging technique.

## 5.1 Introduction

When x ray quanta interact with matter they are transmitted, absorbed, or scattered. Several techniques make use of x-ray deflections at small angles to measure coherently scattered radiation that provides nanometer-scale structural information (0.1-100 nm) of the scattering material. These approaches are typically known as small-angle x-ray scattering (SAXS). Conventional x-ray medical imaging techniques have primarily focused on differentiating materials based on absorption properties providing micrometer scale morphology or spatial information. However, absorption-based approaches are limited in that many pathologies share similar attenuation characteristics with normal surrounding tissues, especially during early disease stages where change occurs at molecular and cellular levels. Many attempted to bridge the two approaches in order to obtain nanometer scale structural information coupled with micrometer scale spatial information with the ultimate goal of improving image quality and diagnostics. In a typical transmission SAXS design, an x-ray pencil beam traverses a sample and scattering patterns are recorded at small angles on a 1D or 2D detector. One approach to measure both scales simultaneously is by utilizing stepper motors to position a sample at various locations in the x-ray beam collecting SAXS data at each position. This information could be used differentiate materials by their inherent scattering cross section.

2D scanning SAXS has been explored clinically for various *ex vivo* biopsy

applications including bone, [63] breast, [27] brain, [70] and cardiac tissues. [13] Albeit a slower measurement compared to a single-shot, full-field, x-ray absorption image, the collection of scattering information provides unique information valuable for material classification. However, translating 2D scanning SAXS imaging into clinical practice requires the development of characterization and calibration tools to design and optimize these novel imaging modalities. A physical phantom with known material properties and geometry can greatly assist in the study of the system parameters affecting resolution, contrast, noise, and overall image quality.

We report planar SAXS (PSAXS) imaging using a laboratory system for a set of physical phantoms and for mouse brain tissue. We discuss factors affecting image quality in PSAXS imaging, describe a method for effective visualization, and compare material differentiation to x-ray absorption imaging.

## 5.2 Methods

Fig. 6.1 depicts the laboratory PSAXS system used for measurements. We use a laboratory SAXS system (SAXSpace, Anton Paar, Ashland, VA, USA). The instrument utilizes a sealed Cu-anode tube optimized for $K_\alpha$ radiation ($\lambda = 0.154$ nm). The system was configured in point collimation mode with an accessible $q$ range of 0.01–20 nm$^{-1}$ ($q = 4\pi sin\theta/\lambda$). A pinhole aperture was achieved using blocks to approximately 200×200 $\mu$m. We utilized 3 stepper motors with 10 $\mu$m step resolution within the instrument vacuum sample chamber to control horizontal and vertical sample motion with respect to a stationary x-ray beam with a sample-to-detector

distance (SDD) of 110 mm. The imaging detector is a CCD camera with a pixel pitch of 24 $\mu$m in an array of 2084×2084 pixels coupled with a $Gd_2O_2S$:Tb phosphor screen designed for 8-keV x rays.

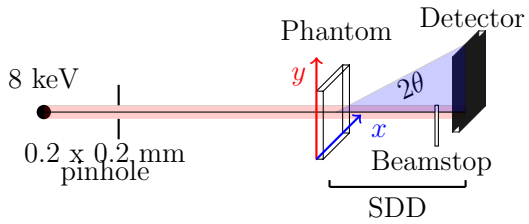


Figure 5.1: Schematic of the setup for planar SAXS imaging.]

Data was acquired and binned in the CCD in 8x8 pixels to allow for shorter measurement times and reduced memory storage. We noted that the highest angular resolution was not needed considering the characteristics of the scatter profiles of the materials used. A beamstop was positioned 5 cm in front of the detector to attenuate a portion of the primary beam of transmitted x rays preventing saturation of the detector pixels. All portions of the beam path were enclosed in a vacuum-sealed chamber at 350 mbar. The acquired 2D image of the scattering was corrected to account for the flat detector among other standard corrections using SAXStreat (Anton Paar, Ashland, VA, USA). Then, the data was radially averaged and reduced to 1D scatter profiles.

Due to the large number of subsequent measurements required per scan, it is impractical to measure a dark current prior to each measurement. A reasonable compromise is to record a dark current measurement with the same exposure time at the end of each set of scanning measurements. Dark current shift over the scan time was accounted for by selecting an angular position with no signal (0 $m^{-1}s^{-1}$)

and subtracting a uniform offset to bring that intensity to 0 $m^{-1}s^{-1}$.

Fig. 6.3 shows our dark current signal and the detector value at a q of 6 $nm^{-1}$ for each SAXS measurement in a typical set of scans.

A set of physical phantoms was designed in Inkscape using an encapsulated postscript format for the FDA logo and an Arial font for UMD lettering, exported in a drawing exchange format and then extruded using OpenSCAD to be 1 mm thick. The phantom designs were 3D-printed using a proprietary plastic (Veroclear$^{TM}$). As a comparison to a well-known plastic often used as tissue-mimicking material for x-ray absorption-based imaging modalities, we also cut the FDA logo into a slab of Polymethyl methacrylate (PMMA) using computer numerical controlled (CNC) milling. Fig. 5.5 (Top) shows the virtual designs and photographs of the 3D-printed Veroclear phantoms and the milled PMMA phantom. Because the 3D-printed material needed a thin base support in the letters, we use a well design with dimensions 3.00x1.50x0.11 cm for UMD and 4.0x2.5x0.11 cm for FDA. Well bottom thickness was 0.01 cm. The thickness standard deviation for the 3D-printed phantoms was ±0.02 mm as determined by a digital caliper. The FDA logo was cut into a 0.123 cm-thick slab of PMMA. The resulting PMMA phantom had dimensions 7.00x4.60x0.12 cm. The standard deviation in the thickness was 0.036 mm. The dimensions were designed to be small enough to fit in our sample holder and allow for the logo and lettering range to be covered by the range of motion by the stepper motors with a resolution relevant for tissue imaging (<1 mm). The phantom cut by the milling instrument was designed to be larger to ease the cutting process. We filled the wells in the Veroclear phantoms with silver behenate (AgBe) powder and

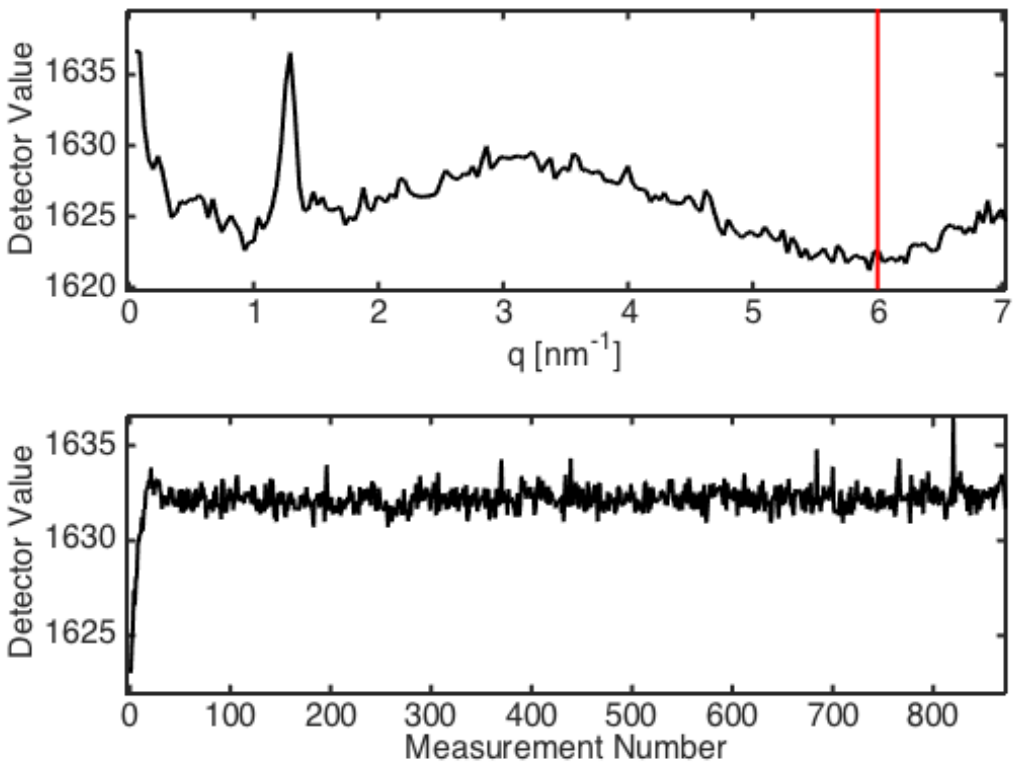


Figure 5.2: (Top) Dark current (DC) measurement. Red vertical line indicates q position at the lowest value. The peak at 1.1 nm$^{-1}$ is due to a row of bad pixels. (Bottom) Plot of detector values for all scatter measurements acquired at the angular position indicated by the red line. At the beginning of scanning measurements, the first few measurements increase the CCD values and stay relatively steady, or slowly decline. Only one DC measurement is needed and the DC shift can be corrected by subtracting a unique offset per each measurement. The noise is due to the measurement intensity variance. The occasional large peak is due to cosmic ray effect.

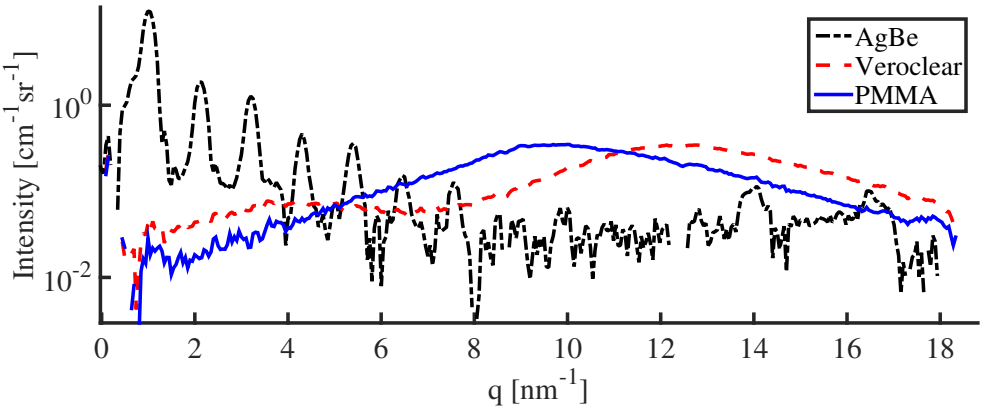


Figure 5.3: Absolute coherent scatter cross sections of AgBe, Veroclear, and PMMA.

used Scotch$^{TM}$tape to seal the open side. Holes were punctured into each independent segment of the wells to let air escape and prevent air pockets when the sample was under vacuum pressure. A similar procedure was performed for the PMMA phantom with both sides sealed with Scotch tape.

AgBe, Veroclear, and PMMA were selected for this work because they were independently measured to absolute scale using a glassy carbon intensity calibrant. [5] In addition, these materials have a well-characterized isotropic scattering cross section and remain unaltered for days inside the vacuum. Finally, the materials of choice demonstrate significant and reproducible material differentiation under SAXS imaging. Fig. 5.3 shows the absolute scatter profiles of the three materials used in this work. The minimum measured $q$ was 0.79 nm$^{-1}$.

We measured the UMD Veroclear phantom with 0.25 mm $x$ and $y$ steps with 5-s exposure at each location. In total, the scanned region covering the UMD lettering was 2.4x0.8 cm. The measurements took approximately 12 h. For these sets of measurements only, SDD was fixed at 302 mm which resulted in a measured $q$-range

of 0.19–6 $nm^{-1}$. All other measurements were obtained with a SDD of 110 mm providing a wider $q$-range of 0.79–19 $nm^{-1}$. Exposure time was increased to 10-s for better signal quality. The FDA Veroclear phantom was measured with 0.5 mm step sizes with a scanned region of 2.4×1.0cm. Total measurement time was approximately 3 h. The FDA PMMA phantom was measured with 0.5 mm step sizes and a scanned region of 2.5×1.1cm. Total measurement time was approximately 5 h. In addition, we measured the bottom corner of the D in this phantom with a higher step resolution of 0.25 mm. The scanned region was 0.7×0.5 cm and took approximately 2.4 h.

Data from PSAXS data can be visualized presenting the individual intensity map for all $q$ angles. However, to improve the visualization of material differentiation, we propose a method based on weighted averaging. We weight the intensity at each $q$ angle with the value of the corresponding cross section data of the material of interest ($I_M$) and then sum all $q$ images to obtain a combined single presentation image,

$$G = \sum_{q=q_1}^{q_n} g(q) I_M(q), \tag{5.1}$$

where $G$ is weighted-sum intensity map, and $g(q)$ is the intensity map at each $q$ bin.

We measured the signal-to-noise ratio (SNR) by selecting 3 regions-of-interest (ROI) for locations with AgBe and support material. The mean and variance were calculated for each ROI and SNR was estimated by SNR = $\mu_{AgBe}/\sigma^2_{support}$. The reported SNR is the mean and standard deviation of 3 estimates for each image.

To compare this imaging modality to x-ray absorption techniques utilized in

most conventional x-ray medical imaging applications, we imaged a few of the phantoms with a 30 kV spectrum running at 1.5 mA for a 2 s exposure. Fig. 5.5 (Bottom left) shows the PMMA FDA phantom with AgBe inside the logo, the Veroclear FDA phantom with no AgBe, and a PMMA UMD phantom with AgBe on tape removed from the UMD Veroclear phantom and attached to a uniform region of PMMA at top right which was imaged using x-ray absorption technique. The x-ray generator was UltraBright Microfocus source (Oxford Instruments, Abingdon, Oxfordshire, UK) with tungsten anode. The detector was FlashScan30, an amorphous silicon-based indirect detector (DPiX, Colorado Springs, CO, USA) with 2304×3200 pixels with a pitch of 125 $\mu$m and a thick CsI scintillator (650 $\mu$m). We collected and averaged five images of each phantom after dark-current and flat-field corrections.

In addition, we scanned a 1 mm coronal slice of a wild-type mouse brain with 0.25 mm step resolution placed in a tissue sample holder (Anton Paar, Ashland, VA, USA). The sample holder has x-ray transparent windows and allows the tissue to remain at atmospheric pressure while in the beam path. The mouse brain was prepared by fixing in paraformaldehyde, slicing using a vibratome to 1 mm, and was stored in a phosphate buffered solution at 4°C until measurements. No staining was performed to this tissue. 448 positions were measured with 100-s exposures for total of 15 h. An x-ray absorption image was also measured using the same system and settings used to measure absorption images for the phantoms.

## 5.3 Results

Results from PSAXS measurements are presented in Fig. 5.4. Intensity maps for the Veroclear UMD phantom are shown in the first column of images. This was the largest region measured at the highest spatial resolution. Measurements were performed in 4 separate sessions and dark current was corrected in each session independently. Horizontal streaks appear due to the inaccuracies If the dark current subtraction for each session. It was the only phantom measured with SDD of 302 mm. The SDD was reduced to 110 mm to acquire a wider angular range and observe intensity maps at PMMA and Veroclear's characteristic peaks at 9.5 and 12.3 $nm^{-1}$ and the exposure time per position was increased to 10 s per measurement for all other phantoms to increase signal quality. At $q$ locations where characteristic scattering peaks of AgBe is known to exist, 1.07 and 2.14 $nm^{-1}$, the AgBe material was the most intense signal in the image. For comparison, we also present an intensity map at a $q$-angle where no characteristic peaks exist for either support or AgBe material at 1.5 $nm^{-1}$. As expected, contrast between the two materials in each image are greatly reduced at this angle and would be further reduced with smaller $q$ resolution bins.

PMMA and Veroclear materials both have broad peaks in their scattering cross section, shown in Fig. 5.3, however PMMA has a scattering maxima at 9.5 $nm^{-1}$. At that angle, support material regions were the most intense for PMMA phantoms. Similarly, at 12.3 $nm^{-1}$ the Veroclear material was the most intense. Conversely, AgBe regions in the image at these $q$-angles are dark.

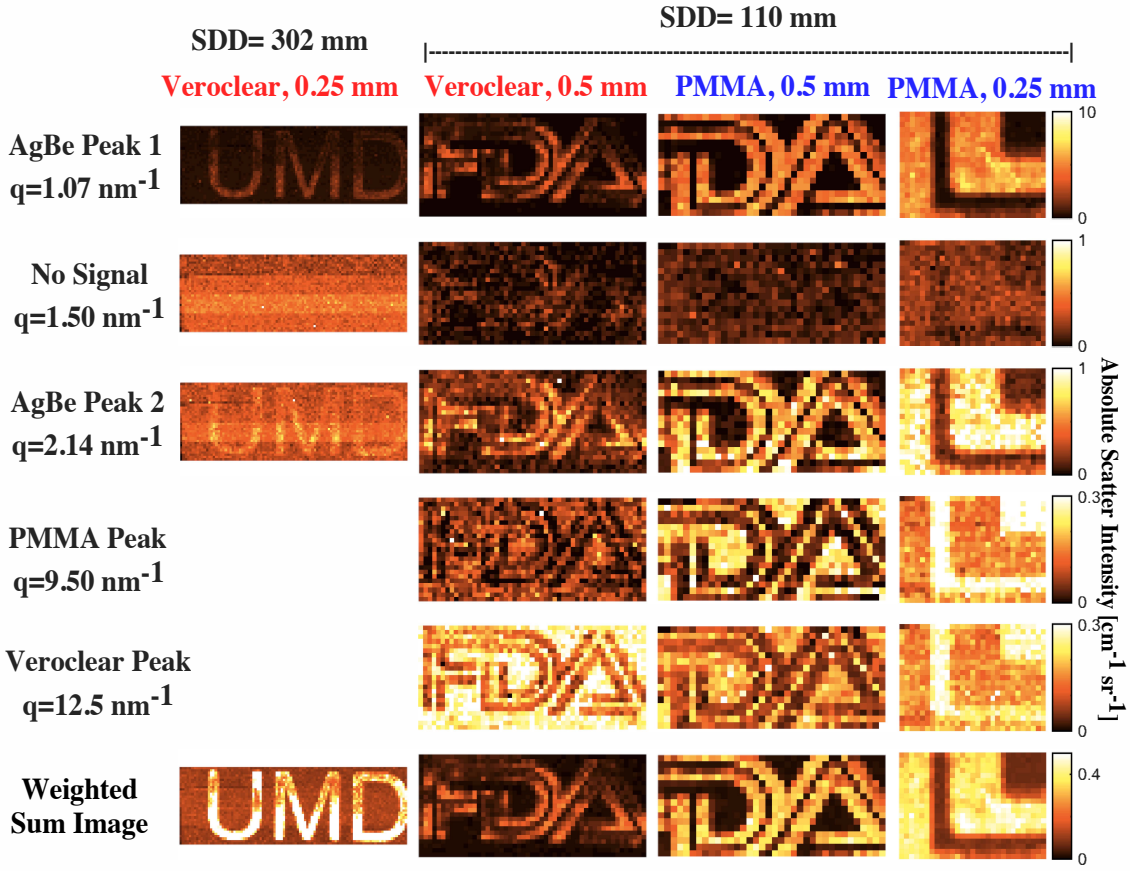


Figure 5.4: Four sets of planar SAXS measurements showing intensity maps at various $q$ angles of interest for the phantoms. Support material and spatial resolution are listed at the top.

The last row of images are the weighted-sum visualization as described in Eq. 5.1. With known cross sections of the target, data from each $q$-bin can be preferentially weighted and summed to increase the signal quality and material differentiation in a single presentation. In these images, we have weighted the $q$-images for AgBe. This presentation mode greatly improves the presentation of low signal measurements as in the Veroclear UMD phantom. The estimated SNR for images in the $4^{th}$ column of Fig. 5.4 which was 1100 ± 620, 91 ± 48, 522 ± 205, 100 ± 57, 140 ± 44, and 10000 ± 6400 from top to bottom.


Figure 5.5: (Top row) OpenSCAD visualization of the phantom geometries. The first two were designs for the 3D printer with support material. The last was used as a stencil for CNC milling. (Middle) Photograph of 3D-printed Veroclear phantoms attached to sample holder and of the CNC-milled PMMA. UMD was 3.00x1.50x0.11 cm and FDA was 4.0x2.5x0.11 cm in size. The lettering and logo regions dipped inward and had a thickness at the bottom of the well of 0.01 cm. (Bottom right) Photograph of CNC-milled PMMA with dimensions 7.00x4.60x0.12 cm. The FDA logo was cut all the way through.(Bottom) Photograph of the phantoms imaged in absorption mode and absorption x-ray images of phantoms.

As a comparison to PSAXS imaging, Fig. 5.5 (Bottom right) shows absorption images of the phantoms using a conventional transmission x-ray system. While this method can show contrast in plastic thickness well, this imaging is not as clear for material differentiation between AgBe and the PMMA in the phantom on the left. Moreover, material differentiation between Veroclear and PMMA is not possible. Differentiation could be confirmed with additional scattering data from PSAXS imaging. For areas with trace amounts of AgBe powder, as shown on the tape at the top right on the phantom to the right, the transmission x-ray system shows no signal.

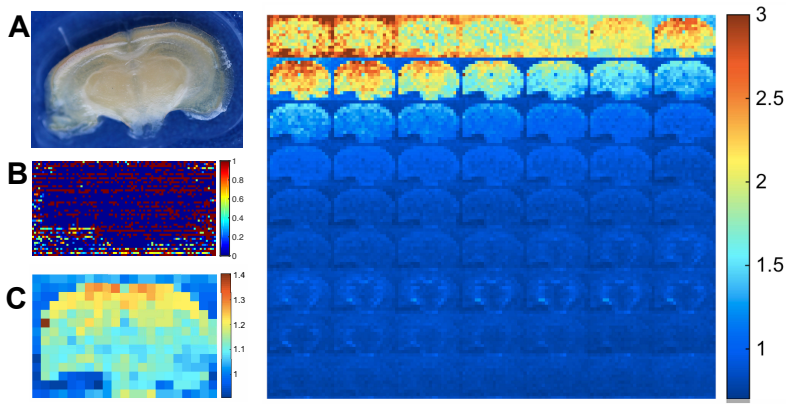


Figure 5.6: (Left) A. Photograph of coronal slice of wild-type mouse brain. B. Corresponding x-ray image after dark and flat field correction. C. Combined PSAXS image summing all $q$ angle images and dividing by number of $q$ bins. (Right) Montage of PSAXS images of coronal slice from a wild-type mouse brain for first 63 $q$ bins. Color bar represents absolute scattering intensity ($cm^{-1}sr^{-1}$).

Finally, we present an application of PSAXS imaging to biological samples. Fig. 5.6 shows tissue type differentiation for a 1 mm coronal slice of wild-type mouse brain. The montage shows scatter intensity maps of the first 63 $q$ bins. Each $q$ bin corresponds to 0.0179 $nm^{-1}$ and the $q$ range was 0.02 to 1.13 $nm^{-1}$. The first 4 images are from behind the beam stop in the beam path. Therefore, brain regions are less intense than regions with only sample holder windows. The $7^{th}$ row of images show the corpus callosum structure with a characteristic scattering peak at approximately 0.8 $nm^{-1}$.

## 5.4 Discussion

This work contributes to the study of factors affecting noise, artifacts, resolution, contrast and signal in a PSAXS imaging system. Using well-characterized materials at known locations in imaging phantoms, we can assess the influence of

these effects on image quality. Factors that affect image noise in this modality are associated with the detector used including its dark current stability and pixel non-uniformity. We observed a CCD temperature-dependent, temporal shift in dark current intensity and how this can affect images as seen in the Veroclear UMD phantom in Fig. 5.4. This could be improved by measuring a dark current between each measurement, however for practical reasons in shortening total measurement times, we measured only one dark current, and then performed a vertical offset for each frame using a reference region in the scatter profile that is expected to be 0 $m^{-1}$ $sr^{-1}$. In addition, we found cosmic rays appearing often in our measurements which manifest as sharp uncharacteristic peaks at random $q$ locations in the scatter profile. Understanding the material cross sections measured could help filter these spikes out of the data in post-processing steps along with the use of despiking corrections. [12] Shot noise is affected by the exposure time and x-ray flux. Shot noise becomes more apparent in $q$ images where not much scattering is measured due to material characteristics. We found important that shot noise does not affect a scatter image at a location where a characteristic peak is present. If shot noise is observed at these images, one approach is to increase exposure time. Higher brilliance systems such as those existing at synchrotron ($10^{11}$ - $10^{13}$ photons/second) can greatly reduce imaging times while maintaining good signal quality. In addition, 10 $\mu$m spatial resolution can currently be achieved at sychrotrons.

The non-uniform intensity in regions of the lettering and logo at AgBe peaks could be attributed to a combination of the effect of varying AgBe densities and of measurement fluctuations. The photographs in Fig. 5.5 were taken after mea-

surements. Visible differences in density of AgBe can be correlated to the PSAXS images.

We have demonstrated PSAXS imaging in a laboratory commercial SAXS system with a beam size of 200 $\mu$m and step sizes down to 250 $\mu$m. This laboratory set-up could be useful in applications where the spatial resolution is utilized for coarse registration of positions within a tissue sample, and the SAXS data at each position provide structural changes happening at the molecular level.

In PSAXS imaging, spatial resolution is dictated by the step size of the object holder, the beam size, and the beam divergence. Angular $q$ resolution is affected by the beam size and beam divergence as well as by the detector pixel size and pixel binning.

## 5.5 Conclusion

This work demonstrates the capabilities of utilizing coherent scatter information at small angles for medical imaging applications where precise material differentiation of nanometer scale structures is needed. A phantom was constructed to show logo and text patterns and imaged with a motorized sample holder for scanning. The scatter cross section is an inherent characteristic of the material nanostructure and can provide unique biomarkers for early detection of diseases. [16] Coherent scatter image at small angles shows promise for imaging applications where contrast agents or nonspecific molecular tags are undesirable.

# Chapter 6: PSAXS of mouse brains

In this chapter, we report results from planar SAXS imaging on sliced wild-type mouse brains with characterization of gray and white matter and corpus callosum cross section profiles. We describe methodology for measurement and data analysis confirming characteristic peaks at 0.81 and 1.6 $nm^{-1}$ for white matter and corpus callosum respectively. Accelerated Monte Carlo imaging simulations for a SAXS-CT configuration are then performed with a simplified cylindrical model of the wild-type mouse brain to demonstrate the capabilities of SAXS imaging. We simulated the model with and without a skull material and found an average improvement in SNR of 0.13 for all materials when a skull was not present. In addition, the dose deposited on the brain was calculated to be 2.4 Gy in the simulation performed with the skull, and 2.2 Gy without the skull. Although the simulation without the skull had lower overall estimated dose deposited, there was an increase of dose deposited on the brain by 0.2 Gy. Our findings can be used to assess optimal instrument parameters and for designing dedicated small-animal SAXS imaging prototypes.

## 6.1 Introduction

Small-angle x-ray scattering (SAXS) techniques measure coherently scattered x-ray deflections at small angles analyzed to produce nanometer-scale structural information (0.1-100 nm) about the scattering sample. Recently, efforts have been focused on utilizing SAXS for medical imaging to provide better material characterization and for diagnostic applications. Since x rays carry higher energies than visible light, SAXS imaging has potential to non-invasively image deeper tissues beyond 1 mm.

Conventional x-ray medical imaging techniques have primarily focused on differentiating materials based on absorption properties providing micrometer scale morphology. However, absorption-based imaging approaches are limited in that many pathologies share similar attenuation characteristics with normal surrounding anatomy, especially during early disease stages where change occurs at the molecular and cellular levels. There is increasing interest in measuring and utilizing scattered x rays, traditionally considered noise in absorption-based approaches, for nanometer-scale structural information coupled with micrometer scale spatial information with the ultimate goal of improving image quality and diagnostic performance.

In transmission SAXS, an x-ray pencil beam traverses a sample and scattering patterns are recorded at small angles on a 1D or 2D detector. As shown in Fig. 6.1(*left*) Planar SAXS (PSAXS) might use stepper motors to position and collect SAXS data at various locations in the plane orthogonal to the beam direction. This information could be used to map and differentiate materials by their inherent

scattering cross section. Several research groups have investigated this approach for studying nanostructure characterization of bone, [32, 63] and recently of cardiac tissue. [13] However SAXS signal quality and resolution are affected by sample thickness and therefore applications of PSAXS have been limited to *ex vivo* biopsy studies. To contribute to the improvement of these new modality, we have recently reported on imaging phantoms for the assessment of PSAXS image quality. [17]

A different approach is depicted in Fig. 6.1(*right*). Here, a SAXS computed tomography (SAXS-CT) design uses image reconstruction algorithms to obtain SAXS profiles of locations deep within objects enabling applications in *in vivo* molecular x-ray imaging. This technique has been used to study biological tissues and plastics, [39] polyethelene, [75] collagen-based phantoms, [91] lamb tissue, [52] and rat brain tissue. [46, 47] We have recently explored a method to assess SAXS data quality for SAXS-CT using Monte Carlo imaging simulations. [18]

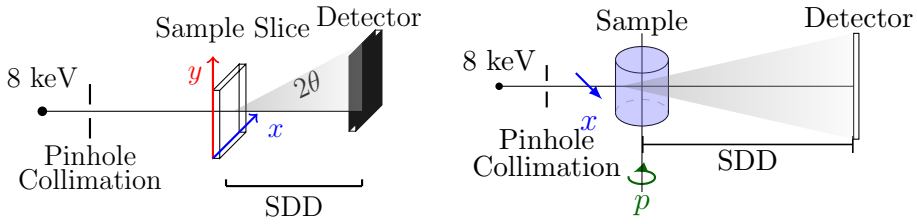


Figure 6.1: Schematic of the imaging setup for planar SAXS (left) and SAXS-CT (right).

One major area of interest in clinical applications of SAXS imaging is the study and diagnosis of neurological disorders. There are currently no known cures or effective treatment for many neurological disorders. Recent discoveries indicate that biomolecular changes may appear 20 or more years before dementia symp-

toms appear. In this context, SAXS imaging may be able to detect earlier disease changes and used to study therapy effectiveness. [16,84] The most notable potential biomarker is myelin, a highly structured fibrous tissue that has been investigated using SAXS for multiple sclerosis. [23,46,85] In addition, amyloid fibers [25,53] have been investigated for imaging Alzheimer's disease along with SAXS signals of brain tumours. [81]

Other brain imaging methods include optical techniques that can successfully characterize molecular neurological hallmarks but lack the ability to image deep tissue where the hallmarks tend to form during early stages of disease. On the other hand, PET imaging has become the standard of practice for *in vivo* imaging using amyloid-targeting tracers. However, PET suffers from inherently low spatial resolution and low specificity. [80] MRI techniques, on the other hand, have high spatial resolution (up to microscale resolution). MRI is currently utilized to study myelin density and location, [55, 83] but is not yet able to characterize nanoscale structural information.

The brain has been studied in X-ray diffraction, SAXS, or WAXS studies over the past 30 years. We provide here a summary of the work related to measured scattering cross sections of brain tissue and report cross section peaks from these studies in Table 6.1. Alzheimer's disease studies using x-ray diffraction were first attempted by Chia *et al.* [15] in 1984. They studied diffraction peaks of myelin isolated from the white matter from human brain of 3 Alzheimer's disease patients and 3 age-matched normal control patients. The study used a laboratory CuK$\alpha$ point source collecting scatter on film for 4 h. They found broad peaks at 0.415, 0.46, and

1 $nm^{-1}$ for normal brain sections, and only the 0.46, and 1 $nm^{-1}$ for Alzheimer's disease brain sections. In 2000, Lazarev *et al.* [54] studied x-ray diffraction patters from fresh 1x5x8 mm samples of human brain white matter among other tissues with no chemical alterations or preservation. They used an 8 keV monochromatic laboratory source with a 8x0.4 mm focal spot and an incident energy per measurement of $2x10^8$ photons in 10-mm beam length with an accessible q-range of 0.044–5.2 $nm^{-1}$. They found diffraction peaks for normal brain, Alzheimer's brain, and cerebral hemorrhage at 0.3189, 0.8055, 1.28, and 1.65 $nm^{-1}$, with the strongest peak at 0.8055 $nm^{-1}$.

More recently, Avila *et al.* [7] studied x-ray diffraction patterns of transgenic mouse optic and sciatic nerve surgically removed and isolated intact. They stretched the nerve bundle within a quartz capillary and measured diffraction patterns with a Cu K$\alpha$ radiation. X-ray diffraction patterns were recorded for an hour using a linear, position-sensitive detector. The focal spot was 0.8 $mm^2$. They compared results of fixed, unfixed, and plastic embedded nerves on myelin periodicity. They found aldehyde treatment introduced a 7% increase in myelin periodicity and a 5% decrease in relative intensity as compared to unfixed nerves. The plastic embedded nerves suppressed myelin peaks to <1% of relative myelin amount over myelin and the background compared to 25% and 30% for unfixed and fixed myelin respectively. The theoretical periodicity of myelin was 17.4 nm which is associated with peaks every 0.36 $nm^{-1}$. However in their measurements, they found myelin periodicity varied depending on preservation technique between 18.7–20.1 nm ± 4 nm (using largest error bar values), which is associated with peaks periodically occurring between

0.313–0.336 $nm^{-1}$. The relative amount of myelin over myelin and the background varied ± 10%. They also studied a isotonic and hypotonic buffer and how swelling of the myelin affects periodicity measurements, provided a comparison for the sciatic and optic nerve, and compared periodicity measurements for optic and sciatic nerves from various transgenic mice. In 2008, De Felici *et al.* [23] studied the structure of human cerebral myelin sheaths using a synchrotron source of intact white and gray matter. The authors reported on the packing order of myelin and attributed distances to SAXS profiles. To avoid measurements of structural changes due to the preservative, they took special care to measure samples within a few days of extraction from cadavers. They used 1 mm thick and 10 mm diameter brain samples immersed in formaldehyde and a 12.4 keV with 50x50 $\mu m^2$ focal spot. The CCD detector covered a range of 0.036 to 0.49 and 4.7 to 48 $nm^{-1}$ using two different sample-to-detector distances. They randomly probed 20 locations in the sample in the white or gray matter. All data showed isotropic rings. In the SAXS data, they found characteristic peaks of white matter at 0.5, 0.75, 1.0, 1.1, 1.5, and 1.8 $nm^{-1}$. The gray matter had similar peaks, but to a much lower intensity. The white matter WAXS data showed 3 broad peaks at 14.4, 20.1, and 29.0 $nm^{-1}$. The gray matter WAXS data had peaks at 20.1 and 29 $nm^{-1}$ but none at 14.4 $nm^{-1}$. They also found that human myelin sheath has a periodicity of 16.5 nm with a slight difference between male and female samples.

The first SAXS-CT study of an intact whole rat brain was performed by Jensen *et al.* [46] using a high-brilliance synchrotron source ($10^{11}$ photons/s) at 18.58 keV and with a focal spot size of 25 $\mu m^2$ using a photon counting PILATUS 2M detector.

They reported measurements for a total of 541 projections over 360° each for 721 translation steps of 25 $\mu$m with 150 ms for scatter measurements and 10 ms for absorption measurements. One tomographic slice was obtained after an exposure time of 24 h. They studied myelin sheaths of mouse brains and reported periodic myelin sheath peaks at approximately 0.35, 0.7, 1.05, 1.35 $nm^{-1}$. They also reported cytoskeletal neurofilaments at 0.6 and 1.05 $nm^{-1}$. They found the second neurofilament peak to overlap with myelin's third peak. The corpus callosum had higher intensity of myelin peaks because these structure consists of densely packed neurons connecting the left and right hemisphere. These authors reported that myelin is the most highly scattering isotropic signal from the brain in the measured range.

In this paper, we report and analyze SAXS cross sections of various brain tissues. Our findings will stimulate the understanding of variability for various brain structures to be used in exploratory simulations to assess feasibility of *in vivo* methods and in the design of optimized dedicated systems for small-animal imaging.

## 6.2 Methods

### 6.2.1 SAXS measurements

We use a laboratory SAXS system (SAXSpace, Anton Paar, Ashland, VA, USA) for PSAXS measurements (Fig. 6.1,*left*). The instrument utilizes a sealed Cu-anode tube optimized for $K_\alpha$ radiation ($\lambda = 0.154$ nm). The system was configured in point collimation mode with an accessible $q$ range of 0.01–20 $nm^{-1}$ ($q = 4\pi sin(\theta)/\lambda$). A pinhole aperture was achieved using blocks to approximately 200x200 $\mu$m. We

Measured SAXS Peak Locations from Literature

| | $q$ **(nm$^{-1}$)** | $d = 2\pi/q$ **(nm)** | **Location** | **Classifier** |
|---|---|---|---|---|
| Chia [15] | 0.415 | 15.14 | Myelin (WM) | Human Brain: AD |
| | 0.460 | 13.65 | Myelin (WM) | Human Brain: AD, Normal |
| | 1.00 | 6.28 | Myelin (WM) | Human Brain: AD, Normal |
| Lazarev [54] | 0.32 | 19.7 | WM | Human Brain: AD, Normal |
| | 0.81 | 7.80 | WM | Human Brain: AD, Normal |
| | 1.28 | 4.90 | WM | Human Brain: AD |
| | 1.65 | 3.81 | WM | Human Brain: AD, Normal |
| Avila [7] | 0.32 | 17.4±1.2 | Myelin | Mouse nerve: fresh |
| | 0.41 | 15.3±1.0 | Myelin | Mouse optic nerve: fresh |
| | 0.34 | 18.7 | Myelin | Mouse nerve: fixed |
| | 0.40 | 15.7 | Myelin | Mouse optic nerve: fixed |
| De Felici [23] | 0.375 | 16.75 | WM | Human brain |
| | 0.760 | 8.267 | WM/GM | Human brain |
| | 1.030 | 6.100 | WM | Human brain |
| | 1.140 | 5.511 | WM | Human brain |
| | 1.153 | 4.120 | WM/GM | Human brain |
| | 1.900 | 3.307 | WM | Human brain |
| | 14.40 | 0.436 | WM | Human brain |
| | 20.10 | 0.313 | WM/GM | Human brain |
| | 29.00 | 0.217 | WM/GM | Human brain |
| Jensen [46] | 0.37 | 16.75 | Myelin | Rat brain |
| | 0.6 | 4.120 | Neurofilament | Rat brain |
| | 0.75 | 8.267 | Myelin | Rat brain |
| | 1.1 | 6.100 | Myelin, Neurofilament | Rat brain |
| | 1.4 | 5.511 | Myelin | Rat brain |

Table 6.1: Compilation of characteristic peaks of the nervous system from various sources. *AD*: Alzheimer's disease, *WM*: White matter, *GM*: Gray matter. Values were estimated from figures in the articles and error of measurements are shown when reported from sources.

| Mouse | Slice | Δx,Δy (mm) | Exposure time (s) | Binning | $q$-range ($nm^{-1}$) |
|---|---|---|---|---|---|
| 1 | 1 | 0.50 | 60 | 4x4 | 0.14–18.4 |
| | 2 | 0.25 | 100 | 4x4 | 0.16–7.03 |
| | 3 | 0.25 | 300 | 8x8 | 0.53–18.3 |
| 2 | 1 | 0.25 | 300 | 4x4 | 0.13–7.09 |

Table 6.2: Experimental settings of all slices measured.

utilized 3 stepper motors with 10 $\mu$m step resolution within the instrument vacuum sample chamber to control horizontal and vertical sample motion with respect to a stationary x-ray beam. The imaging detector is a CCD camera with a pixel pitch of 24 $\mu$m in an array of 2084×2084 pixels coupled with a $Gd_2O_2S$:Tb phosphor screen designed for 8-keV x rays.

We scanned four approximately 1 mm thick, coronal slices of a wild-type mouse brain placed in a tissue sample holder (Anton Paar, Ashland, VA, USA). The sample holder has x-ray transparent windows and allows the tissue to remain at atmospheric pressure while in the beam path. The mice brains were prepared by fixing in paraformaldehyde, slicing using a vibratome to 1 mm, and was stored in a phosphate buffered solution at 4°C until measurements. No staining was performed to this tissue. Table 6.2 lists the spatial steps sizes, exposure time, binning of the CCD pixels, and the $q$ range measured by adjustment of the sample-to-detector distances for each brain slice measured. The anatomy of brain slices were estimated by associating structures in the photograph images to an available Allen Developing Mouse Brain Atlas. [56]

Because registration of a particular brain tissue type is difficult once inside the SAXS system, it was necessary to image the brain slice in a 2D scanning SAXS, so

we could register a particular cross-section measurement to a location in the brain. Photographs were taken of the brain slice before measurements. The tissue dehydrated over a few hours outside a buffer solution. We found that after a slice of brain dries, it could be re-hydrated by storing in phosphate buffered solution for a few hours. However to prevent temporal effects from the drying process affecting measurements, we waited until the tissue was fully dehydrated before starting measurements.

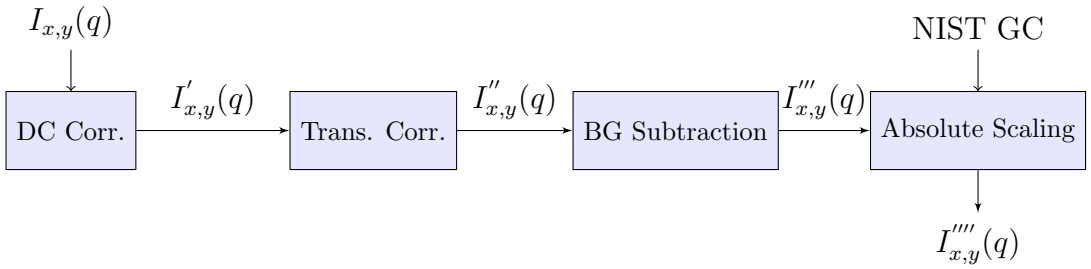


Figure 6.2: Block diagram of PSAXS data processing. The main four blocks are Dark Current Correction, Transmission Correction, Background Subtraction, and Absolute Sntensity Scaling.

A beamstop was positioned 5 cm in front of the detector to attenuate a portion of the primary beam of transmitted x rays preventing saturation of the detector pixels. All portions of the beam path were enclosed in a vacuum-sealed chamber at below 34 mbar. The acquired 2D image of the scattering was corrected to account for standard geometric corrections due to instrument geometry and the CCD using SAXStreat (Anton Paar, Ashland, VA, USA). Then, the data was radially averaged and reduced to 1D scatter profiles, $I(q)$. We performed four additional important corrections for our data at each coordinate pixel position $(x, y)$ as shown in Fig. 6.2. The following describes each processing step.

### 6.2.2 Data Analysis

For each set of measurements, a dark current measurement was acquired for the same exposure as each position. Ideally, a dark current measurement would be obtained immediately after each measurement to have the most accurate dark current correction due to temporal effects. However, due to the large number of subsequent measurements required per scan, it is impractical to measure a dark current between each measurement. Because the shape of the dark current 1D curve does not change other than a temperature and time-dependent offset, a reasonable compromise is to record a dark current measurement with the same exposure time at the end of each set of scanning measurements. Dark current shift over the scan time was accounted for by selecting an angular position with no signal (0 $m^{-1}$ $s^{-1}$) and subtracting a time-dependent offset to bring that intensity to 0 $m^{-1}$ $s^{-1}$. Fig. 6.3 shows our dark current signal and the detector value at a $q$ of 6 $nm^{-1}$ for each SAXS measurement in a typical set of scans. The following equation shows the subtraction of the dark current signal and an offset,

$$I^{'}_{x,y} = I_{x,y}(q) - D_c(q) - \text{offset}_{x,y}. \tag{6.1}$$

Each position had the same exposure time, but there were slight variations in thickness in the slice especially after drying. We corrected for thickness differences

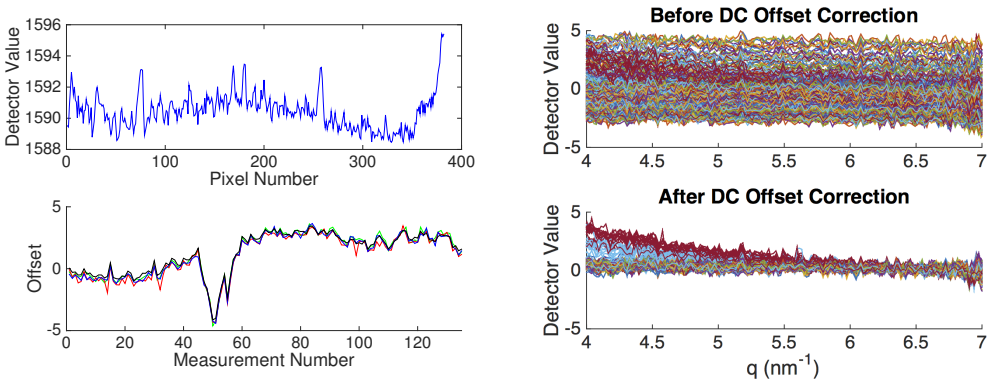


Figure 6.3: (Top left) Dark current (DC) measurement. (Bottom left) Plot of detector values after dark current subraction at a few angular positions for all scatter measurements. The black line is an average of 30 angular positions. (Top right) All measurements plotted by $q$ after dark current subtraction, but before dark current offset correction. (Bottom right) All measurements plotted by $q$ after dark current subtraction, and after dark current offset correction.

in the tissue by dividing scatter profiles by the transmission value for each pixel,

$$I''_{x,y}(q) = \frac{I'_{x,y}(q)}{I'_{x,y}(0)}. \tag{6.2}$$

However, we make the assumption is that the tissue at each location has approximately the same attenuation properties.

When scatter profiles at each location are corrected for dark current and transmission differences, the background can be subtracted. We define the background as the windows of the tissue sample holder that contribute to the scatter signal measured. In the planar scan, we ensured that there are locations measured that only contain the windows and no tissue. We averaged the scatter profile of all pixels that only contained window, $I_{BG}$, and subtracted this background signal from all

positions,

$$I'''_{x,y}(q) = I''_{x,y}(q) - I''_{BG}(q). \tag{6.3}$$

To convert empirical measurements to absolute cross sections, measurements of a secondary intensity standard, 1 mm thick glassy carbon, [94] and $q$ calibration reference [14], silver behenate (AgBe), were also acquired in the same scan. The glassy carbon measurements were scaled to NIST data of absolute glassy carbon values and a calibration factor, $C_f$ was obtained. The calibration factor was multiplied by all other measurements,

$$I''''_{x,y}(q) = C_f I'''_{x,y}(q). \tag{6.4}$$

The $q$-angles in measurements were corrected by the AgBe measurements where peak locations are known.

### 6.2.3 SAXS-CT simulations

To study SAXS-CT feasibility for brain imaging applications, simulations of x-ray transport of the entire SAXS imaging chain were performed using Monte Carlo techniques. We used MC-GPU, a GPU-accelerated x-ray transport simulation tool that has previously been used to generate clinically-realistic radiographic projection images and computed tomography (CT) scans of the human anatomy. [9] The code is publicly available and distributed for free in source form. MC-GPU massively multi-threads a Monte Carlo simulation algorithm for the transport of x rays in a voxelized

geometry utilizing x-ray interaction models and cross sections from PENELOPE 2006. [73] MC-GPU has handled realistic human anatomy phantoms, like the freely available Virtual Family model, [20] and adapted to simulate coherent scattering CT incorporating molecular form factor and structure factor effects. [18,19,28] The x-ray source is an infinitely small monochromatic pinhole beam which can be set to a single monochromatic energy or spectra. The detector pixels 100% detection efficiency and can be set to any size with any resolution. The input text file specifies instrument geometry including detector size, source-to-detector distance, sample-to-detector distance, monochromatic energy of the source and other important parameters for the simulation such as the number of x-ray tracks to simulate, number of GPUs to use in multithreading process. The voxelized sample geometry is defined in a text file which specifies number of voxels, material assignment, and density of material ($g/cm^3$).

The molecular form factors can be obtained by measuring the scattering profile. The process is demonstrated in detail elsewhere [8, 50, 87], here we will give a brief description. The measured scatter profile provide relative values of $(1+cos^2(\theta/2)) \times F^2_{Mol}(q)$ that are not readily usable in the simulation code. It is known for theoretical considerations [8, 38] that at sufficiently large momentum transfer $q$ the measured $F_{Mol}$ asymptotically approaches the Independent Atomic Approximation (IAA) form factors given by,

$$F^2_{\mathrm{IAA}} = \sum n_i F^2(q, Z_i), \tag{6.5}$$

where $n_i$ is the weight fraction of element $i$, $Z$ is the atomic number, $F(q, Z)$ is

the coherent scatter form factor for element $i$ [42]. As a result, the absolute values of $F^2_{\mathrm{Mol}}(x)$ could be estimated by re-normalizing the data to fit the IAA values in an interval of $q$ ranging from 40 to 50 nm$^{-1}$. In this study, we used our measured 1D scatter profiles $I(q)$ of white matter (WM1), gray matter (GM1) and skull form factors estimation. We used the measured scatter profiles given by De Felici *et al.* [23] for WM2 and GM2 for comparison.

For WM1 and GM1 we used the same form factors of WM2 and GM2 respectively at wide angular range from 2.5–50 nm$^{-1}$. For the skull we normalized our measured $F_{mol}$ (given in relative values) to those given by Tartari *et al.* [87] for bone in an interval of $q$ ranging from 2.5 to 5 nm$^{-1}$. A comparison of the form factors obtained by IAA model and measured data are shown in fig.6.4 Fig. 6.4(a) shows the geometry of the cylindrical model of the mouse head. The skull thickness was 0.2 mm, gray matter was 1 mm, and white matter was 8 mm in diameter. The density use for gray and white matter materials was 1.03 g/cm$^3$ and the skull was 1.85 g/cm$^3$. We simulated 100 translation points at 0.1 mm step sizes across this 1x1 cm$^2$ region, 360 projections with 1° angular steps. The x-ray energy was 20 keV monochromatic with a beam divergences 0.08°. The sample-to-detector distance was 30 cm. The detector was 3 cm in radius and had 300 bins from the center to edge with a $q$ range of 0–10 nm$^{-1}$. For each translation and projection, we simulated $1\times10^9$ histories totalling $3.6\times10^{13}$ histories for the CT slice image. This took approximately 13 hours on a computer with 6 GeForce GTX Titan GPUs. To study the effect of the skull on signal quality and dose deposited to the brain, we repeated simulations replacing the skull material with WM1.

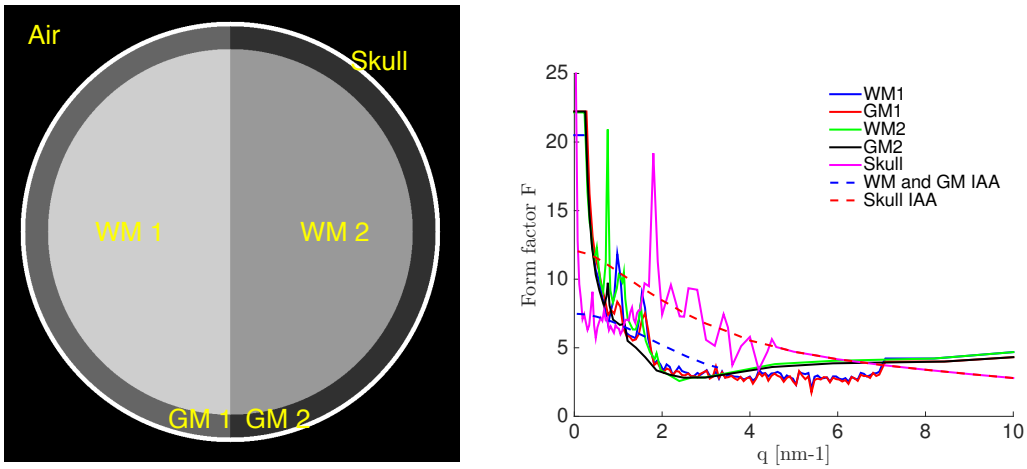


(a) Virtual phantom of mouse brain

(b) Form factor of materials.

Figure 6.4: (a) Simplified cylindrical model of a slice of a mouse head. (b) Coherent scattering form factor for WM1, WM2, GM1, GM2 and skull materials. dotted line: form factors calculated with IAA. Solid line: form factors measured in this study.

We calculated the signal-to-noise ratio (SNR) by taking the mean over the standard deviation of pixel values belonging to each material,

$$\text{SNR} = \mu_{mat}/\sigma_{mat}. \tag{6.6}$$

This calculation could be achieved for each $q$ intensity map, however, for the comparison of simulations with a skull in place versus skull replaced by gray matter, we selected a $q$ angle with a prominent peak for both WM1 and WM2 at 1.03 nm$^{-1}$.

## 6.3 Results

Fig. 6.5 shows results from the first coronal slice in the frontal lobe of a wild-type mouse brain. A photograph of the frontal section of the brain shows the left and right hemisphere of the cortex in the upper two quadrants and the olfactory bulbs

in the bottom two quadrants. Before measurement, the brain had dried in the tissue sample holder and in the process of drying, the two hemispheres had separated. We present a $q$ intensity map at 0.19 $nm^{-1}$ where regions could be by intensity in the pixels. The scatter profiles for each region were averaged. In this measurement, since we measured with a SAXS and WAXS range, we stitched the scatter profiles using the regions of overlap. There are two visible broad peaks at approximately 1 and 1.6 $nm^{-1}$ for region 1 that exists to a lesser degree for region 2. There is also a very broad and low intensity peak at approximately 13.8 $nm^{-1}$ which exists for both regions. This particular slice had both gray and white matter superimposed in the beampath, therefore there are influences of scattering from both tissue types in the scatter profile. For this reason, the two peaks at small-angles may be suppressed.

For the next set of measurements, we increased the exposure time to 100 s for higher quality signal and observed only the SAXS range. Fig. 6.6 shows results from a second slice from the wild-type mouse brain which has distinct gray matter at the perimeter of the cortex, and a corpus callosum which can be seen as the lighter white strand connecting the left and right hemispheres. At a particular $q$ of 0.81 $nm^{-1}$, the intensity map shows a distinct structure of corpus callosum which is more intense with respect to the other parts of the brain. Two regions were : A structure that is likely to be the corpus callosum, and the remaining region of the brain. The average scatter profile of pixels in the region shows there is a distinct peak at 0.81 and 1.62 $nm^{-1}$ that is more intense in the corpus callosum region of the slice.

To improve the signal quality of measurements further, we measured the next

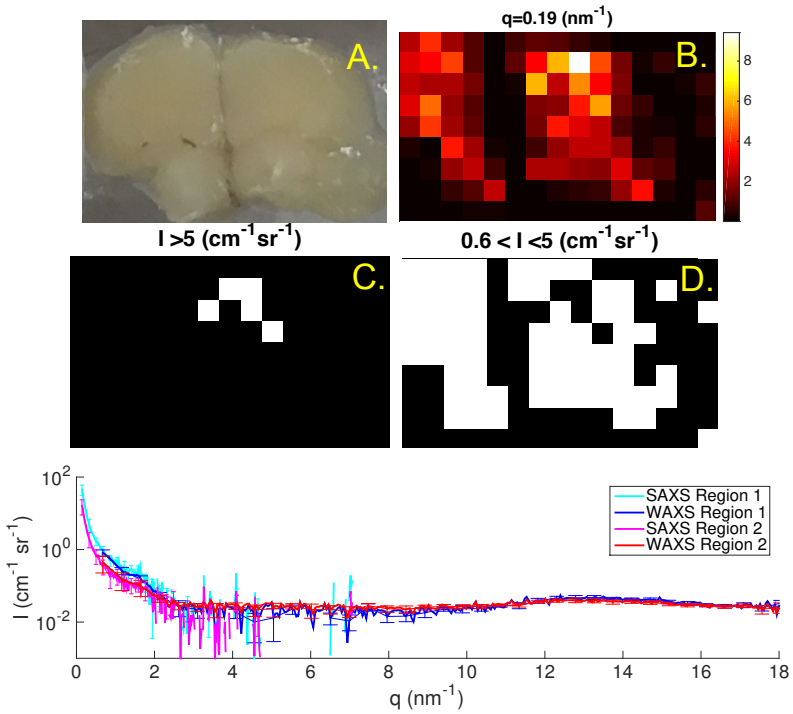


Figure 6.5: (A.) Photograph of first coronal slice into the frontal lobe of the wild-type mouse brain. The upper half is the cortex, whereas the bottom half are the olfactory bulbs. (B.) An intensity map at $q$=0.19 nm$^{-1}$. (C.) First region where intensity was higher than 5 cm$^{-1}$ sr$^{-1}$ in B. (D.) Second region where the intensity was between 0.6 and 5 cm$^{-1}$ sr$^{-1}$ in B. (Bottom) Stitched data of the average frontal lobe using measurements in SAXS and WAXS range. The scatter profiles are a result of the average of pixels in the two regions depicted in C and D. Error bars are $\pm 1\sigma$ for every 10 points.

set with an exposure time of 300 s per position and observed the WAXS range. Fig. 6.7 shows results from a third slice from the mouse. During the drying process, the brain slice had curled at the edges. We observed the intensity map at a strong peak of $q$=1.6 nm$^{-1}$ and three regions by intensity. The average scatter profiles of pixels in the regions shows there is a distinct peak at 0.92 and 1.6 nm$^{-1}$ to varying intensities. The $q$ resolution for these measurements were also lower due to binning by 8x8 instead of 4x4 in other measurements. The higher binning allowed for higher signal at wider angles where broad peaks occur and where high angular resolution

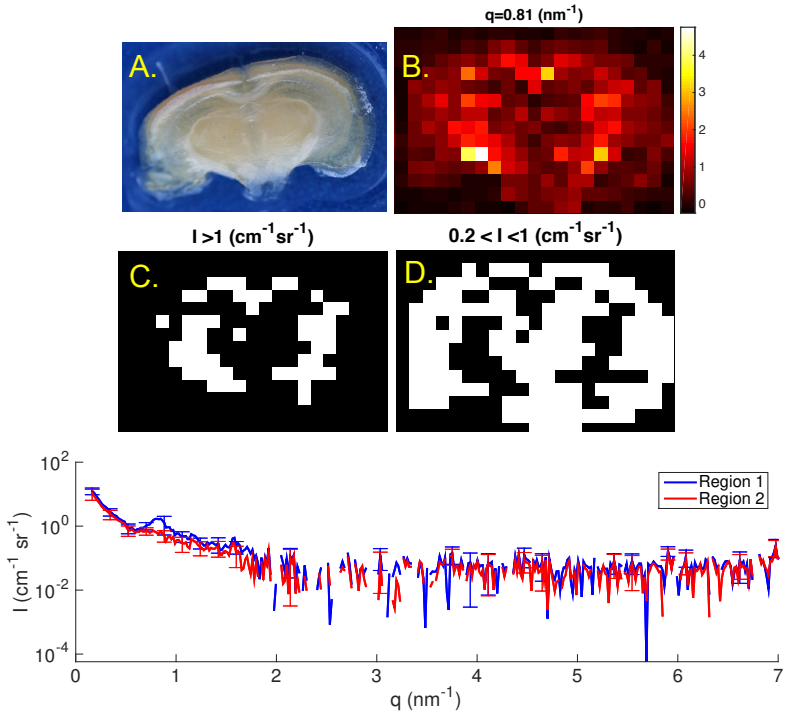


Figure 6.6: (A.) Photograph of a coronal slice in a wild-type mouse brain. (B.) An intensity map at $q$=0.81 nm$^{-1}$. (C.) First region where intensity was higher than 1 cm$^{-1}$ sr$^{-1}$ in B. (D.) Second region where the intensity was between 0.2 and 1 cm$^{-1}$ sr$^{-1}$ in B. (Bottom) Scatter profiles of the average of pixels in the two regions depicted in C and D. Error bars are $\pm 1\sigma$ for every 10 points.

is not needed. There is a broad peak at 7.14 and another at 14.6 nm$^{-1}$.

Finally, we present measurements of a slice from a second wild-type mouse brain with an exposure time of 300 s per position and observed the SAXS range in Fig. 6.8. The first peak existed for all positions at $q$=1.01 nm$^{-1}$, so we three regions by the intensity map at that angle. The average scatter profiles of pixels in the regions shows there are two distinct peaks at 1.01 and 1.53 nm$^{-1}$ also to varying intensities. All observed peaks, both distinct and subtle, in scatter profiles measured were tabulated in Table 6.3.

Fig. 6.9 shows SAXS-CT simulations of a simplified mouse head constructed

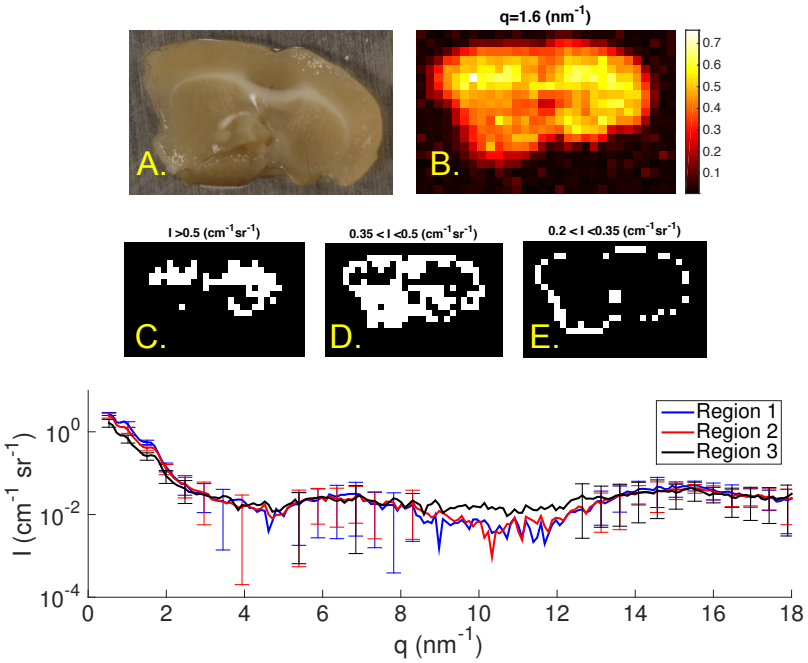


Figure 6.7: (A.) Photograph of a coronal slice in a wild-type mouse brain. (B.) An intensity map at $q$=01.6 nm$^{-1}$. (C.) First region where intensity was higher than 0.5 cm$^{-1}$ sr$^{-1}$ in B. (D.) Second region where the intensity was between 0.35 and 0.5 cm$^{-1}$ sr$^{-1}$ in B. (E.) Third region where the intensity was between 0.2 and 0.35 cm$^{-1}$ sr$^{-1}$ in B.(Bottom) Scatter profiles of the average of pixels in the three regions depicted in C,D and E. Error bars are $\pm 1\sigma$ for every 10 points.

of cylinders. The outer layer is bone with a thickness of 0.2 mm. The next layer is gray matter with a thickness of 1 mm. The inner layer is white matter with a thickness of 8 mm. Also in Fig. 6.9, we show material cross sections obtained from literature, whereas the right side uses material cross sections we measured. The CT images show at particular angles, the white matter material has more contrast with respect to other materials. By averaging the pixels belonging to each material type, we can reconstruct the scattering x-ray cross section of the materials. Because the skull is expected to be highly attenuating, we also simulated the same virtual phantom but with the skull voxels replaced with GM2 which is shown in the middle figure. All SAXS-CT images show presence of the skull. The simulation with the

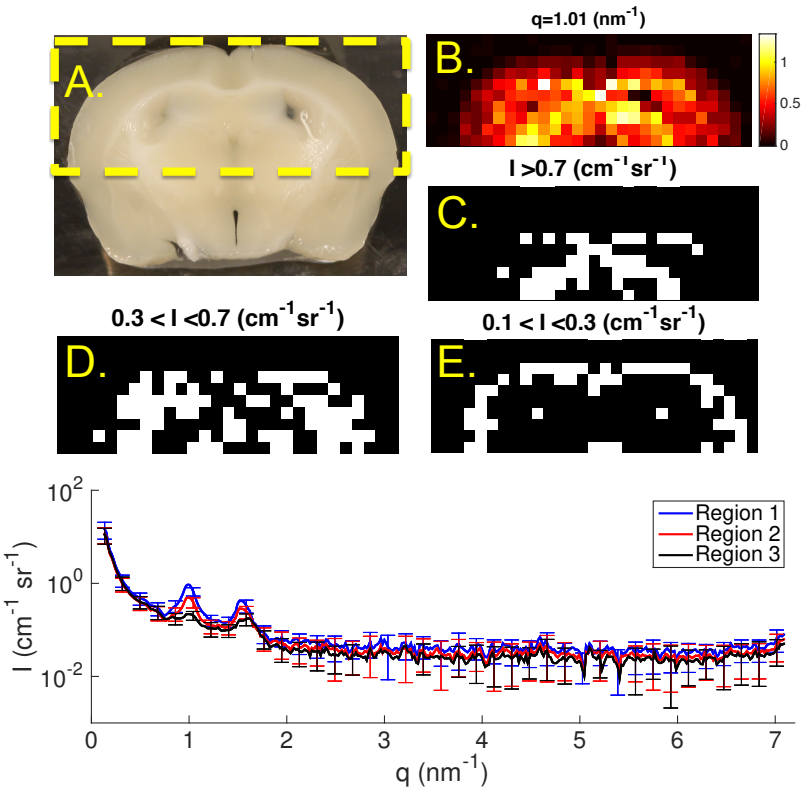


Figure 6.8: (A.) Photograph of a coronal slice in a second wild-type mouse brain. Dotted yellow line indicates region that was imaged. (B.) An intensity map at $q$=1.01 nm$^{-1}$ where the first peak appeared in the scatter profiles. (C.) First region where intensity was higher than 0.7 cm$^{-1}$ sr$^{-1}$ in B. (D.) Second region where the intensity was between 0.3 and 0.7 cm$^{-1}$ sr$^{-1}$ in B. (E.) Third region where the intensity was between 0.1 and 0.3 cm$^{-1}$ sr$^{-1}$ in B.(Bottom) Scatter profiles of the average of pixels in the three regions depicted in C,D and E. Error bars are $\pm 1\sigma$ for every 10 points.

skull calculated an estimated total dose of 2.4 Gy whereas the simulation without the skull was 2.2 Gy deposited on the entire region imaged. In the simulation with the skull, the white and gray matter had each approximately 50 Gy whereas the skull had 323 Gy, given density of the skull was 1.85 g/cm$^2$ and at the perimeter of the phantom whereas the brain density was 1.03 g/cm$^2$ and at the center. In the simulation without the skull, all materials were approximately between 50–57 Gy with a slight increase in dose deposited compared to simulations with the skull.

| | Fig. 6.5 | | Fig. 6.6 | | | | | |
|---|---|---|---|---|---|---|---|---|
| $q$ **(nm$^{-1}$)** | 1.60 | 14.1 | 0.39 | 0.56 | 0.81 | 1.01 | 1.58 | 1.92 |
| $d$ **(nm)** | 3.93 | 0.45 | 16.1 | 13.7 | 7.76 | 6.22 | 3.98 | 3.27 |

| | Fig. 6.7 | | | | | | | Fig. 6.8 | | | | |
|---|---|---|---|---|---|---|---|---|---|---|---|---|
| $q$ **(nm$^{-1}$)** | 0.96 | 1.65 | 2.48 | 3.01 | 3.89 | 6.75 | 15.4 | 0.55 | 0.66 | 0.82 | 1.01 | 1.53 |
| $d$ **(nm)** | 6.55 | 3.81 | 2.53 | 1.62 | 1.61 | 0.93 | 0.41 | 11.4 | 9.52 | 7.66 | 6.22 | 4.11 |

Table 6.3: Compilation of characteristic peaks measured.

The calculated SNR for each material is tabulated below in Table. 6.4.

| | **WM1** | **WM2** | **GM1** | **GM2** |
|---|---|---|---|---|
| **with skull** | 24.0 | 20.93 | 10.8 | 6.30 |
| **without skull** | 24.9 | 21.3 | 10.0 | 6.20 |

Table 6.4: SNR of each material for simulations with or without a skull present.

## 6.4 Discussion

We measured approximately 1 mm thick slices of wild-type mouse brain with an aim of characterizing the small-angle scattering cross section for various tissue types and compare to results from others. A planar SAXS set-up allowed us to register different parts of the brain to SAXS intensity maps. Our planar SAXS measurements of three slices of normal wild-type mouse brain show regions in the slice of the brain with common characteristic cross section features, in particular, with the corpus callosum.

Some sources of error in our measurements are due to imperfect dark current subtraction since only one is obtained at the end. We mitigated some of the error by offsetting by a constant that is determined by averaging several points near the tail-end of the scatter profile that is supposed to be approximately 0 cm$^{-1}$ sr$^{-1}$.

This reduced the standard deviation across all measurements at a few angles with approximately 0 $cm^{-1}$ $sr^{-1}$ in the scatter profile from 1.4201 to 0.1987 $cm^{-1}$ $sr^{-1}$ as shown in Fig. 6.3 (right).

We scaled the intensity of the measurements to absolute scale using a secondary glassy carbon standard, however, some error in absolute intensities are introduced with imperfect background subtraction. In a conventional SAXS measurement of bio-molecules in solution, it is advised to use the same quartz capillary sample holder for the signal measurement as well as the background measurement so the sample holder can be subtracted more accurately. In a planar SAXS imaging, it would be more robust to measure the same tissue sample holder without the tissue as a location-dependent background measurement, however this would double the measurement time. As another compromise for our background subtraction, we regions of windows of the tissue sample holder which served as the background signal using intensity thresholds, averaged the scatter profile and used this as a surrogate background for background subtraction. Negative intensities do not theoretically exist in absolute x-ray scattering cross sections, however, they appear in our data in Fig. 6.5 and are an inevitable result of imperfect subtraction of noisy data.

Despite these errors, we were able to detect prominent peaks that exist in white matter and more so in the corpus callosum structure which we suspect could be due to the higher density of nerve fibers and myelin sheaths surrounding the nerve axons. Myelin has been reported to be a strong small-angle scatterer and the subject of many neurological SAXS studies Our prominent peak was at 0.81 $nm^{-1}$ which match with results from Lazarev *et al.*, and are similar to 0.76 $nm^{-1}$ from

De Felici *et al.*, and 0.75 $nm^{-1}$ from Jensen *et al.* (refer to Table 6.1). The differences can be explained by the $q$ resolution and uncertainty of our system, [65] but also to differences in myelin and neuron structure in different species of animals as previous reports were on the human and rat brain. Finally, the drying of the brain before measurements may shrink the periodic packaging of the myelin layers thereby overestimating the peak location.

Other peaks reported be others were not detected in our measurements. This is probably because of a combination of low scatter signal intensities, peak broadening due to our $q$ resolution. Finer quality measurements can almost always be performed at a synchrotron source where pencil beam sizes can go down to 10 $\mu m^2$, there is flexibility in energy of x-rays, and flux of the beam is between $10^{11}$ to $10^{13}$ photons/s. However, we have demonstrated detection of the strongest myelin peak within the corpus callosum structure with a laboratory source.

The SAXS-CT simulations showed that the approximate dose to an animal for a single CT slice imaged was approximately 2.4 Gy. Improvements can be made by using a higher energy at the sacrifice of the signal quality. At the settings we used, we were successfully able to reconstruct the original cross sections of each pixel location in the CT slice.

## 6.5 Conclusion

We have measured small-angle x-ray scattering (SAXS) of wild-type mouse brain slices in a planar imaging mode to characterize cross sections of various tissue

types within the brain. Our work compares results from wild-type mouse brain to previous SAXS measurements of brains from other species and aims to generalize commonalities in cross section peaks attributed to myelin, which is the strongest scatterer within the brain. We demonstrate SAXS-CT with simulations using a Monte Carlo X-ray transport simulator (MC-GPU) of a simplified mouse head model and report estimated SNR and radiation dose deposited to a brain for a CT slice.

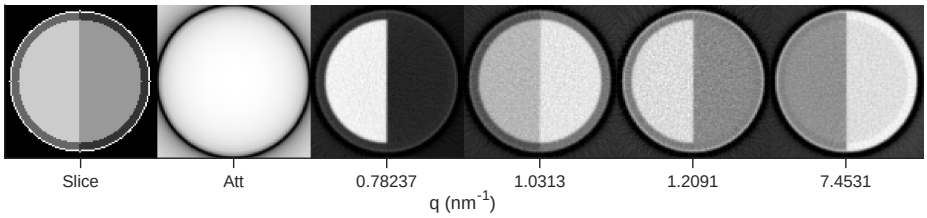


(a) SAXS-CT results of phantom with skull.

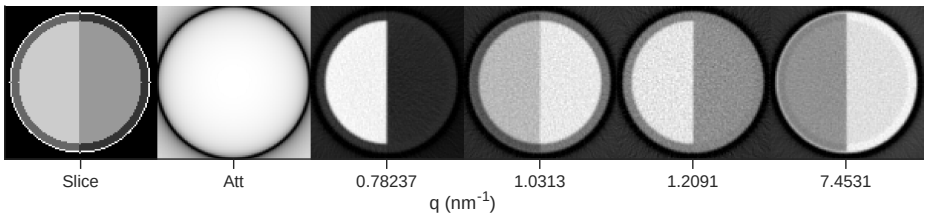


(b) SAXS-CT results of phantom without skull.

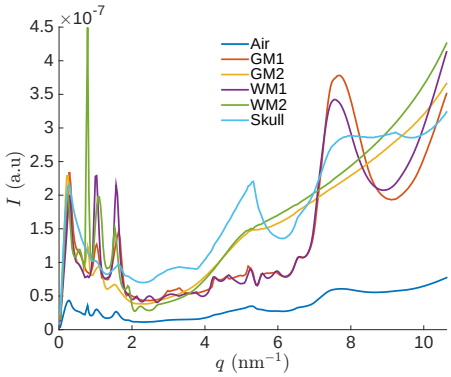


(c)

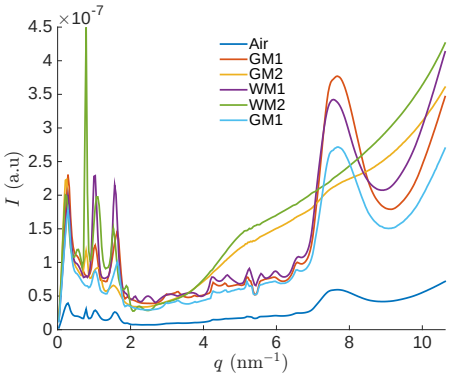


(d)

Figure 6.9: (a) Results from SAXS-CT simulations using MC-GPU. First image is a map of materials (same as Fig. 6.4(a)). The second image is the attenuation image that a typical CT image would produce. The 3rd to 6th images are intensity maps reconstructed from a specific $q$ angle indicated below the image. (b) Results of SAXS-CT simulations with the skull replaced by GM2. (c-d) Using the material map in the first image, we averaged pixels belonging to a particular material and plot cross sections of each material(c: with skull, d: without skull).

# Chapter 7: SAXS imaging of amyloids

## 7.1 Introduction

Alzheimer's disease (AD) remains the only disease in the top ten leading causes of death in America that cannot be prevented, slowed, or reversed. [3] AD is the most common degenerative brain disorder that destroys memory, thinking skills, and ability for people to perform every day tasks. Precise biomolecular changes that lead to AD, why disease progression varies greatly among people, disease prevention, and effective treatments are still unknown. [45, 71, 89]

One widely-accepted hypothesis posits that $\beta$ amyloid deposition in the brain parenchyma is a molecular culprit for AD onset and has been the target of AD imaging and disease-modifying therapeutic research. [76] Some imaging methods to assess molecular changes in the brain include optical techniques that can successfully characterize neurological hallmarks but lack the ability to image deep tissue ($>$ 1 mm) where they tend to form during early stages of disease. On the other hand, PET imaging has become the gold standard for *in vivo* imaging of amyloid in the brain using amyloid-targeting tracers. However, PET suffers inherently from low spatial resolution and low specificity. [80] MRI techniques, on the other hand, have high spatial resolution (up to microscale resolution). MRI is currently utilized

to study myelin density and location, but are not yet able to achieve nanoscale structural information. We propose that small-angle x-ray scattering (SAXS) imaging may have the potential to detect $\beta$ amyloid plaque earlier by their molecular structure characteristics without tracers and assist in the need for better diagnostics and therapy monitoring tools. [16]

SAXS is a biophysical method to study shape and structure of macromolecules in solution. In transmission SAXS, a monoenergetic x-ray pencil beam traverses a sample and scattering patterns are recorded at small angles on a 1D or 2D detector. Information on size, shape, and structure can be extracted from the recorded scatter profiles through various analytical techniques. This technique has been used extensively to study in vitro structure of $\beta$ amyloid monomers, oligomers, and fibrils in solution. [44, 51, 77]

SAXS has recently been extended to imaging applications is solids and soft matter. Planar SAXS (PSAXS) uses stepper motors to position and collect SAXS data at various locations in the sample in the plane orthogonal to the beam direction. This information could be used to map and differentiate materials by their inherent scattering cross section. Several research groups have investigated this approach for studying nanostructure characterization of biological materials. [13, 32, 63]

We histologically assess amyloid in an AD model mouse brain, measure and compare PSAXS imaging of a coronal slice from transgenic AD model mouse brains to a wild-type mouse brain, measure and report PSAXS measurements of a wild-type mouse brain with a bovine serum albumin (BSA) amyloid fibril model placed at a specific location and locate it using planar SAXS imaging, and simulate anthropo-

morphic virtual phantoms of a mouse and human head with embedded neurological plaque targets.

## 7.2 Methods

For PSAXS imaging measurements, a laboratory SAXS system (SAXSpace, Anton Paar, Ashland, VA, USA) with a sealed Cu-anode tube optimized for $K_\alpha$ radiation ($\lambda = 0.154$ nm) was utilized. We configured the system in point collimation mode with an accessible $q$ range of 0.01–20 $nm^{-1}$ ($q = 4\pi sin(\theta)/\lambda$). The pinhole aperture was approximately 200x200 $\mu$m. The system has 3 stepper motors with 10 $\mu$m step resolution to control sample position with respect to the beam within air-tight vacuumed sample chamber. Scattered x-rays were captured by a CCD camera with a pixel pitch of 24 $\mu$m in an array of 2084×2084 pixels binned 4x4 coupled with a $Gd_2O_2S$:Tb phosphor screen designed for 8-keV x rays.

We obtained 2 wild-type (WT) 9 month old mouse brains along with 2 transgenic (Tg) AD model mouse brains that were 8 month old and 4 month old. The mouse brains were prepared by fixing in paraformaldehyde, slicing coronally using a vibratome to 1 mm, and was stored in a phosphate buffered solution at 4°C until measurements with no staining performed. To confirm locations of amyloid deposits in the AD mouse model, we took subsequent slices of the 1 mm thick slices at 40 $\mu$m for histological confirmation using a amyloid-targeting dye, Thioflavin S. The 40 $\mu$m slices were stained following procedures outlined by Rajamohamedsait et al. [69] For PSAXS measurements, we placed the 1 mm brain slices in a tissue sample holder

(Anton Paar, Ashland, VA, USA). The sample holder utilizes x-ray transparent windows and enables the tissue to remain at atmospheric pressure while in the vacuumed beam path. The SAXS signals of the slice was measured at 0.25 mm steps horizontally and vertically to cover the entire region of the brain slice. Exposure time was 300 s per position. The sample-to-detector distance was 30.5 cm to cover a $q$ range of 0.16 to 7 $nm^{-1}$. 957 positions were measured and took 60.5 hours for each slice.

We also measured a bovine serum albumin (BSA) amyloid fibril model placed at a specific location in a wild-type mouse brain slice and locate it using planar SAXS imaging. BSA fibrils mimic nanostructural qualities of amyloid fibrils by their beta-sheet formation of threads. [22] BSA amyloid fibrils were concocted with heating and cooling cycles of BSA in solution following work presented in Dahal *et al.* [22] The first fibrils are formed within two weeks of initial preparation, however do not continue growing after two months at room-temperature controlled incubation. We waited two months for stability and saw visible white threads of BSA fibrils in the solution. To condense the fibrils, we centrifuged the fibrils at 12,500 rpm for 30 minutes. A BSA fibril pellet was formed of diameter 0.8 mm. At measurement time, the prepared BSA pellet was placed in the right side of the mouse brain slice shown in Fig. 7.8. The photograph was taken after measurements where the tissue was dehydrated. We found the tissue could be re-hydrated by storing in phosphate buffered solution for a few hours. However we intentionally allowed the tissue to dry before measurements to prevent temporal effects from the drying process affecting measurements.

To study SAXS-CT feasibility for *in vivo* brain imaging applications in mouse and human, simulations of x-ray transport of the entire SAXS imaging chain were performed using Monte Carlo techniques. We used MC-GPU, a GPU-accelerated x-ray transport simulation tool that has previously been used to generate clinically-realistic radiographic projection images and computed tomography (CT) scans of the human anatomy. [9] The code is publicly available and distributed for free in source form. MC-GPU massively multi-threads a Monte Carlo simulation algorithm for the transport of x rays in a voxelized geometry utilizing x-ray interaction models and cross sections from PENELOPE 2006 [73] and was adapted to simulate coherent scattering CT incorporating molecular form factor and structure factor effects. [18, 19, 28] The x-ray source is an infinitely small monochromatic pinhole beam which can be set to a single monochromatic energy or spectra. The detector pixels 100% detection efficiency and can be set to any size with any resolution. The voxelized sample geometry is defined in a text file which specifies number of voxels, material assignment, and density of material ($g/cm^3$). We obtained voxelized virtual phantom of a mouse from Digimouse, [86] with segmented regions using PET, CT, and crysosection data. Digimouse has a 0.1 $mm^3$ voxel size and approximate size of the head was 1.5 x 1.5 cm coronally. A voxelied human head phantom was obtained from Iacono et al. [43] which segmented material regions by MRI data. This phantom is called Multimodal Imaging-Based Detailed Anatomical Model (MIDA) and has 0.05 $mm^3$ voxel sizes. The approximate size of the MIDA phantom was 16 x 20 cm transversly. For simulations in this work, we obtained a coronal slice in the Digimouse head region and a transverse slice in the MIDA phantom.

| # | Material | Density (g/cm$^3$) | |
|---|---|---|---|
| 0 | Air | 0.001 | MIF |
| 1 | Skin | 1.10 | IAA |
| 2 | Skeleton | 1.85 | MIF |
| 7 | Gray Matter | 1.03 | MIF |
| 8 | Striatum | 1.03 | MIF |
| 10 | White Matter | 1.03 | MIF |
| 11 | Muscle | 1.04 | IAA |

Table 7.1: Digimouse material index, materials, and density information in a single coronal slice. MIF is material interference function which indicates we supplied empirical scatter profiles at small angles. IAA is the independent atomic approximation, where theoretical scatter off of independent atoms are used in simulations without consideration of interference effects.

| # | Material | Density (g/cm$^3$) | |
|---|---|---|---|
| 1 | Air | 0.001 | MIF |
| 2 | Gray Matter | 1.03 | MIF |
| 3 | White Matter | 1.03 | MIF |
| 4 | Muscle | 1.04 | IAA |
| 5 | Adipose | 0.92 | IAA |
| 6 | Cortical Bone | 1.85 | MIF |
| 7 | Spongiosa Bone | 1.85 | MIF |
| 8 | Cartilage | 1.85 | MIF |
| 9 | Skin | 1.10 | IAA |
| 10 | Cerebrospinal Fluid | 1.00 | MIF |
| 11 | Blood | 1.00 | MIF |

Table 7.2: MIDA material index, materials, and density information in a single transverse slice. MIF is material interference function which indicates we supplied empirical scatter profiles at small angles. IAA is the independent atomic approximation, where theoretical scatter off of independent atoms are used in simulations without consideration of interference effects.

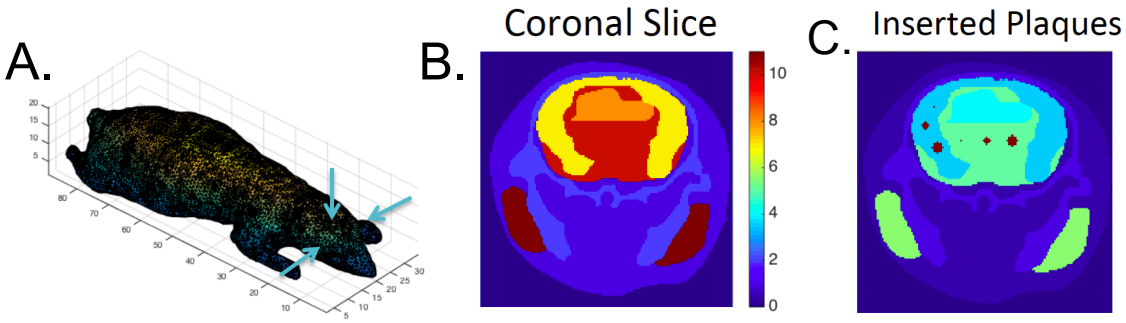


Figure 7.1: (A.) Mesh 3D representation of the Digimouse virtual phantom and approximate location of coronal slice used for SAXS-CT simulations. (B.) A coronal slice through the voxelized phantom with color bar showing material indicies tabulated in Tab. 7.1. (C.) Cylindrical regions of plaque were inserted at locations within the gray and white matter of the slice. The diameter of the plaque regions were 0.1, 0.4, and 0.6 mm.

Table 7.1 and Table 7.2 shows the tissue material present in the selected slices. We obtained density estimates of the various tissues from the International Commission on Radiation Units & Measurements (ICRU) and the International Comission on Radiation Protection (ICRP). For a few materials, we supplied empirical x-ray scattering measurements at small angles to accurately reflect the material's molecular interference factors (MIF). For other materials, at the perimeter of the head, we allowed simulations the theoretically calculate the independent atomic approximation (IAA) of x-ray scattering at small angles based on the elemental composition of the materials. The MIF more accurately reflects reality because it accounts for the structure factor effects in SAXS.

Fig. 7.1 shows the Digimouse virtual phantom and the approximate location of the coronal slice used for SAXS-CT simulations. We inserted regions of 0.1, 0.4, and 0.6 mm diameter for neurological plaques. The MIF of the neurological plaques were from measurements of a BSA amyloid model on brain tissue. Fig. 7.2 shows a

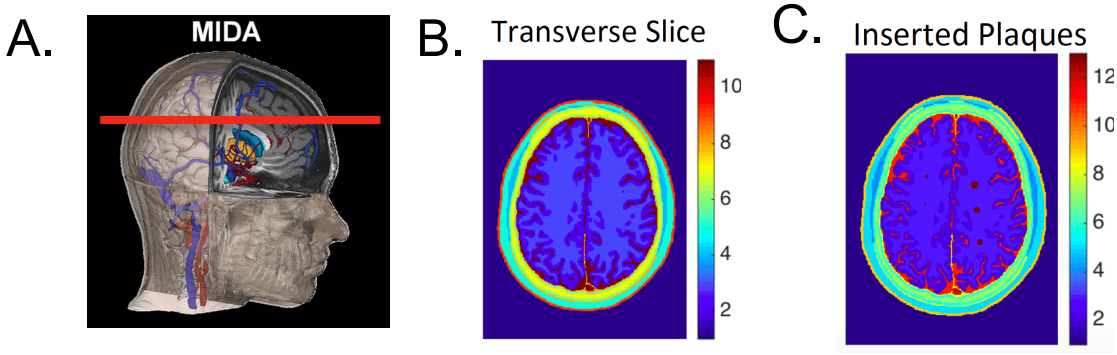


Figure 7.2: (A.) A representation of the MIDA virtual phantom and a line is drawn at the approximate location of the transverse slice used for SAXS-CT simulations. (B.) A transverse slice through the voxelized phantom with color bar showing material indicies tabulated in Tab. 7.2. (C.) Cylindrical regions of plaque were inserted at locations within the white matter of the slice. The diameter of the plaque regions were 0.05, 0.2, 0.3, 0.4, 0.5, and 0.6 mm.

representation of the MIDA phantom with an approximate location of the transverse slice used for SAXS-CT simulations. The size of the inserted neurological plaques are 0.05, 0.2, 0.3, 0.4, 0.5, and 0.6 mm in diameter.

We simulated SAXS-CT with 0.1 mm translation steps for Digimouse and 0.05 mm translation steps for MIDA which were chosen because of the phantom's respective voxel size. We simulated 360 projections with 1 degree angular steps around the phantom to reconstruct CT slice using filtered back projection. Since Digimouse is a smaller phantom, we simulated runs with a monochromatic 16, 20, and 33 keV x rays. $10^8$ x-ray histories per translation position per projection totalling $5.6 \times 10^{13}$ total x-ray trajectories simulated for a CT slice. The total time for each set of SAXS-CT simulated on Digimouse phantom was approximately 2.5 hours. For MIDA phantom, we simulated at higher monochromatic x-ray energies (60 and 70 keV) to account for the larger size (16-20cm). We also increased number of histories simulated to $10^9$ per translation position per projection totalling $1.7 \times$

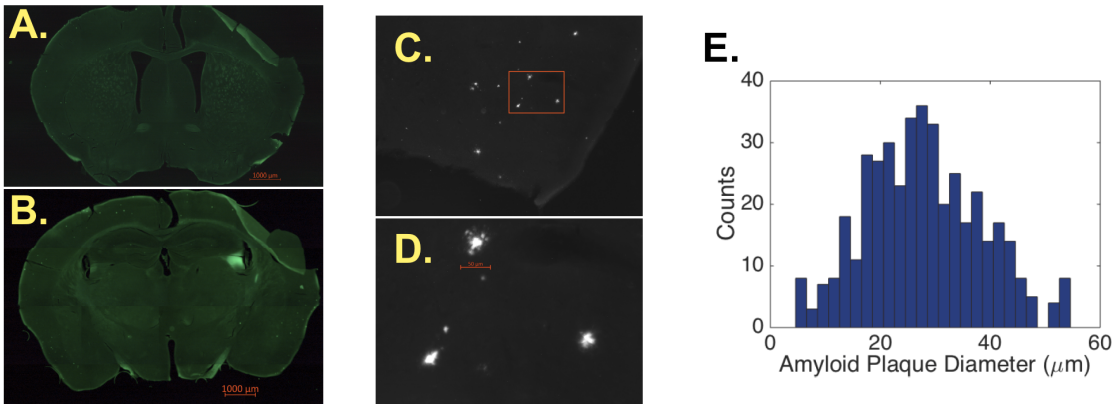


Figure 7.3: (A and B.) Two whole slice fluorescent microscopy images of Tg mouse brain with Thioflavin S dye using a 5x objective, 450 nm excitation, and 550 nm emissions. (C.) A 20x zoom in on the bottom right corner of one Tg slices showing amyloid deposits. (D.) 40x zoom of the red box region in C. showing approximate size of the amyloid. (E.) The diameter of 420 amyloid plaques were manually measured using ImageJ software in 5 different Tg histological slices to provide a size distribution.

$10^{14}$ total x-ray trajectories simulated for a CT slice. The total time for each set of SAXS-CT simulated on MIDA phantom was approximately 4.2 days.

## 7.3 Results

From our histological analysis, we learned that the mean diameter of the plaques in our Tg mouse brains was 27.9±10.5 $\mu$m ($\pm\sigma$ of 420 counted plaques). The amyloid load in the neocortex region of the brain was estimated to be 0.0013 determined by the volume of plaques over the volume in the neocortex region. Fig. 7.3 shows two of the five histology slices imaged, an image of a few amyloids, and the distribution of amyloid plaque sizes found in 5 slices studied.

Figs. 7.4 and 7.5 show photograph, histology, and PSAXS measurement comparisons of two transgenic AD mouse model brain slices. The histology slice was

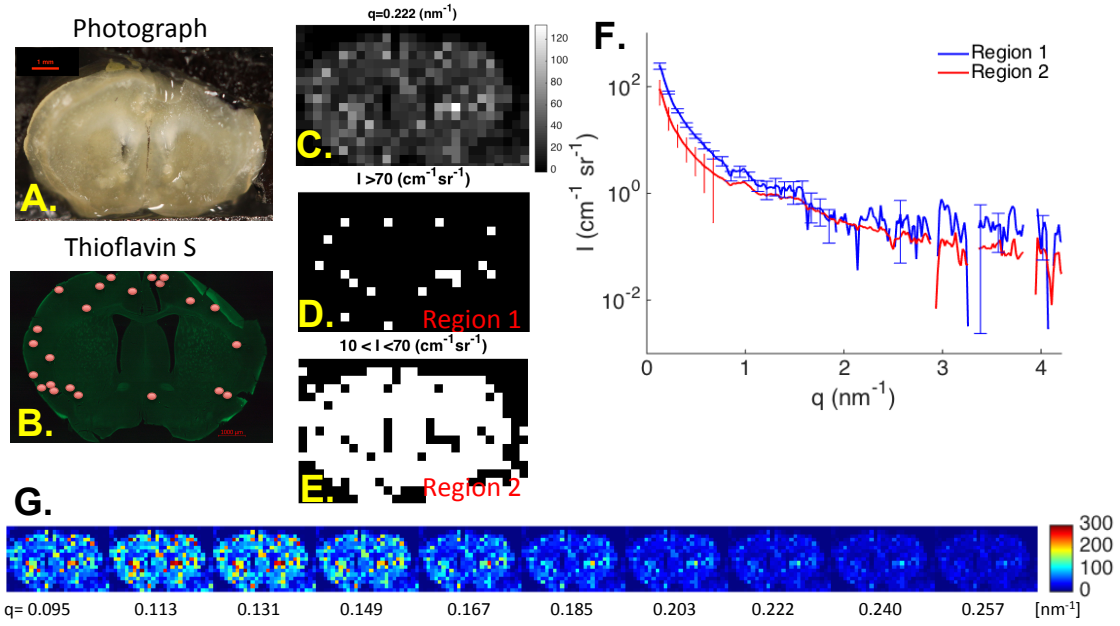


Figure 7.4: (A.) Photograph of the 1 mm Tg brain slice measured. (B.) Fluorescent microscopy image of the corresponding subsequent slice. Red dots are added to improve visualization of the amyloid plaque locations. (C.) Intensity map at $q$ at 0.22 nm$^{-1}$. (D and E.) are intensity-based segmentation of C. (F.) Average scatter profile of pixel regions from D and E. (G.) Intensity maps for the first 10 $q$ bins.

a subsequent slice at 40 $\mu$m. Because of the small size of the plaques (28 $\mu$m in diameter), we placed red dots to show locations where plaques were found. Using a $q$ intensity map at a small angle, intensity-based segmentation was performed to find pixels with potential amyloid plaques on the basis that plaques are expected to have higher intensities at lower angles. The pixels that had higher intensities at the selected small-angle $q$ appeared in the neocortex region of each of the slices. Fig. 7.4 shows region 1 also had a upward curve in intensities at small-angles compared to the rest of the brain region.

Transgenic AD mouse model measurement results were compared to a wild-type mouse brain measurement. We segmented the intensities in similar way at small-angles and found the higher intensities to exsist in the corpus callosum region

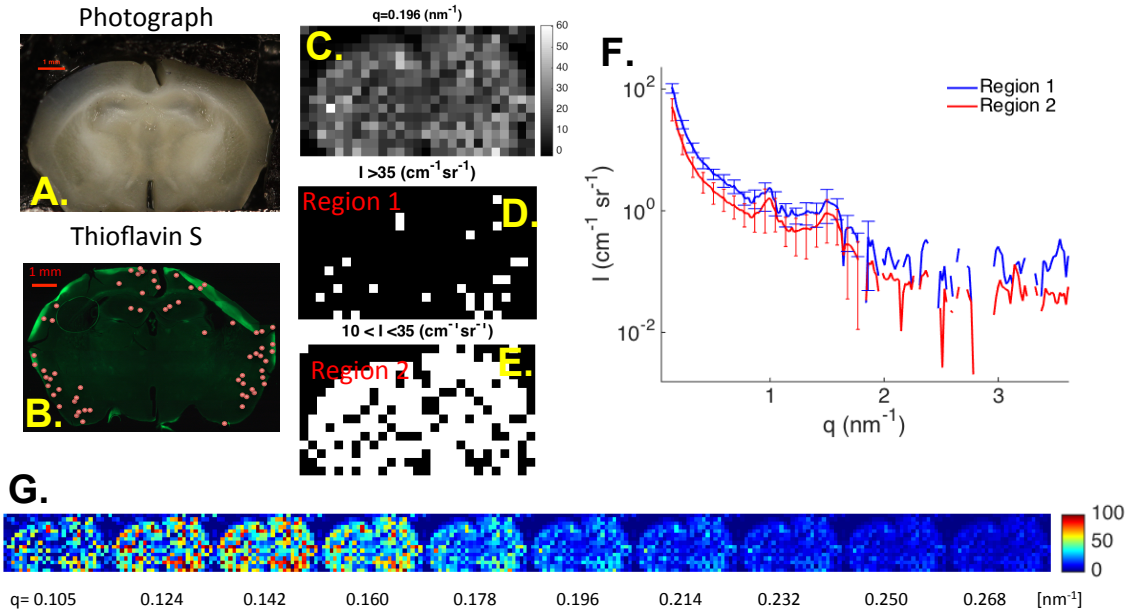


Figure 7.5: (A.) Photograph of the 1 mm Tg brain slice measured. ( B.) Fluorescent microscopy image of the corresponding subsequent slice. Red dots are added to improve visualization of the amyloid plaque locations. (C.) Intensity map at $q$ at 0.22 nm$^{-1}$. (D and E.) are intensity-based segmentation of C. (F.) Average scatter profiles of pixel regions from D and E. (G.) Intensity maps for the first 10 $q$ bins.

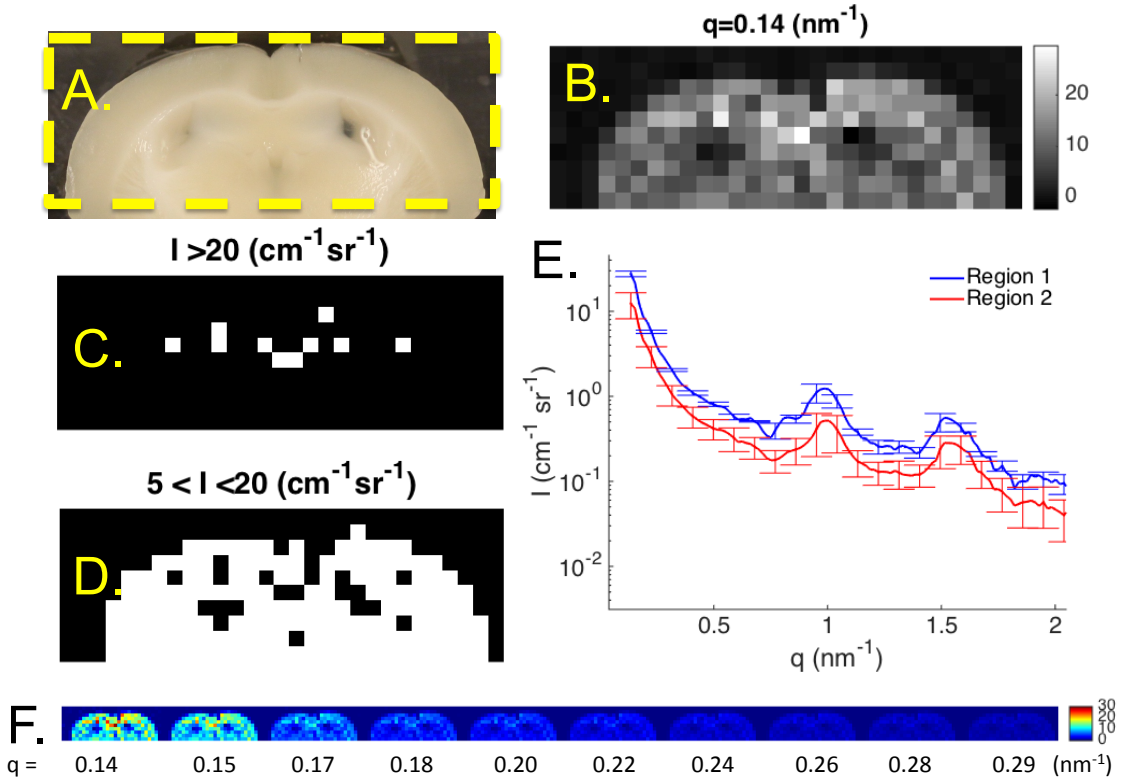


Figure 7.6: (A.) Photograph of the 1 mm WT brain slice measured. (B.) Intensity map at $q$ at 0.14 nm$^{-1}$. (C and D.) are intensity-based segmentation of B. (E.) Average scatter profile of pixel regions from C and D. ( F.) Intensity maps for the first 10 $q$ bins.

of the brain slice. The average scatter profiles from each region also showed a similar profile, except for the higher intensity in region 1 which could be due to higher density of myelin in the corpus callosum region. The expected upward turn at small-angles was not apparent in this measurement as it were in the transgenic AD brain measurements.

To assess the influence of instrument noise, we did a high resolution measurement with 50 $\mu$m steps as opposed to 250 $\mu$m performed for other whole slice PSAXS measurements. We selected the bottom left corner of another Tg brain slice. Each location was measured for 300 s. This measurement on the same region-of-interest

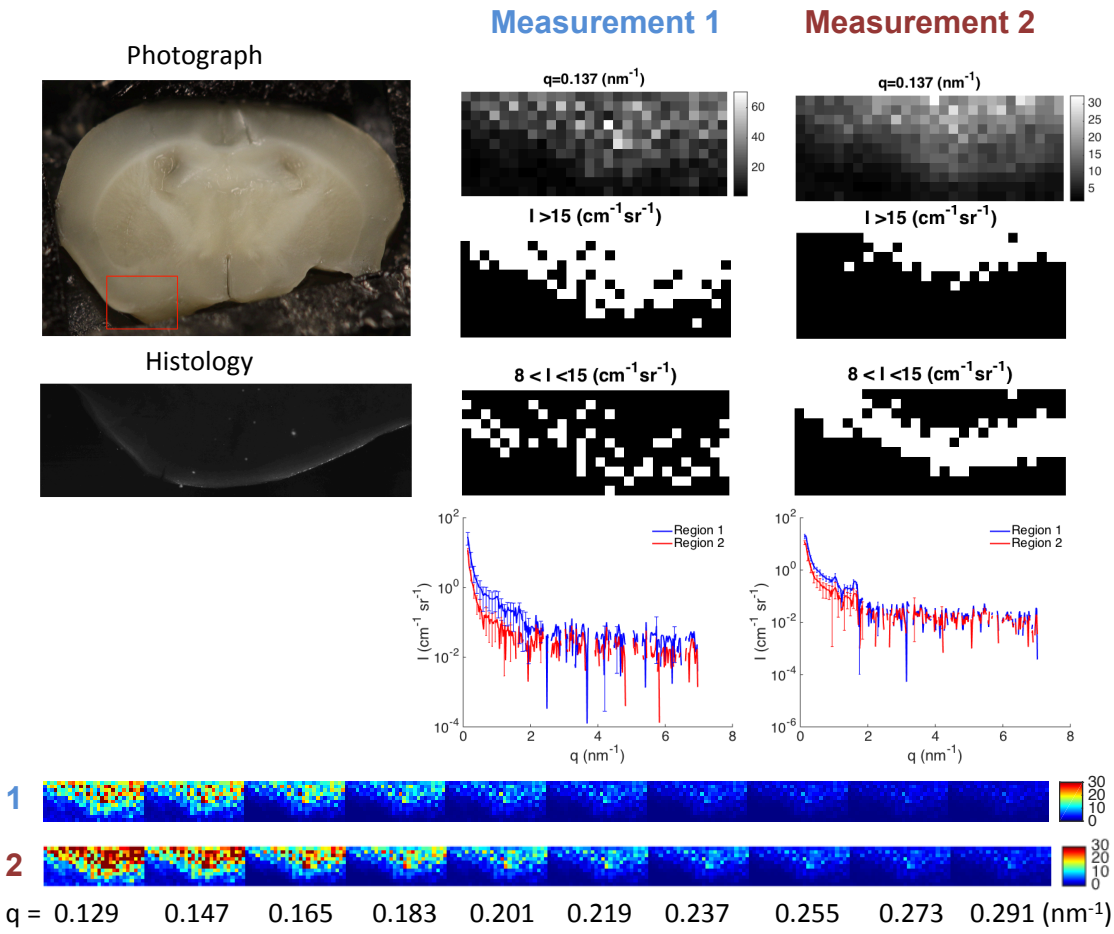


Figure 7.7: (Left) Photograph of measured brain slice with a red box indicating region-of-interest. Histology of that location in a subsequent slice is shown below the photograph. Middle and right columns show two repetition measurements of the same region. Bottom shows the first 10 $q$ bins of both sets of measurements.

was performed again and compared in Fig. 7.7. The second measurement set had higher intensities than the first set, however the high intensity regions were consistently in the same location shown at the bottom $q$ bin images in Fig. 7.7. The repetition experiment indicates longer exposure time is needed to remove effects of instrument noise as determined by differences in images from the two sets.

Fig. 7.8 shows a photograph of the measured brain slice. The BSA fibrils are not visible in this image. However they are visible in the PSAXS images in Fig. 7.9

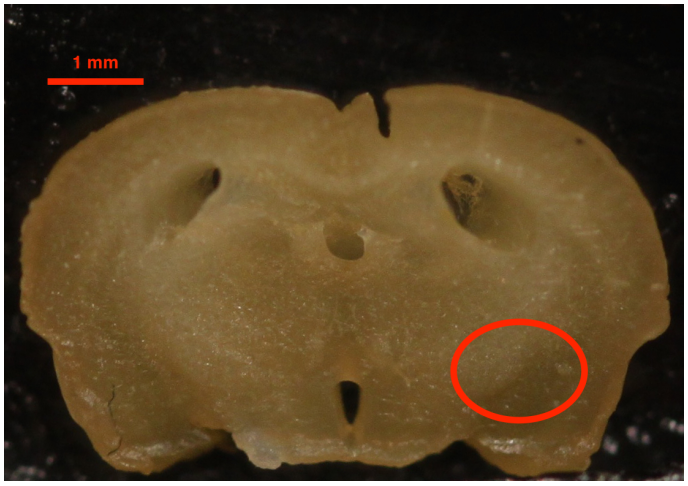


Figure 7.8: Photograph of coronal slice of wild-type mouse brain acquired after measurements. Location where BSA fibril pellet was placed is marked with red circle.

which shows each $q$ intensity map. The BSA fibrils are aggregates that have higher intensities at low $q$ angles therefore the first 10 images show the highest contrast of the BSA fibrils compared to the rest of the brain tissue.

Using a intensity threshold approach, we segmented regions of BSA fibrils, white matter, and gray matter. The BSA fibrils were segmented by the intensity map at $q$ of 0.21 $nm^{-1}$ and thresholding above 21 $cm^{-1}$ $sr^{-1}$. The white matter and gray matter were segmented by intensity map the first peak at a $q$ of 0.95 $nm^{-1}$ and thresholding from 2 to 4 $cm^{-1}$ $sr^{-1}$ for white matter and 0.7 to 1.5 $cm^{-1}$ $sr^{-1}$ for gray matter. The results of these segmentated regions and their average scatter profiles are presented in Fig. 7.10.

Fig. 7.11 and Fig. 7.12 shows the MC-GPU simulation results of SAXS-CT on a slice of Digimouse and MIDA virtual phantoms with embedded regions of neurological plaques of varying sizes. Fig. 7.11 shows that 16 keV for 1.5 cm thick mouse head may be too low because of attenuation of the x-rays at the skull. 16 keV

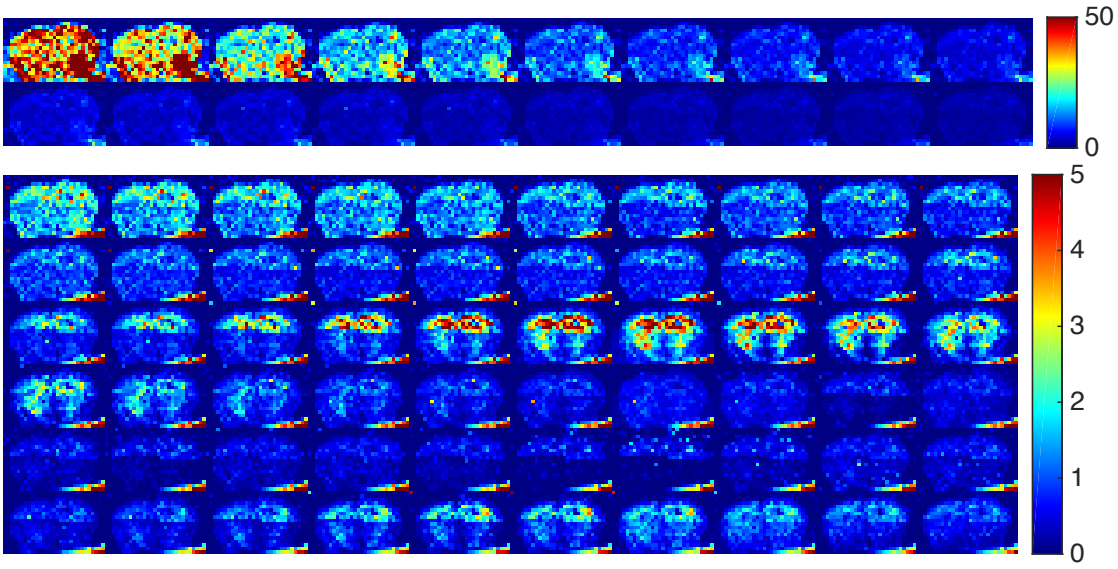


Figure 7.9: Montage of each $q$ bin intensity map for a slice of wild-type brain with superimposed BSA fibrils.

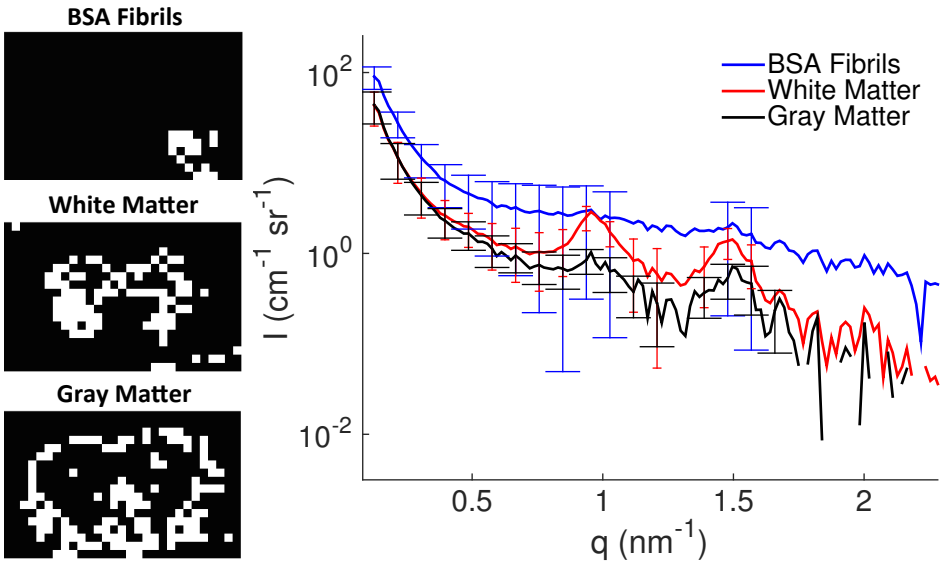


Figure 7.10: (Left) Result of pixel segmentation based on intensity thresholds for BSA fibrils, white matter, and gray matter. (Right) Average of scatter profiles for pixels segmented with $\pm\sigma$ represented every 5 points.

| Energy (keV) | Total Dose (Gy) |
|---|---|
| 16 | 6.08 |
| 20 | 6.42 |
| 33 | 4.42 |

Table 7.3: Total Dose for 16, 20, and 33 keV SAXS-CT measurement of Digimouse slice.

| Energy (keV) | Total Dose (Gy) |
|---|---|
| 60 | 0.015 |
| 70 | 0.053 |

Table 7.4: Total Dose for 60 and 70 keV SAXS-CT measurement of MIDA slice.

shows undersampling artifacts in the reconstructed CT images at various angles. Artifacts are reduced in the measurement set at 20 keV and further reduced in measurements with 33 keV. In the measurement set with 33 keV x rays, even the smallest plaque at 0.1 mm is visible in the white matter at small-angles.

Simulation results shown in Fig. 7.12 for the MIDA human head slice show neurological plaques down to 0.3 mm in diameter. Because the human head is much thicker at approximately 16-20 cm, higher energy x rays are needed to escape the tissue. However, a larger proportion of x rays at high energies will also be transmitted with no interaction with the tissue, therefore we simulated these sets with 10 times the number of x rays to improve signal.

Table 7.3 presents the estimated total dose deposited on the Digimouse head for SAXS-CT measurements. Likewise, table 7.4 shows the total dose deposited to the MIDA head. We had calculated less dose deposited on the MIDA head than the Digimouse head due to the higher energy of the x rays used even though more total x rays were simulated for the MIDA head.

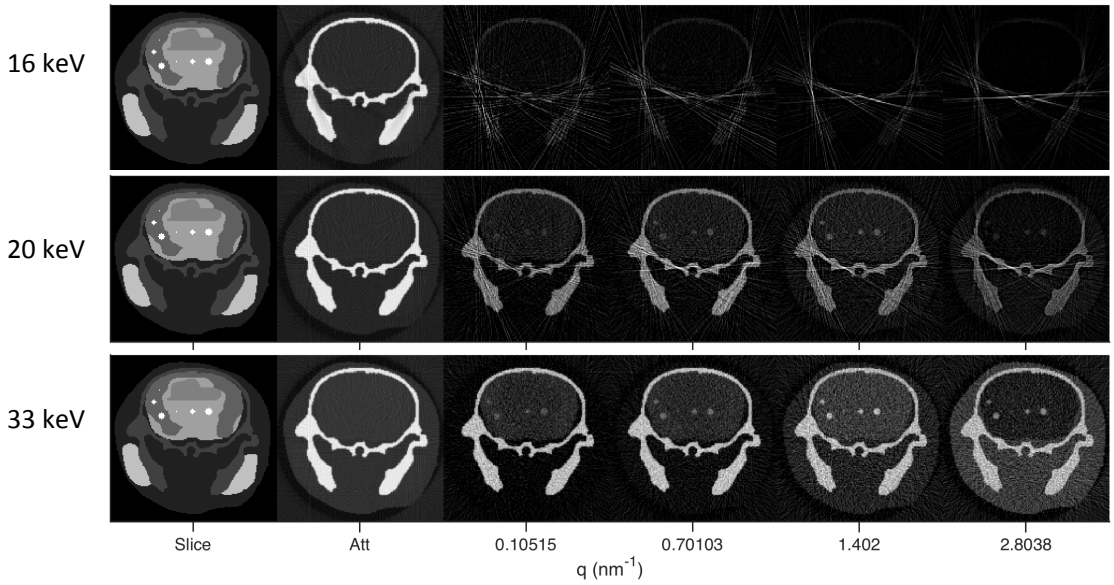


Figure 7.11: SAXS-CT simulation results using MC-GPU on Digimouse slice. First column is a slice through voxel phantom. The second column is the attenuation image. The 3rd to 6th images are intensity maps reconstructed from a specific $q$ angle indicated below the image. First row shows results of simulations with 16 keV x rays, second row shows simulations with 20 keV, and last row shows simulations performed with 33 keV.

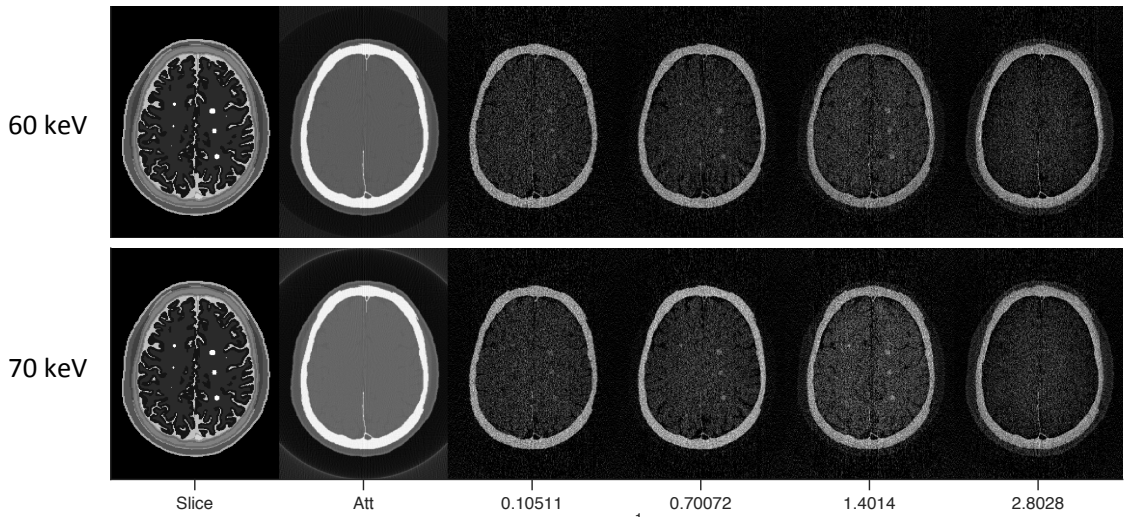


Figure 7.12: SAXS-CT simulation results using MC-GPU on MIDA slice. First column is a slice through voxel phantom. The second column is the attenuation image. The 3rd to 6th images are intensity maps reconstructed from a specific $q$ angle indicated below the image. First row shows results of simulations with 60 keV x rays, bottom row shows simulations performed with 70 keV x rays.

## 7.4 Discussion

In this work, we have performed histological analysis of the amyloid load on Tg mouse brain, measured PSAXS of a few Tg slices, compared results to a WT mouse brain, demonstrated SAXS imaging differentiation of amyloid fibril model on a WT mouse brain, and simulated SAXS-CT on a mouse head and human head with embedded amyloid plaques to demonstrate feasibility.

Through our histological work, we found the plaque sizes to be smaller than the resolution of our PSAXS measurements with a mean diameter of 28 $\mu$m. While it is possible to measure at 10 $\mu$m resolution step sizes and beam size at modern synchrotron sources, our system is limited to a 200 $\mu$m beam size. While we may not be able to measure single neurological plaques with our system, we postulated that if a plaque was within the beam, that there would be increased intensities at small-angles due to the scattering contribution from the plaque or plaques. Because the size of the plaques, we cannot use the subsequent slices that were analyzed with histology for a registration map of these plaques, however, we are able to estimate regions where amyloid exist.

Our measurements of the Tg slices show that pixel locations with high intensities at small-angles are present in regions of the neocortex where plaques are shown to exist in histology. As expected, these pixels showed scatter profiles with increased intensities below 0.5 $nm^{-1}$. We performed the same intensity-based segmentation at small angles on a region of a WT mouse brain and found that the scatter profile of more intense pixel regions did not show the same characteristic upward turn at

small-angles as the Tg brain intense pixels.

In addition, we performed a higher step resolution of 50 $\mu$m with a 200 $\mu$m beam size in a particular region-of-interest in a transgenic brain twice to rule out intense pixel regions due to system noise. While results from the two measurements were not identical, the centers of intense pixel regions were consistent between the two measurements. Differences could be attributed to the long period of time required for measurements. Each set took approximately a week, therefore the same brain slice was in the system for 2 weeks and could have experienced more degradation and drying during measurements. With a known amyloid target at a known location, a signal-to-noise estimate can be ascertained.

We have demonstrated that SAXS imaging can be used to differentiate amyloid fibrils from normal tissue by their small-angle scatter profile characteristics. Aggregation tends to curve upwards at low $q$ angles and this characteristic can be utilized in SAXS imaging to locate and track growth of brain plaques *in vivo* without the use of any contrast agents or molecular tags. We demonstrate this with a model amyloid system of BSA fibrils where the amyloid target could be placed at a known location and with a known size.

The BSA fibril pellet was mostly translucent and after placing on the brain slice, it was difficult to locate. The BSA fibrils are not visible in the photograph in Fig. 7.8 but are clearly visible in the SAXS images shown in Fig. 7.9.

A corpus callosum structure is apparent in the 5th row and again in the 8th row in Fig. 7.9. This is due to the highly scattering myelin structure that is most dense in the corpus callosum. The images in these rows correspond to the two peaks

in the scattering profile in Fig. 7.10 at $q$ of 0.95 and 1.6 $nm^{-1}$. The gray matter region also have these peaks but they are more diffuse. They are also apparent in the BSA fibril average signal since the fibrils were superimposed on brain tissue.

A large contributor to our success in detecting amyloid fibrils was the density of the fibrils measured since density affects intensity scale in scatter profiles. The density of BSA amyloid fibrils was estimated to be approximately 31.5 $mg/cm^3$ and the approximate amyloid load was calculated to be 0.0997 which is within normal range of amyloid plaque in Tg mice 12 to 70 weeks old. [67] This was much higher than the calculated amyloid load of the Tg brains that we had which were 0.0013. PSAXS signal quality is affected by sample thickness and therefore applications are limited to *ex vivo* biopsy studies. However, SAXS computed tomography (SAXS-CT) uses image reconstruction algorithms to obtain SAXS profiles of locations deep within objects enabling applications in *in vivo* molecular x-ray imaging. This technique has been demonstrated study biological tissues and plastics. [39, 46, 47, 52, 75, 91] Simulations of the Digimouse head show that 33 keV x rays achieve increased signal and minimize dose over 16 and 20 keV x rays. The MIDA phantom simulation show a minor improvement in signal quality in the 70 keV x-ray simulation over the 60 keV x-ray simulation determined by ability to see the 0.3 mm diameter embedded plaque. The 0.2 mm and 0.1 mm plaque sizes were not visible in these images. Higher energy x rays and larger number of x rays are needed for SAXS-CT imaging of a human head. The optimal energy that balances signal and dose have yet to be determined for a mouse and human. However, we have determined that it is theoretically feasible to measure plaques at higher resolution than existing *in vivo*

amyloid imaging methods.

## 7.5 Conclusion

We demonstrate feasibility of SAXS imaging of amyloid. Transgenic Alzheimer's disease (AD) mouse brains and a wild-type mouse brain were measured using planar SAXS and compared. Amyloid plaques were found to have higher intensities at small angles and intensity maps at $q$ bins below 0.5 $nm^{-1}$ is the range that was investigated for detection of amyloid targets. However, amyloid plaque detection in our SAXS system is limited by amyloid size and density. Histological analysis of 40 $\mu$m thick subsequent slices to 1 mm slices we imaged using planar SAXS showed the distribution of plaque sizes centered around 28 $\mu$m in diameter with a $\sigma$ of $\pm 10$ $\mu$m from 420 plaques counted in transgenic AD mouse brains. The plaques also appeared more frequently in the neocortical region of the brain slices. Our SAXS system spatial resolution was limited by the beamsize which was 200 $\mu$m in diameter and was not well-suited for detection of individual plaques in transgenic AD mice. A SAXS system with beamsizes and scanning step sizes $\leq$10 nm would be better suited for detection of individual amyloid plaques in transgenic AD mice. In spite of our SAXS system spatial resolution limitation, we have found higher intensity pixels in intensity maps at $q$ bins below 0.5 $nm^{-1}$ in the neocortex region where plaques are known appear in higher frequency. The x-ray scattering contribution from a single or multiple plaques within the SAXS beam assisted in a coarse detection of plaques. To further demonstrate feasibility of amyloid detection, we

utilized an amyloid fibril model from bovine serum albumin with 0.8 mm diameter and placed it at a known location on a wild-type mouse brain slice and we were able to spatially locate the plaque. The estimated amyloid load of this fabricated AD model was 0.0997 which is within normal range of amyloid plaque in Tg mice 12 to 70 weeks old. Finally, we performed x-ray transport simulations of SAXS-CT of a virtual mouse model head (Digimouse) and a virtual human head (MIDA). The simulations performed on Digimouse showed that for a mouse head approximately 1-2 cm in diameter, 33 keV x rays were optimal for detection of plaques down to 0.1 mm in diameter. 33 keV x rays also had the least amount of radiation dose deposited (4.42 Gy) to the head compared to measurements with 16 (6.08 Gy) and 20 keV (6.42 Gy). Simulations performed on the MIDA human head phantom, showed that with 70 keV x rays, the minimum detectable plaque size was 0.3 mm diameter, and with 60 keV x rays, the minimum detectable plaque size was 0.4 mm diameter. However, SAXS-CT simulations using 60 keV had 15 mGy dose deposited whereas simulations using 70 keV had 53 mGy. Also, higher energy x rays for human head applications also required higher number of total x rays simulated to obtain enough scattering signal to distinguish plaque regions because a larger proportion of the x rays transmit without interaction. Further simulations are needed to fine tune optimal x-ray energies for small animal and SAXS-CT human head imaging for amyloid plaques. However, the outlook of utilizing SAXS-CT imaging for *in vivo* detection of amyloid plaque is promising. We have demonstrated simulations could be used to design dedicated SAXS-CT systems for small-animal and human amyloid imaging applications.

# Chapter 8: Future Work

Small-angle x-ray scattering techniques for medical imaging have been advanced by the work presented in this dissertation. We initially explored biomarkers *in vitro* and observed aggregation growth of $\beta$ amyloid and tau two time points of SAXS measurements. We developed a method of incorporating experimentally measured cross sections into a GPU-accelerated Monte Carlo simulation tool of x-ray transport to improve realism at small-angles and study optimal energy and thickness for a potential *in vivo* application of SAXS imaging. We also proposed a method to study depth limit of SAXS-CT systems. A comprehensive study on SAXS and XRD studies of mouse brain were reviewed and compared to our own results of PSAXS measurements. We imaged planar SAXS of transgenic Alzheimer's disease mouse model brains and compared them to histology and wild-type measurements. We were successfully able to image and locate an amyloid fibril model constructed from BSA on a wild-type mouse brain slice. Finally, simulations of SAXS-CT of mouse and human head with embedded neurological plaques were performed and results demonstrated theoretical feasibility to image amyloid plaques *in vivo* with optimized instrument settings.

Because amyloid plaques are aggregates of $\beta$ amyloid, small-angle x-ray scat-

tering is the appropriate angular range to look for differentiating cross section between that and of regular tissue. We found that amyloid scatter profiles in the brain curved upwards at $q \geq 0.5$ nm$^{-1}$. The upward turn at $q \geq 0.5$ nm$^{-1}$ characteristic of amyloid plaque could serve as a biomarker for Alzheimer's disease *in vivo*. Simulations of SAXS-CT system using 33 keV x rays allowed for detection of neurological plaques down to 0.1 mm diameter within a virtual mouse head with a CT slice size of 1.5x1.5 cm$^2$ and the estimated radiation dose deposited on the mouse head for one slice was 4.42 Gy. 16 and 20 keV energies were also probed for mouse head SAXS-CT imaging applications, however, simulations using 33 keV x rays produced the least amount of undersampling artifacts for the same number of x rays simulated ($10^{13}$ x rays) and also produced the least amount of dose deposited. We also performed simulations of SAXS-CT with 60 and 70 keV x rays on a virtual human head between 16-20 cm in diameter. We simulated 10 times the number of x rays for the virtual human head to increase the amount of x rays reaching the detector. 0.4 and 0.3 mm diameter plaques were detected with an estimated radiation dose of 0.015 and 0.053 Gy in SAXS-CT simulations with 60 and 70 keV respectively. Smaller plaques could theoretically be detected with more simulated x-rays histories. Simulations of a mouse head and human head reveal that SAXS-CT could be used to image amyloid plaques *in vivo*. Further work is needed to more finely assess optimal x-ray energies to use for small-animal and human heads for detection of plaques between 10 to 50 $\mu$m in diameter. From our initial work we have found 33 keV optimal for mouse head and between 60 to 70 keV for a human head.

There are still key challenges that need to be addressed for SAXS-CT to be

a practical tool for *in vivo* amyloid imaging. The dose to the sample should be minimized and measurement times need to be reduced. The current upper limit for clinical head CT for humans is 60-80 mGy. [58] Our simulations of SAXS-CT with 60 keV x rays deposited only 15 mGy in the human head and we were able to detect plaques of size 0.3 mm in diameter. Through histological analysis, we found the size of amyloid plaques in transgenic AD mice were about 10 times smaller at approximately 0.03 mm in diameter and amyloid plaques are reported to be a similar size in humans. [78] Step sizes and smaller beams below 10 $\mu$m are necessary for the detection of individual plaques. Synchrotron sources can already achieve a 10 $\mu m^2$ beamsize using x-ray microfocusing instrumentation. In addition, synchrotron SAXS sources have x-ray flux of $10^8$ x rays/s/$\mu m^2$ as opposed to laboratory SAXS sources with x-ray flux of approximately $10^2$ x rays/s/$\mu m^2$. Given the flux and beam size specification of synchrotron sources, individual amyloid plaque imaging using SAXS-CT may be feasible at measurement times in the order of a few minutes to a few hours depending on the step resolution and number of projections used. However, laboratory SAXS-CT system for amyloid imaging at present requires days. For practical use in clinics and for *in vivo* amyloid imaging, measurement times need to be reduced in SAXS-CT systems. One approach to shorten measurement times in laboratory systems is the use of liquid metal jet sources which allow flexibility in x-ray spectra and higher flux. In addition, the use of 2D spectroscopic x-ray detectors eliminate the need to filter x rays for monochromation and allow for more efficient usage of x rays generated. The entire spectra of x rays generated could be collected and each energy bin could be used to calculate a different scattering

angle. With energy bins below 1 keV, the wavelength effect of smearing on the scatter profile becomes negligible. Furthermore, measurement times can be reduced by locally imaging a smaller region-of-interest.

In another approach, SAXS imaging could be used more coarsely to assess amyloid load by the contribution of x-ray scattering from multiple plaques illuminated within a larger beam (0.1-1 $mm^2$). Shorter measurement times are achieved by lower resolution scanning and larger beamsizes. Denser plaque regions would contribute more to higher intensities below 0.5 $nm^{-1}$. We have planar SAXS imaged transgenic AD mouse brains slices with 0.2 $mm^2$ beam. Higher intensities are present in intensity maps at 0.22 $nm^{-1}$ in the neocortical regions where histology of subsequent slices show plaques to be present. More work is needed to correlate intensity of these regions to amyloid load, a metric commonly used clinically to assess progression of Alzheimer's disease. Theoretically, the measured scatter profile is a linear combination of individual material scatter profiles. A least-squares approximation of measured scatter profiles with basis functions formed by known cross sections of amyloid plaques and brain tissues could be used to estimate amyloid load in any pixel in a SAXS-CT image.

The outlook of SAXS imaging for applications in medical imaging is promising for assessing pathology by structural tissue differentiation between normal and diseased states. As a result of the work performed during this PhD program, knowledge in the field of SAXS imaging for medical applications has been advanced and evidence of feasibility for SAXS-CT imaging for detection of amyloid plaques is stronger. Optimization of maximized signal and minimized dose for small animals

and humans could be addressed *in silico* using MC-GPU simulations along with the design of dedicated SAXS-CT systems for amyloid detection. We also plan to develop a hybrid energy-dispersive, angular-dispersive SAXS-CT system using a 2D spectroscopic x-ray detector to collect all generated x-rays and assess improvements in measurement times. Concurrently, we plan to also use planar SAXS to further study correlation of scattering intensities below 0.5 $nm^{-1}$ to amyloid load in brain tissues of transgenic and wild-type mice. Techniques to assess image quality quantitatively will be developed and implemented.

# Bibliography


[1] *Diagnostic and Statistical Manual of Mental Disorders: DSM-5*. American Psychiatric Association, 2003.

[2] Guidance for Industry, Alzheimers disease: Developing drugs for the treatment of early stage disease. Draft Guidance, 2013. US Department of Health and Human Services Food and Drug Administration. *Center for Drug Evaluation and Research (CDER)*, 16, 2013.

[3] 2017 Alzheimer's disease facts and figures. *Alzheimer's & Dementia*, 12(4):459–509, 2017.

[4] M. Ahmed, J. Davis, D. Aucoin, T. Sato, S. Ahuja, S. Aimoto, J. I. Elliott, W. E. Van Nostrand, and S. O. Smith. Structural conversion of neurotoxic amyloid-$\beta$ 1-42 oligomers to fibrils. *Nature Structural & Molecular Biology*, 17(5):561–567, 2010.

[5] N. Alam*, M. Choi*, B. Ghammraoui, E. Dahal, and A. Badano. Small-angle x-ray scattering cross-section measurements of imaging materials. *Biomedical Physics and Engineering Express*, 2017.

[6] N. Allec, M. Choi, N. Yesupriya, B. Szychowski, M. White, M. Kann, E. Garcin, M.-C. Daniel, and A. Badano. Small-angle x-ray scattering method to characterize molecular interactions: Proof of concept. *Scientific Reports*, 5(12085), 2015.

[7] R. L. Avila, H. Inouye, R. C. Baek, X. Yin, B. D. Trapp, M. L. Feltri, L. Wrabetz, and D. A. Kirschner. Structure and stability of internodal myelin in mouse models of hereditary neuropathy. *Journal of Neuropathology & Experimental Neurology*, 64(11):976–990, 2005.

[8] G. B and P. LM. Non-invasive classification of breast microcalcifications using x-ray coherent scatter computed tomography. *Physics in Medicine and Biology*, 62(3):1192, 2017.

[9] A. Badal and A. Badano. Accelerating Monte Carlo simulations of photon transport in a voxelized geometry using a massively parallel graphics processing unit. *Medical Physics*, 36(11):4878–4880, 2009.

[10] A. Badal and A. Badano. SU-E-I-68: Fast and accurate estimation of organ doses in medical imaging using a GPU-accelerated Monte Carlo simulation code. *Medical Physics*, 38(6):3411–3411, 2011.

[11] C. Ballard, S. Gauthier, A. Corbett, C. Brayne, D. Aarsland, and E. Jones. Alzheimer's disease. *The Lancet*, 377(9770):1019–1031, 2011.

[12] S. Barna, M. Tate, S. Gruner, and E. Eikenberry. Calibration procedures for charge-coupled device x-ray detectors. *Review of Scientific Instruments*, 70(7):2927–2934, 1999.

[13] M. Bernhardt, J. Nicolas, M. Eckermann, B. Eltzner, F. Rehfeldt, and T. Salditt. Anisotropic x-ray scattering and orientation fields in cardiac tissue cells. *New Journal of Physics*, 19(1):013012, 2017.

[14] T. Blanton, T. Huang, H. Toraya, C. Hubbard, S. Robie, D. Louer, H. Göbel, G. Will, R. Gilles, and T. Raftery. JCPDS International Centre for Diffraction Data round robin study of silver behenate. A possible low-angle x-ray diffraction calibration standard. *Powder Diffraction*, 10(02):91–95, 1995.

[15] L. Chia, J. Thompson, and M. Moscarello. X-ray diffraction evidence for myelin disorder in brain from humans with Alzheimer's disease. *Biochimica et Biophysica Acta (BBA) - Biomembranes*, 775(3):308–312, 1984.

[16] M. Choi, N. Alam, E. Dahal, B. Ghammraoui, and A. Badano. Alzheimer's disease imaging biomarkers using small-angle x-ray scattering. In *SPIE Medical Imaging*, pages 978802–978802. International Society for Optics and Photonics, 2016.

[17] M. Choi and A. Badano. Planar small-angle x-ray scattering imaging of phantoms and biological samples. *Applied Physics Letters*, 110(15):153106, 2017.

[18] M. Choi, B. Ghammraoui, A. Badal, and A. Badano. Method to study sample object size limit of small-angle x-ray scattering computed tomography. In *SPIE Medical Imaging*, pages 97831Z–97831Z. International Society for Optics and Photonics, 2016.

[19] M. Choi, B. Ghammraoui, A. Badal, and A. Badano. Monte Carlo x-ray transport simulation of small-angle x-ray scattering instruments using measured sample cross sections. *Journal of Applied Crystallography*, 49(1), 2016.

[20] A. Christ, W. Kainz, E. G. Hahn, K. Honegger, M. Zefferer, E. Neufeld, W. Rascher, R. Janka, W. Bautz, J. Chen, et al. The Virtual Family development of surface-based anatomical models of two adults and two children for dosimetric simulations. *Physics in Medicine and Biology*, 55(2):N23, 2009.

[21] A. M. Cormack. Representation of a function by its line integrals, with some radiological applications. *Journal of Applied Physics*, 34(9):2722–2727, 1963.

[22] E. Dahal, M. Choi, N. Alam, A. Bhirde, S. Beaucage, and A. Badano. Structural evaluation of an amyloid fibril model using small-angle x-ray scattering. *Physical Biology (In submission)*, 2017.

[23] M. De Felici, R. Felici, C. Ferrero, A. Tartari, M. Gambaccini, and S. Finet. Structural characterization of the human cerebral myelin sheath by small angle x-ray scattering. *Physics in Medicine and Biology*, 53(20):5675, 2008.

[24] N. J. Dougall, S. Bruggink, and K. P. Ebmeier. Systematic review of the diagnostic accuracy of $^{99m}$Tc-HMPAO-SPECT in dementia. *American Journal of Geriatric Psychiatry*, 12(6):554–570, 2004.

[25] T. Eichner and S. E. Radford. A diversity of assembly mechanisms of a generic amyloid fold. *Molecular Cell*, 43(1):8–18, 2011.

[26] L. Feigin, D. I. Svergun, and G. W. Taylor. *Structure analysis by small-angle X-ray and neutron scattering*. Springer, 1987.

[27] M. Fernández, J. Keyriläinen, R. Serimaa, M. Torkkeli, M.-L. Karjalainen-Lindsberg, M. Leidenius, K. von Smitten, M. Tenhunen, S. Fiedler, A. Bravin, et al. Human breast cancer in vitro: matching histo-pathology with small-angle x-ray scattering and diffraction enhanced x-ray imaging. *Physics in Medicine and Biology*, 50(13):2991, 2005.

[28] B. Ghammraoui and A. Badal. Monte Carlo simulation of novel breast imaging modalities based on coherent x-ray scattering. *Physics in Medicine and Biology*, 59(13):3501, 2014.

[29] B. Ghammraoui, A. Badal, and L. M. Popescu. Multiple-component object representation and iterative reconstruction for x-ray coherent scattering imaging of the breast. In *The 13th Int. Meeting on Fully Three-Dimensional Image Reconstruction in Radiology and Nuclear Medicine*, 2015.

[30] B. Ghammraoui, L. M. Popescu, and A. Badal. Monte Carlo evaluation of the relationship between absorbed dose and contrast-to-noise ratio in coherent scatter breast CT. In *SPIE Medical Imaging*, pages 94121G–94121G. International Society for Optics and Photonics, 2015.

[31] O. Glatter. A new method for the evaluation of small-angle scattering data. *Journal of Applied Crystallography*, 10(5):415–421, Oct 1977.

[32] A. Gourrier, W. Wagermaier, M. Burghammer, D. Lammie, H. S. Gupta, P. Fratzl, C. Riekel, T. J. Wess, and O. Paris. Scanning x-ray imaging with small-angle scattering contrast. *Journal of Applied Crystallography*, 40:s78–s82, 2007.

[33] A. Guiner, G. Fournet, and C. Walker. Small angle scattering of x-rays. *J. Wiley & Sons, New York*, 1955.

[34] A. Guinier. The diffusion of x-rays under the extremely weak angles applied to the study of fine particles and colloidal suspension. *Comptes Rendus Hebdomadaires Des Seances De L Academie Des Sciences*, 206:1374–1376, 1938.

[35] A. Guinier. Un nouveau type de diagrammes de rayons X. *Comptes Rendus Hebdomadaires Seances l'Academie Sciences*, 206:1641–1643, May 1938.

[36] A. Guinier. *X-ray diffraction in crystals, imperfect crystals, and amorphous bodies*. Courier Corporation, 1994.

[37] O. Hansson, H. Zetterberg, P. Buchhave, E. Londos, K. Blennow, and L. Minthon. Association between CSF biomarkers and incipient Alzheimer's disease in patients with mild cognitive impairment: a follow-up study. *The Lancet Neurology*, 5(3):228–234, 2006.

[38] G. Harding. Effective density and atomic number determined from diffraction profiles. *Proc. SPIE, Hard X-Ray and Gamma-Ray Detector Physics and Penetrating Radiation Systems VIII, 631910*, 2006.

[39] G. Harding, J. Kosanetzky, and U. Neitzel. X-ray diffraction computed tomography. *Medical Physics*, 14(4):515–525, 1987.

[40] L. E. Hebert, J. Weuve, P. A. Scherr, and D. A. Evans. Alzheimer disease in the United States (2010–2050) estimated using the 2010 census. *Neurology*, 80(19):1778–1783, 2013.

[41] G. N. Hounsfield. Computerized transverse axial scanning (tomography): Part 1. description of system. *The British Journal of Radiology*, 46(552):1016–1022, 1973.

[42] J. H. Hubbell, W. J. Veigele, E. A. Briggs, R. T. Brown, D. T. Cromer, and R. J. Howerton. Atomic form factors, incoherent scattering functions, and photon cross sections. *Phys. Chem.*, 4:471–538, 1975.

[43] M. I. Iacono, E. Neufeld, E. Akinnagbe, K. Bower, J. Wolf, I. V. Oikonomidis, D. Sharma, B. Lloyd, B. J. Wilm, M. Wyss, et al. Mida: A multimodal imaging-based detailed anatomical model of the human head and neck. *PloS One*, 10(4), 2015.

[44] H. Inouye, P. E. Fraser, and D. A. Kirschner. Structure of beta-crystallite assemblies formed by alzheimer beta-amyloid protein analogues: analysis by x-ray diffraction. *Biophysical Journal*, 64(2):502–519, 1993.

[45] C. R. Jack, V. J. Lowe, S. D. Weigand, H. J. Wiste, M. L. Senjem, D. S. Knopman, M. M. Shiung, J. L. Gunter, B. F. Boeve, B. J. Kemp, et al. Serial PIB and MRI in normal, mild cognitive impairment and Alzheimer's disease:

implications for sequence of pathological events in Alzheimer's disease. *Brain*, page awp062, 2009.

[46] T. H. Jensen, M. Bech, O. Bunk, A. Menzel, A. Bouchet, G. Le Duc, R. Feidenhans, and F. Pfeiffer. Molecular x-ray computed tomography of myelin in a rat brain. *NeuroImage*, 57(1):124–129, 2011.

[47] T. H. Jensen, M. Bech, O. Bunk, M. Thomsen, A. Menzel, A. Bouchet, G. Le Duc, R. Feidenhans, and F. Pfeiffer. Brain tumor imaging using small-angle x-ray scattering tomography. *Physics in Medicine and Biology*, 56(6):1717, 2011.

[48] H. Kaya. Scattering from cylinders with globular end-caps. *Journal of Applied Crystallography*, 37(2):223–230, Apr 2004.

[49] M. A. Keenan, M. G. Stabin, W. P. Segars, and M. J. Fernald. RADAR realistic animal model series for dose assessment. *Journal of Nuclear Medicine*, 51(3):471–476, 2010.

[50] G. Kidane, R. Speller, G. Hanby, and A. Hanby. X-ray scatter signatures for normal and neoplastic breast tissues. *Physics in Medicine and Biology*, 44:1791–1802, 1999.

[51] D. A. Kirschner, C. Abraham, and D. J. Selkoe. X-ray diffraction from intraneuronal paired helical filaments and extraneuronal amyloid fibers in alzheimer disease indicates cross-beta conformation. *Proceedings of the National Academy of Sciences*, 83(2):503–507, 1986.

[52] U. Kleuker, P. Suortti, W. Weyrich, and P. Spanne. Feasibility study of x-ray diffraction computed tomography for medical imaging. *Physics in Medicine and Biology*, 43(10):2911, 1998.

[53] A. E. Langkilde and B. Vestergaard. Methods for structural characterization of prefibrillar intermediates and amyloid fibrils. *FEBS letters*, 583(16):2600–2609, 2009.

[54] P. Lazarev, M. Paukshto, N. Pelc, and A. Sakharova. Human tissue x-ray diffraction: breast, brain, and prostate. In *Engineering in Medicine and Biology Society, 2000. Proceedings of the 22nd Annual International Conference of the IEEE*, volume 4, pages 3230–3233. IEEE, 2000.

[55] D. Le Bihan. Looking into the functional architecture of the brain with diffusion MRI. *Nature Reviews Neuroscience*, 4(6):469–480, 2003.

[56] E. S. Lein, M. J. Hawrylycz, N. Ao, M. Ayres, A. Bensinger, A. Bernard, A. F. Boe, M. S. Boguski, K. S. Brockway, E. J. Byrnes, et al. Genome-wide atlas of gene expression in the adult mouse brain. *Nature*, 445(7124):168–176, 2007.

[57] N. Mattsson, H. Zetterberg, O. Hansson, N. Andreasen, L. Parnetti, M. Jonsson, S.-K. Herukka, W. M. van der Flier, M. A. Blankenstein, M. Ewers, et al. CSF biomarkers and incipient Alzheimer disease in patients with mild cognitive impairment. *Journal of American Medical Association*, 302(4):385–393, 2009.

[58] C. McCollough, T. Branham, V. Herlihy, M. Bhargavan, L. Robbins, K. Bush, M. McNitt-Gray, J. T. Payne, T. Ruckdeschel, D. Pfeiffer, et al. Diagnostic reference levels from the ACR CT accreditation program. *Journal of the American College of Radiology*, 8(11):795–803, 2011.

[59] I. McKeith, D. Dickson, J. Lowe, M. Emre, J. O'brien, H. Feldman, J. Cummings, J. Duda, C. Lippa, E. Perry, et al. Diagnosis and management of dementia with lewy bodies third report of the DLB consortium. *Neurology*, 65(12):1863–1872, 2005.

[60] I. McKeith, J. O'Brien, Z. Walker, K. Tatsch, J. Booij, J. Darcourt, A. Padovani, R. Giubbini, U. Bonuccelli, D. Volterrani, et al. Sensitivity and specificity of dopamine transporter imaging with 123 I-FP-CIT SPECT in dementia with lewy bodies: a phase III, multicentre study. *The Lancet Neurology*, 6(4):305–313, 2007.

[61] G. McKhann, D. Drachman, M. Folstein, R. Katzman, D. Price, and E. M. Stadlan. Clinical diagnosis of Alzheimer's disease report of the NINCDS-ADRDA Work Group* under the auspices of Department of Health and Human Services Task Force on Alzheimer's disease. *Neurology*, 34(7):939–939, 1984.

[62] D. Orthaber, A. Bergmann, and O. Glatter. SAXS experiments on absolute scale with kratky systems using water as a secondary standard. *Journal of Applied Crystallography*, 33(2):218–225, 2000.

[63] O. Paris. From diffraction to imaging: New avenues in studying hierarchical biological tissues with x-ray microbeams (review). *Biointerphases*, 3(2):FB16–FB26, 2008.

[64] S. Park, A. Badal, S. Young, and K. J. Myers. A mathematical framework for including various sources of variability in a task-based assessment of digital breast tomosynthesis. In *SPIE Medical Imaging*, pages 83134S–83134S. International Society for Optics and Photonics, 2012.

[65] B. R. Pauw. Everything SAXS: small-angle scattering pattern collection and correction. *Journal of Physics: Condensed Matter*, 25(38):383201, 2013.

[66] J. S. Pedersen. Analysis of small-angle scattering data from colloids and polymer solutions: modeling and least-squares fitting. *Advances in Colloid and Interface Science*, 70:171–210, 1997.

[67] B. Pinzer, M. Cacquevel, P. Modregger, S. McDonald, J. Bensadoun, T. Thuering, P. Aebischer, and M. Stampanoni. Imaging brain amyloid deposition using

grating-based differential phase contrast tomography. *NeuroImage*, 61(4):1336–1346, 2012.

[68] O. Querbes, F. Aubry, J. Pariente, J.-A. Lotterie, J.-F. Démonet, V. Duret, M. Puel, I. Berry, J.-C. Fort, P. Celsis, et al. Early diagnosis of Alzheimer's disease using cortical thickness: impact of cognitive reserve. *Brain*, 132(8):2036–2047, 2009.

[69] H. B. Rajamohamedsait and E. M. Sigurdsson. Histological staining of amyloid and pre-amyloid peptides and proteins in mouse tissue. *Amyloid Proteins: Methods and Protocols*, pages 411–424, 2012.

[70] P. Regnard, G. Le Duc, E. Bräuer-Krisch, I. Tropres, E. A. Siegbahn, A. Kusak, C. Clair, H. Bernard, D. Dallery, J. A. Laissue, et al. Irradiation of intracerebral 9l gliosarcoma by a single array of microplanar x-ray beams from a synchrotron: balance between curing and sparing. *Physics in Medicine and Biology*, 53(4):861, 2008.

[71] E. M. Reiman, Y. T. Quiroz, A. S. Fleisher, K. Chen, C. Velez-Pardo, M. Jimenez-Del-Rio, A. M. Fagan, A. R. Shah, S. Alvarez, A. Arbelaez, et al. Brain imaging and fluid biomarker analysis in young adults at genetic risk for autosomal dominant Alzheimer's disease in the presenilin 1 E280A kindred: a case-control study. *The Lancet Neurology*, 11(12):1048–1056, 2012.

[72] W. C. Rontgen. On a new kind of ray, a preliminary communication. *Wurzburg Physico-Médical Society on December*, 28, 1895.

[73] F. Salvat, J. M. Fernández-Varea, and J. Sempau. PENELOPE-2006: A code system for Monte Carlo simulation of electron and photon transport. In *Nuclear Energy Agency Workshop Proceedings, Barcelona, Spain*, 2006.

[74] D. Schneidman-Duhovny, M. Hammel, J. A. Tainer, and A. Sali. Accurate saxs profile computation and its assessment by contrast variation experiments. *Biophysical Journal*, 105(4):962–974, 2013.

[75] C. Schroer, M. Kuhlmann, S. Roth, R. Gehrke, N. Stribeck, A. Almendarez-Camarillo, and B. Lengeler. Mapping the local nanostructure inside a specimen by tomographic small-angle x-ray scattering. *Applied Physics Letters*, 88(16):164102, 2006.

[76] D. J. Selkoe and J. Hardy. The amyloid hypothesis of Alzheimer's disease at 25 years. *EMBO molecular medicine*, 8(6):595–608, 2016.

[77] L. C. Serpell. Alzheimers amyloid fibrils: structure and assembly. *Biochimica et Biophysica Acta (BBA)-Molecular Basis of Disease*, 1502(1):16–30, 2000.

[78] A. Serrano-Pozo, M. L. Mielke, A. Muzitansky, T. Gómez-Isla, J. H. Growdon, B. J. Bacskai, R. A. Betensky, M. P. Frosch, and B. T. Hyman. Stable size

distribution of amyloid plaques over the course of Alzheimer disease. *Journal of Neuropathology & Experimental Neurology*, 71(8):694–701, 2012.

[79] M. B. Shulman, K. Harkins, R. C. Green, and J. Karlawish. Using AD biomarker research results for clinical care a survey of ADNI investigators. *Neurology*, 81(13):1114–1121, 2013.

[80] D. H. Silverman, S. S. Gambhir, H.-W. C. Huang, J. Schwimmer, S. Kim, G. W. Small, J. Chodosh, J. Czernin, and M. E. Phelps. Evaluating early dementia with and without assessment of regional cerebral metabolism by PET: a comparison of predicted costs and benefits. *Journal of Nuclear Medicine*, 43(2):253–266, 2002.

[81] K. Siu, S. Butler, T. Beveridge, J. Gillam, C. Hall, A. Kaye, R. Lewis, K. Mannan, G. McLoughlin, S. Pearson, et al. Identifying markers of pathology in SAXS data of malignant tissues of the brain. *Nuclear Instruments and Methods in Physics Research Section A: Accelerators, Spectrometers, Detectors and Associated Equipment*, 548(1):140–146, 2005.

[82] S. W. Snyder, U. S. Ladror, W. S. Wade, G. T. Wang, L. W. Barrett, E. D. Matayoshi, H. J. Huffaker, G. A. Krafft, and T. F. Holzman. Amyloid-beta aggregation: selective inhibition of aggregation in mixtures of amyloid with different chain lengths. *Biophysical Journal*, 67(3):1216, 1994.

[83] S.-K. Song, S.-W. Sun, M. J. Ramsbottom, C. Chang, J. Russell, and A. H. Cross. Dysmyelination revealed through mri as increased radial (but unchanged axial) diffusion of water. *NeuroImage*, 17(3):1429–1436, 2002.

[84] R. A. Sperling, P. S. Aisen, L. A. Beckett, D. A. Bennett, S. Craft, A. M. Fagan, T. Iwatsubo, C. R. Jack, J. Kaye, T. J. Montine, et al. Toward defining the preclinical stages of Alzheimers disease: Recommendations from the National Institute on Aging-Alzheimer's Association workgroups on diagnostic guidelines for Alzheimer's disease. *Alzheimer's & Dementia*, 7(3):280–292, 2011.

[85] R. Stapulionis, C. L. P. Oliveira, M. C. Gjelstrup, J. S. Pedersen, M. E. Hokland, S. V. Hoffmann, K. Poulsen, C. Jacobsen, and T. Vorup-Jensen. Structural insight into the function of myelin basic protein as a ligand for integrin $\alpha$m$\beta$2. *The Journal of Immunology*, 180(6):3946–3956, 2008.

[86] D. Stout, P. Chow, R. Silverman, R. M. Leahy, X. Lewis, S. Gambhir, and A. Chatziioannou. Creating a whole body digital mouse atlas with PET, CT and cryosection images. *Mol. Imaging Biol*, 4(4):S27, 2002.

[87] A. Tartari, A. Taibi, C. Bonifazzi, and C. Baraldi. Updating of form factor tabulations for coherent scattering of photons in tissues. *Physics in Medicine and Biology*, 47(1):163, 2001.

[88] E. Valentini, A. G. Kikhney, G. Previtali, C. M. Jeffries, and D. I. Svergun. SASBDB, a repository for biological small-angle scattering data. *Nucleic Acids Research*, page gku1047, 2014.

[89] V. L. Villemagne, S. Burnham, P. Bourgeat, B. Brown, K. A. Ellis, O. Salvado, C. Szoeke, S. L. Macaulay, R. Martins, P. Maruff, et al. Amyloid $\beta$ deposition, neurodegeneration, and cognitive decline in sporadic Alzheimer's disease: a prospective cohort study. *The Lancet Neurology*, 12(4):357–367, 2013.

[90] G. Waldemar, B. Dubois, M. Emre, J. Georges, I. McKeith, M. Rossor, P. Scheltens, P. Tariska, and B. Winblad. Recommendations for the diagnosis and management of Alzheimer's disease and other disorders associated with dementia: EFNS guideline. *European Journal of Neurology*, 14(1):e1–e26, 2007.

[91] S. J. Wilkinson, K. D. Rogers, C. J. Hall, and A. R. Round. Small angle scatter imaging from wide beam diffraction patterns. *Physics in Medicine and Biology*, 52(9):2409, 2007.

[92] Y. Yin, B. Bassit, L. Zhu, X. Yang, C. Wang, and Y. Li. $\gamma$-secretase substrate concentration modulates the A$\beta_{42}$/A$\beta_{40}$ ratio: Implications for Alzheimer's disease. *The Journal of Biological Chemistry*, 282(32):2363944, 2007.

[93] S. Young, A. Badal, K. J. Myers, and S. Park. A task-specific argument for variable-exposure breast tomosynthesis. In *Breast Imaging*, pages 72–79. Springer, 2012.

[94] F. Zhang, J. Ilavsky, G. G. Long, J. P. Quintana, A. J. Allen, and P. R. Jemian. Glassy carbon as an absolute intensity calibration standard for small-angle scattering. *Metallurgical and Materials Transactions A*, 41(5):1151–1158, 2010.